

Bachelor's Thesis

Sensitivitätsanalyse für die Beobachtung von Spin-Korrelationen im $t\bar{t} \rightarrow$ Lepton+Jets Kanal

Sensitivity Study for the Observation of Spin Correlations in the $t\bar{t} \rightarrow$ lepton+jets channel

prepared by

Theresa Reisch

from Northeim

at the II. Physikalischen Institut

Thesis number: II.Physik-UniGö-BSc-2022/04

Thesis period: 28th March 2022 until 4th July 2022

First referee: Prof. Dr. Arnulf Quadt

Second referee: Prof. Dr. Ariane Frey

Abstract

In this work, spin correlations between the top and the anti-top quark are investigated in a sensitivity analysis. For this purpose, the decay channel of $t\bar{t} \rightarrow \text{lepton} + \text{jets}$ is considered and the strange quark is identified as a spin analyser next to the charged lepton using a c -tagging approach. Based on this, spin observables are constructed and analytical formulas are fitted to the distributions to obtain the spin coefficients. The reconstructed distributions are unfolded to the parton level and the sensitivity achieved is investigated considering systematic uncertainties.

The best sensitivity was achieved for the $C(n, n)$ coefficient with a 31σ intervals distance to the no spin correlations value. The other coefficients have σ intervals of 3, 15 and 20σ . In conclusion, a good sensitivity to spin correlations was reached.

Keywords: top quark, $t\bar{t}$ pair production, spin correlation, c -tagging

Zusammenfassung

In dieser Arbeit werden Spin-Korrelationen zwischen dem Top- und dem Anti-Top-Quark in einer Sensitivitätsanalyse untersucht. Dazu wird der Zerfallskanal von $t\bar{t} \rightarrow \text{Lepton} + \text{Jets}$ betrachtet und das Strange-Quark als Spin-Analysator neben dem geladenen Lepton mit Hilfe von einem c -tagging Ansatz identifiziert. Darauf aufbauend werden Spin-Observablen konstruiert und analytische Formeln an die Verteilungen gefittet, um die Spin-Koeffizienten zu erhalten. Die rekonstruierten Verteilungen werden auf das Parton-Level entfaltet und die erreichte Sensitivität unter Berücksichtigung von systematischen Unsicherheiten untersucht.

Die beste Sensitivität wurde für den $C(n, n)$ Koeffizienten mit einem 31σ Abstand zu dem Wert ohne Spin-Korrelationen erreicht. Die anderen Koeffizienten haben σ -Intervalle von 3, 15 und 20σ . Daraus lässt sich schließen, dass eine gute Sensitivität für die Spin-Korrelationen erzielt wurde.

Stichwörter: Top-Quark, $t\bar{t}$ -Paarproduktion, Spin-Korrelation, c -tagging

Contents

1. Introduction	1
2. Theory	3
2.1. The Standard Model of Particle Physics	3
2.1.1. Overview	3
2.1.2. The Strong Interaction	4
2.1.3. The Electromagnetic Interaction	5
2.1.4. The Weak Interaction	5
2.2. Top Quark	6
2.2.1. Top Quark Properties	6
2.2.2. Top Quark Pair Production	6
2.2.3. Top Quark Decay	7
2.2.4. Spin Correlation	9
2.2.5. Observables	10
3. Experimental Setup	13
3.1. The LHC	13
3.2. The ATLAS Detector	13
3.2.1. Overview	13
3.2.2. Detector Components	15
4. Experimental Techniques	17
4.1. b -Tagging	17
4.2. Event Reconstruction with KLFitter	18
4.3. Profile Likelihood Unfolding with TRexFitter	19
5. Sensitivity Study for the Observation of Spin Correlations	21
5.1. Investigation of possible c -tagging WPs	21
5.1.1. Preparation	21
5.1.2. Signal Regions	23

5.2. Investigation of Spin Observables	25
5.2.1. Construction of the Observables	25
5.2.2. Reconstruction	25
5.2.3. Spin Sensitivity	29
5.2.4. Fitting	31
5.2.5. Check with no Spin Correlations Sample	34
5.2.6. Background	35
5.3. Unfolding	37
5.3.1. Closure Test	37
5.3.2. Results	39
5.3.3. Systematic Uncertainties	42
6. Conclusion	47
A. Additional Plots for the Investigation of Spin Observables	49
A.1. Migration Matrix	49
A.2. Comparison Truth and Reconstructed Distribution	54
A.3. Selection Efficiencies	59
A.4. Acceptance	62
A.5. Comparison Pre- and Post-Fit Plots	65
B. Additional Plots for the Systematics	73
B.1. $\cos \theta_l^k \cos \theta_s^k$	74
B.1.1. $t\bar{t}$ Matrix Element	74
B.1.2. $t\bar{t}$ Parton Shower	75
B.1.3. Final State Radiation	76
B.2. $\cos \theta_l^n \cos \theta_s^n$	77
B.2.1. $t\bar{t}$ Matrix Element	77
B.2.2. $t\bar{t}$ Parton Shower	78
B.2.3. Final State Radiation	79
B.3. $\cos \theta_l^r \cos \theta_s^r$	80
B.3.1. $t\bar{t}$ Matrix Element	80
B.3.2. $t\bar{t}$ Parton Shower	81
B.3.3. Final State Radiation	82
B.4. $\cos \varphi$	83
B.4.1. $t\bar{t}$ Matrix Element	83
B.4.2. $t\bar{t}$ Parton Shower	84

B.4.3. Final State Radiation 85

Nomenclature

Variables

variable	meaning	unit
S	spin	\hbar
Q	electric charge	e
I_3	weak isospin	-
m	mass	GeV
E	energy	GeV
\sqrt{s}	centre of mass energy	GeV
τ	lifetime	s
τ_{had}	hadronisation time	s
τ_{deco}	spin decorrelation time	s
x	Bjorken x	-
V_{xy}	CKM matrix element	-
α_i	spin analysing power	-
C/D	spin coefficients	-
\mathcal{C}	spin desity matrix	-
η	pseudorapidity	-
\mathcal{L}	likelihood	-
LL	logarithmic likelihood	-
P	event probability	-
p_T	tranverse momentum	GeV
ϵ	efficiency	-
a	acceptance	-

Particles

symbol	particle	pdgId
u	up quark	1
d	down quark	2
s	strange quark	3
c	charm quark	4
b	bottom quark	5
t	top quark	6
\bar{q}	anti quark	- pdgId(q)
l	charged lepton	11, 13, (15)
ν	neutrino	12, 14, (16)
g	gluon	21
Z	Z boson	23
$W^{+/-}$	W boson	± 24

Abbreviations

abbreviation	meaning
SM	Standard Model
QCD	Quantum Chromodynamics
QED	Quantum Electrodynamics
QFD	Quantum Flavourdynamics
EWT	Electroweak Theory
PDF	Parton Density Function
CME	Centre of Mass Energy
CKM	Cabibbo-Kobayashi-Maskawa
CERN	Conseil Européen pour la Recherche Nucléaire
LHC	Large Hadron Collider
LEP	Large Electron Positron Collider
ATLAS	A Toroidal LHC Apparatus
EM	Electromagnetic
KLFitter	Kinematic Likelihood Fitter
WP	Working Point
PLU	Profile Likelihood Unfolding

abbreviation	meaning
POI	Point of Interest
PCBT	Pseudo Continuous b -Tagging
PdgId	Particle Data Group Id
SR	Signal Region
ndf	Number of Degrees of Freedom
MC	Monte Carlo
NP	Nuisance Parameter
ISR	Initial State Radiation
FSR	Final State Radiation

1. Introduction

When looking at the history of mankind, the question "What keeps the world together in its inner core?" has always been important and philosophy and religion attempted to provide an answer. From a current, scientific point of view, the Standard Model of Particle Physics offers a suitable approach to explain the fundamental mechanism of the universe. In general, particle physics describes the nature of the elementary particles and their interaction via forces. As a consequence, particle physics is one of the most fundamental branches of physics and attempts to find a theory describing high energy phenomena as they happened shortly after the universe formed.

These phenomena are studied at particle colliders such as the LHC at CERN, where protons are brought to collision at high energies to create new particles. The most famous success of the LHC was the discovery of the Higgs boson in 2012 at ATLAS [1] and CMS [2], which has been predicted since the 1960s and is essential for the Higgs mechanism explaining the mass of most of the particles. But still, there are problems unexplained by the Standard Model like the origin of the neutrino mass that is necessary for the neutrino oscillation already observed [3]. Therefore, probing the Standard Model and its prediction is an important way to discover new physics.

The top quark as a part of the Standard Model is the most massive of the elementary particles with the shortest lifetime. According to the Standard Model, it is a spin $S = \frac{1}{2}$ fermion. By investigating the spin correlations between top and anti-top, also the spin of the top quark is examined and therefore the Standard Model predictions are tested. In the top quark pair production via the strong interaction, the top quarks are unpolarised and the spin properties are directly transmitted to the decay products. The channel used for this analysis is the lepton+jets decay channel of $t\bar{t}$ where the strange quark and the charged lepton are taken as spin analysers. To identify the strange quark, a c -tagging approach and event reconstruction is used. The observables sensitive to spin correlations are analysed and relevant spin coefficients are obtained by fitting the distributions and performing unfolding.

1. Introduction

Beginning with a theoretical overview of the Standard Model of Particle Physics including sections about the top quark and spin correlations in Ch. 2, the basis of the experimental setup consisting of the LHC and the ATLAS experiment is then described in Ch. 3. Ch. 4 covers the experimental techniques used in this analysis such as b -tagging, event reconstruction and unfolding. The results of the analysis are shown in Ch. 5 and Ch. 6 provides a summary and an outlook for further research.

2. Theory

This chapter provides the theoretical background for the analysis in this thesis consisting of the Standard Model, details about the top quark and spin correlations.

2.1. The Standard Model of Particle Physics

2.1.1. Overview

The Standard Model of Particle Physics (SM) presents the current understanding of three of the four fundamental forces and the elementary particles.

As seen in Fig. 2.1, the SM consists of fermions with spin $S = \frac{1}{2}$, gauge bosons with spin $S = 1$ and the Higgs boson with spin 0. In general, the fermions can be divided into quarks and leptons which can be distinguished by their interaction properties. There are six quarks and six leptons that can be classified in three generations (shown with three columns in Fig. 2.1). Two left-handed fermions in a generation form a weak isospin doublet. The quark doublets consist of an up type quark with electric charge $Q = +\frac{2}{3}$ and third component of the weak isospin $I_3 = +\frac{1}{2}$ and a down type quark with electric charge $Q = -\frac{1}{3}$ and third component of the weak isospin $I_3 = -\frac{1}{2}$. The lepton doublets contain an electrically neutral, massless neutrino and a charged lepton with electric charge $Q = -1$.

The gauge bosons are vector bosons and force carriers for three fundamental forces: strong force, weak force and electromagnetic force; gravitation as a fourth force is not included. The Higgs boson is a scalar boson that gives the massive particles their mass.

Out of all these particles, the electron and up and down quark are the stable particles forming the matter existing in the universe. According to the SM, neutrinos are also stable but neutrino oscillation has already been observed which can only be explained if neutrinos are massive. The other particles are unstable and decay into the stable ones via one of the three forces.

distance r , the larger the potential and from the energy new quarks are created forming new hadrons and a jet.

At low-energy scales, α_S is close to 1, therefore large compared to the other coupling constants. But since α_S decreases with increasing energy and is not constant (so-called running coupling), it has an asymptotic freedom [8].

2.1.3. The Electromagnetic Interaction

Quantum electrodynamics (QED) describes the electromagnetic interaction with the massless photon as the exchange particle. The electromagnetic force couples to electric charge, therefore all quarks, the charged leptons and the W bosons are affected, but not the photon itself.

2.1.4. The Weak Interaction

Lastly, the weak interaction is mediated via the exchange of either W bosons or Z bosons. The theory describing the weak interaction is called quantum flavour dynamics (QFD). Because of its coupling to the weak isospin, all quarks and leptons are affected as well as the force carriers of the weak interaction. In QFD, left-handed particles and right-handed particles are sorted into weak isospin doublets while right-handed particles and left-handed anti-particles form singlets. The charged currents mediated by the W bosons only affect left-handed particles and right-handed anti-particles and are able to change the flavour of the particle with a strength described by the CKM matrix [9]. The vertex factor for this interaction can be described by

$$i \frac{g_w}{2\sqrt{2}} \gamma_\mu \frac{1 - \gamma_5}{2} V_{ij}$$

with the coupling strength g_w and V_{ij} being the element of the CKM matrix (only if quarks are involved). The term $1 - \gamma_5$ is the left-handed chirality operator which projects the left-handed part of a state. In contrast, the neutral currents mediated by the Z boson affect both left- and right-handed particles are shown by the vertex factor

$$i \frac{g_z}{2} \gamma_\mu (g_v - g_a \gamma_5),$$

where the vector-axial vector coupling $(g_v - g_a)\gamma_5$ indicates the preference to a coupling to left-handed particles. In contrast to the other gauge bosons, the W and Z bosons are massive because of their interaction with the Higgs field [10, 11].

2. Theory

At high energies of about 246 GeV, the electromagnetic and the weak force can be unified to one single electroweak force described by the electroweak theory (EWT) [12–14].

2.2. Top Quark

The top quark was discovered at FERMILAB by the DØ [15] and CDF collaborations [16] in 1995 after being predicted in 1973 [9]. It was the last quark to be discovered because of its huge mass.

2.2.1. Top Quark Properties

The top quark is a spin $\frac{1}{2}$ fermion with a charge of $Q = +\frac{2}{3}$ and the weak isospin partner of the bottom quark with the top's isospin $I_3 = +\frac{1}{2}$. It is therefore a particle of the third generation.

Of all the six quarks, the top quark is the most massive one with the shortest lifetime. Due to its huge mass, the top quark has the strongest Yukawa coupling to the Higgs field (in the order of 1), which makes it interesting to study. The top mass is found to be

$$m_t = (172.69 \pm 0.30) \text{ GeV} \quad (2.2)$$

via direct measurements [17]. The lifetime is $\tau \approx 5 \cdot 10^{-25}$ s [17], while the time for quarks to hadronise and build bound states is $\tau_{\text{had}} \approx 10^{-24}$ s [18]. Therefore, the top quark is the only quark that decays before it hadronises. In addition, the top quark lifetime is much shorter than the spin decorrelation time of $\tau_{\text{deco}} \approx 10^{-21}$ s [19], which is why the top quark is suitable for examining spin correlations.

2.2.2. Top Quark Pair Production

Top quarks can either be produced as a pair of top and anti-top or as a single top quark, but to study spin correlations, the focus will be on the pair production. At the TEVATRON, a proton anti-proton collider, the dominating production process is the $q\bar{q}$ annihilation; the corresponding Feynman diagram is shown in the upper row of Fig. 2.2. In contrast, at the LHC, a proton-proton collider, top quarks are mostly produced via gluon-gluon fusion, which can be explained by looking at the parton density functions (PDFs).

Each parton of a hadron carries only a fraction of the total momentum described by the Bjorken x . Because the collision is inelastic and only the partons interact, the necessary

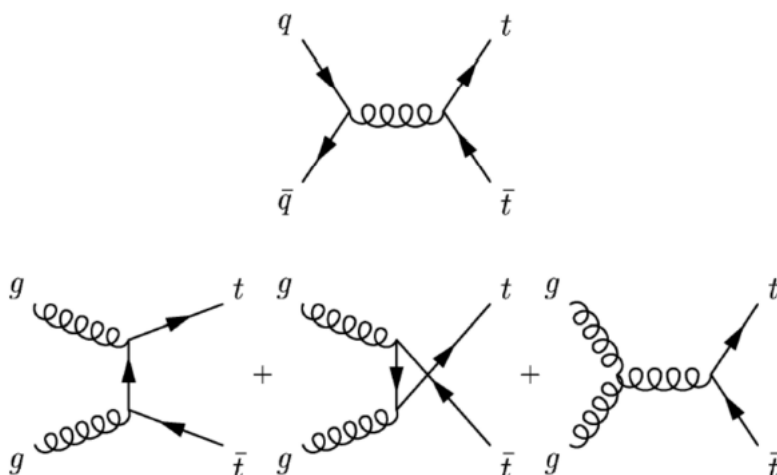


Figure 2.2.: The Feynman diagrams for the top quark pair production.

effective centre of mass energy (CME) for the production of a top anti-top pair is given by

$$\sqrt{s_{\text{eff}}} = \sqrt{x_1 x_2 s} \geq 2m_t. \quad (2.3)$$

In conclusion, at a high CME a low x is sufficient for producing top anti-top pairs. In particular, the PDF for gluons has extraordinarily high values for low x and a high CME, which is the setting at LHC, and therefore gluon-gluon fusion is the dominating production process there.

The leading order Feynman diagrams for the gluon-gluon fusion can be seen in the lower row of Fig. 2.2. Both the gluon-gluon fusion and quark-anti-quark annihilation are interactions of the strong force, which is parity conserving, therefore the top quark is unpolarised in leading order processes.

2.2.3. Top Quark Decay

As already mentioned, the top quark decays after a very short period of time. Because the element of the CKM matrix $|V_{tb}|^2$ is nearly 1 [17] and the decay rate is proportional to this element, the top quark decays into a bottom quark and a W boson in 99.8% of all cases. The W boson, in contrast, has different decay modes. In $(67.41 \pm 0.27)\%$ of all cases, the W boson decays into quarks [17], where the decay rate is again proportional to the CKM matrix element and in the rest of the cases, it decays leptonically to a charged lepton and a lepton neutrino, where the decay rate is equal for the different lepton flavours (lepton universality).

2. Theory

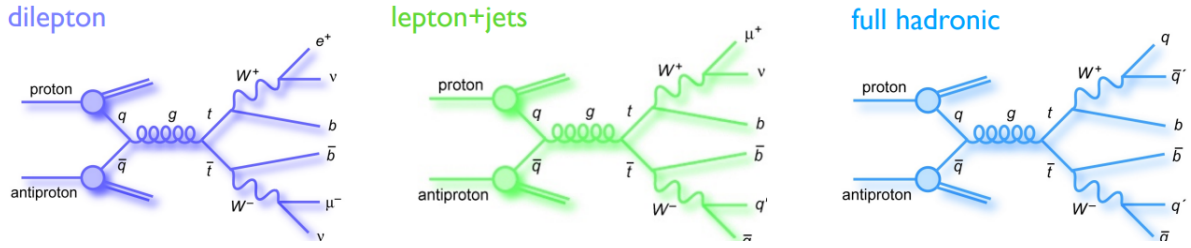


Figure 2.3.: Three different kinds of decays for a top quark pair produced via quark anti-quark fusion.

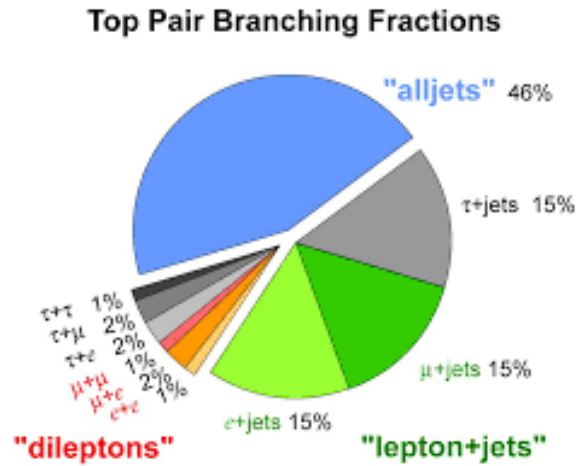


Figure 2.4.: Branching ratios for the $t\bar{t}$ decay.

In Fig 2.3, the different decay modes of the top quark pair are presented because each of the two W bosons can decay either hadronically or leptonically. As shown in Fig. 2.4, the dileptonic channel has a branching ratio of around 0.105, which is low compared to a branching ratio of 0.438 for the mixed channel and 0.457 for the fully hadronic channel [17]. These values can easily be deduced from the W decay modes mentioned earlier. The signal from the dileptonic decay can be separated from the background very easily since the signature of leptons can clearly be determined. In general, the background impact increases with the number of hadronic decays in the considered decay channel.

In this thesis, the mixed channel where one W boson decays leptonically and the other one hadronically is used to study spin correlations because it provides the best compromise between good signal to background ratio and a high branching ratio. Usually, events where a W boson decays into a τ lepton are excluded because the τ lepton itself decays either leptonically or hadronically. Consequently, it is not possible to detect the τ but it rather needs to be reconstructed and the decay products can get mixed up with the other

	b	W	l	d/s	u/c
$\alpha_i(\text{LO})$	-0.41	0.41	1	1	-0.31
$\alpha_i(\text{NLO})$	-0.39	0.39	0.998	0.97	-0.32

Table 2.1.: Spin analysing powers of different particles [21].

decay products.

2.2.4. Spin Correlation

The top quark decaying faster than the spin decorrelation time makes it suitable for studying spin correlations since the spin properties are directly passed to the decay products. The angular distribution of the top quark decay products contains information about the spin of the particles and can therefore be used to analyse spin correlations. The cross section σ can be described by [20]

$$\frac{1}{\sigma} \frac{d\sigma}{d \cos(\theta_i)} = (1 + \alpha_i |\mathbf{P}|^3 \cos(\theta_i))/2 \quad (2.4)$$

with the spin analysing power α_i , the top polarisation vector \mathbf{P} and θ_i being the angle between the momentum direction of decay product i of the top quark and \mathbf{P} .

The spin analysing power α_i describes the degree to which the top quark spin is transferred to the decay product i and can take values between -1 and 1 . Because it is close to 1 for charged leptons and the down or strange quark, these are the ones used for the analysis. To find the strange quark, the associated charm quark is tagged using the DL1r b -tagger [22] because the charm quark has properties similar to the bottom quark regarding parameters relevant for b -tagging (more in Ch. 4). The strange quark cannot be tagged like this but with full reconstruction of the W boson, the strange quark can be found. The bottom quark as another down type quark has a weaker spin analysing power but since the decay of a W boson into a b quark is suppressed because of the CKM matrix element, it is sufficient to look at the down type quark of the hadronically decaying W boson. The spin analysing power for up type quarks like the up or charm quark is around $\alpha_i = -0.3$, as listed in Tab. 2.1, what weakens the effect measurably.

2. Theory

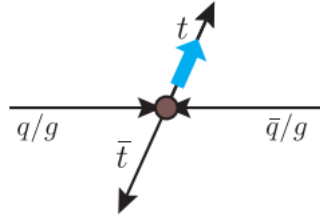


Figure 2.5.: Helicity basis.

2.2.5. Observables

Different observables are chosen for studying top quark spin correlations. One of them is the angle $\Delta\phi$ between the momentum directions of the charged lepton from the leptonically decaying W boson and the down type quark from the hadronically decaying W boson in the laboratory frame and in the helicity basis. The helicity basis is defined as the basis in which the top spin is aligned with the top quark's direction of flight in the $t\bar{t}$ rest frame, which can be seen in Fig. 2.5. The observable in the helicity basis is specified with the index $\Delta\phi_{hb}$. The $\Delta\phi$ observable is sensitive to the spin correlation but the spin sensitivity depends on $m_{t\bar{t}}$ and with higher values the sensitivity is expected to vanish [23].

The other four observables have an analytical formula which can be used to extract spin information via fitting of the unfolded distributions. Three of them can be expressed as $\cos(\theta_l^a) \cos(\theta_s^a)$ where only the axis $a = \{k, r, n\}$ for taking θ vary (see Tab. 2.2). In the following, the superscript is dropped if the generalisation of the three observables is meant and specified otherwise.

If the W^+ from the top quark decays leptonically, the θ are calculated according to

$$\cos \theta_l = \hat{l} \cdot \hat{a} \quad \text{and} \quad \cos \theta_s = \hat{s} \cdot \hat{b},$$

with \hat{l}, \hat{s} being the unit vectors of the particle's directions of flight, \hat{a} the t reference axis and \hat{b} the \bar{t} reference axis. For a leptonic decay of the W^- from the anti top, \hat{a} and \hat{b} switch. There are three different choices for \hat{a} and \hat{b} described in Tab. 2.2, with the

name	\hat{a}	\hat{b}
transverse n	$\text{sign}(y_p)\hat{n}_p$	$-\text{sign}(y_p)\hat{n}_p$
radial r	$\text{sign}(y_p)\hat{r}_p$	$-\text{sign}(y_p)\hat{r}_p$
helicity k	\hat{k}	$-\hat{k}$

Table 2.2.: Choice of reference axes. The variables are defined in detail in Eq. (2.5)-(2.8).

variables defined as [24]

$$\hat{k} = t \text{ direction of flight in } t\bar{t} \text{ rest frame,} \quad (2.5)$$

$$\hat{p}_p = \text{proton direction of flight in lab frame,} \quad (2.6)$$

$$y_p = \hat{p}_p \cdot \hat{k}, \quad r_p = \sqrt{1 - y_p^2}, \quad (2.7)$$

$$\hat{r}_p = \frac{1}{r_p}(\hat{p}_p - y_p \hat{k}), \quad \hat{n}_p = \frac{1}{r_p}(\hat{p}_p \times \hat{k}). \quad (2.8)$$

To extract the spin correlation coefficients, the relation [24]

$$\frac{1}{\sigma} \frac{d\sigma}{d \cos \theta_l \cos \theta_s} = \frac{1}{2}(1 - C \cdot \cos \theta_l \cos \theta_s) \ln \left(\frac{1}{|\cos \theta_l \cos \theta_s|} \right) \quad (2.9)$$

is used to fit the normalised distributions. According to Eq. (2.9), the parameter C is linked to the mean of the distribution via

$$C = -9 \cdot \langle \cos \theta_l \cos \theta_s \rangle.$$

The relevance of the $\cos \theta_l \cos \theta_s$ observable comes from the connection of the C parameter to the spin correlation via [24]

$$C(\hat{a}, \hat{b}) = \alpha_l \alpha_s \frac{\sigma(\uparrow\uparrow) + \sigma(\downarrow\downarrow) - \sigma(\uparrow\downarrow) - \sigma(\downarrow\uparrow)}{\sigma(\uparrow\uparrow) + \sigma(\downarrow\downarrow) - \sigma(\uparrow\downarrow) + \sigma(\downarrow\uparrow)}, \quad (2.10)$$

with the spin analysing powers α_i and the spin asymmetry $A = \frac{\sigma(\uparrow\uparrow) + \sigma(\downarrow\downarrow) - \sigma(\uparrow\downarrow) - \sigma(\downarrow\uparrow)}{\sigma(\uparrow\uparrow) + \sigma(\downarrow\downarrow) - \sigma(\uparrow\downarrow) + \sigma(\downarrow\uparrow)}$, where σ represents the spin operator applied on the $t\bar{t}$ system. Therefore, by extracting the parameter C from the distribution spin correlations can be measured.

The opening angle between the two spin analysers

$$\cos \varphi = \hat{l} \cdot \hat{s}$$

2. Theory

can also be used to determine spin correlations since the normalised distribution can be described by [24]

$$\frac{1}{\sigma} \frac{d\sigma}{d \cos \varphi} = \frac{1}{2}(1 - D \cdot \cos \varphi), \quad D = -3 \cdot \langle \cos \varphi \rangle. \quad (2.11)$$

The factor D is proportional to the trace of the spin density matrix \mathcal{C} consisting of the C parameters from before via

$$D = -\frac{1}{3} \text{Tr}(\mathcal{C}) = -\frac{1}{3} (C(n, n) + C(r, r) + C(k, k)).$$

Besides the sensitivity to spin correlations, the D parameter extracted from the $\cos \varphi$ distribution can indicate quantum entanglement in $t\bar{t}$. This entanglement in quarks has not been detected yet. To check the $\cos \varphi$ observable, a cut on $m_{t\bar{t}}$ has to be applied, where only events with $m_{t\bar{t}} < 390 \text{ GeV}$ are considered. There the sensitivity to the entanglement is enhanced because of the proximity to the $t\bar{t}$ threshold ($\sim 350 \text{ GeV}$) [25]. The marker for the entanglement is a value of $D < 1/3$.

3. Experimental Setup

The data used for studying top quark spin correlations is collected at the ATLAS (**A** **T**oroidal **L**HC **A**pparatu**S**) detector at the LHC. The LHC (**L**arge **H**adron **C**ollider) is a proton proton collider at the research centre CERN (**C**onseil **E**uropéen pour la **R**echerche **N**ucléaire).

3.1. The LHC

The LHC is a synchrotron with a circumference of around 27 km located in Geneva [26]. The first collision was achieved in 2010 at a CME of 7 TeV but since then the LHC was upgraded with the latest CME of 13.6 TeV at the start of Run 3 in 2022, the highest collision energy up until now. It is designed to reach a CME of 14 TeV that is expected to be reached with the upgrade to the High Luminosity Large Hadron Collider (HL-LHC) starting 2029 [27]. The LHC can achieve such high energies since it is a hadron collider with a smaller synchrotron radiation loss at high energies compared to lepton colliders like LEP (Large Electron Positron Collider), the predecessor of LHC.

The particles are accelerated with the help of different circular accelerators until they reach velocities close to the vacuum speed of light and are brought to collision. As shown in Fig. 3.1, there are four interaction points where the accelerated particles collide and the detectors ATLAS [28], ALICE [29], CMS [30] and LHCb [31] are positioned.

3.2. The ATLAS Detector

3.2.1. Overview

ATLAS is the largest particle detector at the LHC with a length of 46 m, a diameter of 25 m and a mass of about 7,000 t. It is a cylindric general purpose detector that focuses on measuring new processes or particles and their properties, namely the masses, momenta,

3. Experimental Setup

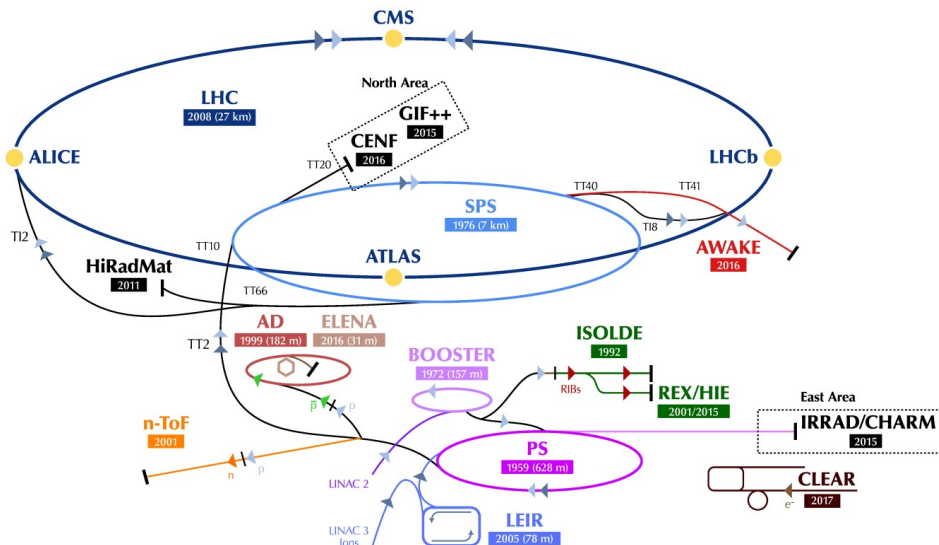


Figure 3.1.: Structure of the CERN complex and LHC (©CERN).

energies, lifetimes, electric charges and spins.

The detector consists of different layers, which can be seen in Fig. 3.2. Generally, the detector can be divided into four major components: the inner detector, the calorimeters, the muon spectrometer, and the magnet system. The inner detector tracks the particles and the calorimeters measure the energy of the particles by stopping them. As the name indicates, the muon system focuses on measuring muon properties and the magnetic system deflects the charged particles so they are measured in the inner detector and muon spectrometer. The only particles that the ATLAS detector cannot detect are neutrinos because they rarely interact with matter. Because neutrinos can be a part of the top quark decay, their energy and momentum are reconstructed via the missing transverse momentum. In hadron colliders, the total missing momentum cannot be determined since the partons of the hadron carry different momentum fractions but the momentum transverse to the beam line is zero before the collision. Therefore, if the total transverse momentum in the final states is not zero, it indicates missing transverse momentum.

The coordinates to describe the detector are the cylindrical coordinates consisting of the azimuthal angle ϕ , the polar angle θ and the z axis along the beam line. Using this and the assumption that in high energy physics the particle mass can be neglected, the pseudorapidity η can be defined as

$$\eta \equiv -\ln \left(\tan \frac{\theta}{2} \right).$$

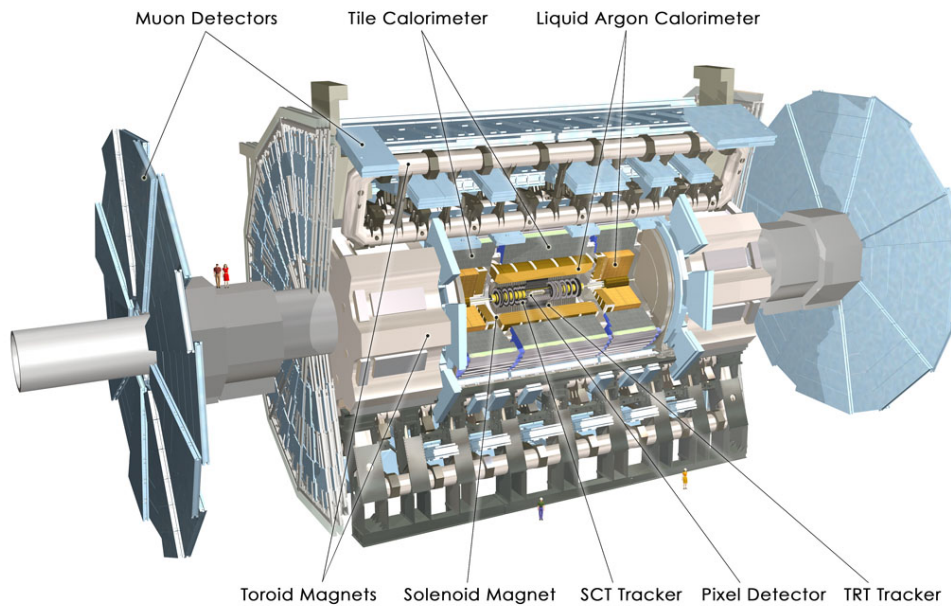


Figure 3.2.: The different layers of the ATLAS detector (©CERN).

In the following, the pseudorapidity is used to show the ranges of the detector components covered. Differences in the pseudorapidity $\Delta\eta$ are Lorentz invariant under boosts, which is an important property for hadron colliders because there the collision system is boosted due to the different momentum fractions of the partons.

3.2.2. Detector Components

The inner detector tracks charged particles and collects information about the type of particle and their momentum, especially the starting point of the track can be used for b -tagging (see Ch. 4.1). The inner detector tracks particles with a pseudorapidity $|\eta| < 2.5$ with three different components. One of the components of the inner detector is the silicon-based Pixel detector, which can measure tracks very precisely due to its short distance to the interaction point. The other two parts are the semi-conductor tracker and the transition radiation tracker covering a larger area to track particles.

The ATLAS detector has an electromagnetic and a hadronic calorimeter (both sampling calorimeters). The hadronic calorimeter is necessary since some strongly interacting, electrically neutral particles might pass through the electromagnetic calorimeter. The EM calorimeter absorbs energy from charged particles and photons and is characterised by a high precision in terms of the energy and location of the particles. The precision of the hadron calorimeter is lower but otherwise the mechanism is identical. The two calorime-

3. *Experimental Setup*

ters combined cover a pseudorapidity of $|\eta| < 4.9$.

Since muons are more massive than electrons and lose less energy to bremsstrahlung, which makes them minimal ionising particles, they must be detected in the outer part of the detector in the specialised muon spectrometers. These spectrometers cover a pseudorapidity of $|n| < 2.7$. Most of the particles will not pass the calorimeters, so the muon identification is accurate.

The magnet system of the ATLAS detector consists of two superconducting magnet systems: the solenoid, which surrounds the inner detector and allows precise measurement of the momenta of even very energetic particles, and the outer toroid magnets within the muon systems.

Another important tool for recording data is the trigger system that uses fast event reconstruction to select the most interesting events because it is not possible to store all the events. The trigger system consists of two trigger levels with the Level 1 trigger implemented in hardware and making decisions in less than $2.5 \mu\text{s}$. The events saved by the first level trigger are then sorted by the High Level trigger implemented in software and deciding in $200 \mu\text{s}$. Out of 40 MHz of events happening, about 1,000 Hz remain for the offline analysis.

4. Experimental Techniques

To study spin correlations in the lepton + jets channel, b tagging and event reconstruction are necessary. Not only the two b jets from t and \bar{t} can be identified via b -tagging, but also the c jet from the hadronically decaying W boson. To assign the jets to the W boson (and parent top/anti-top), the event reconstruction with KLFitter is used. Lastly, the reconstructed distributions are unfolded to match the parton level.

4.1. b -Tagging

As already mentioned, the top quark nearly always decays into a bottom quark, which then hadronises and forms a jet. The special property of B hadrons is their long lifetime due to the low value of the CKM matrix elements V_{cb} and V_{ub} for possible decays. The CKM matrix states that decays within generation of quarks are far more likely to occur than those between generations and since the top quark is the weak isospin partner of the b quark and much more massive than the b quark, B hadrons have unusually long lifetimes. This property can be used to identify jets originating from bottom quarks in collision data by reconstructing the secondary vertex from jet tracks. The difference between b jets and light jets is shown in Fig. 4.1. Moreover, b quarks are heavier than their decay products what causes the decay products to have a higher transverse momentum. Consequently, the jets are wider, have higher numbers of particles and higher invariant masses what can also be used for the b -tagging.

When studying spin correlations, not only identifying the b quark but also finding the charm quark is relevant because of the spin analysing power of the associated strange quark. To achieve this, the DL1r tagger is used [22] because it also has sensitivity to c jets due to similar properties as the b jets. C hadrons have a shorter lifetime than B hadrons but still a longer lifetime than hadrons containing light quarks, which is why the b -tagger might mistag them as a b jet. In Addition, the mass of the c quark is higher than for the light quarks but smaller than the b quark mass.

The working points (WPs) of DL1r differ in the ratio of b jets identified and therefore in

4. Experimental Techniques

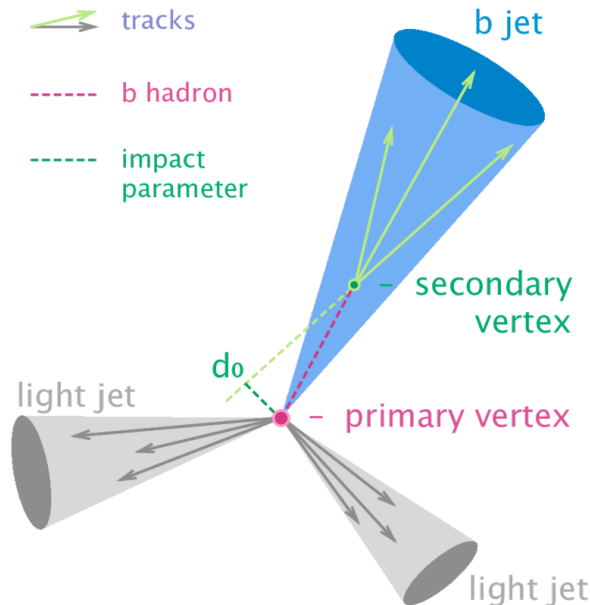


Figure 4.1.: Diagram of a b jet with a secondary vertex compared to a light jet.

WP	incl. b jet eff.	excl. b jet eff.
1	100 %	14.74 %
2	85.26 %	7.66 %
3	77.60 %	6.66 %
4	70.94 %	9.62 %
5	61.32 %	61.32 %

Table 4.1.: Definition of the DL1r WPs. The inclusive efficiency is the efficiency inclusive for all the lower WPs, whereas the exclusive efficiency describes the difference between adjoined inclusive efficiencies.

their efficiency and purity. As can be seen in Tab. 4.1, the first WP identifies all of the b jets but also mistags all of the other jets, so its purity is low and the WP is not useful. The WPs 2-4 can be considered loose WPs with a lower purity but higher efficiency. In contrast, the last WP, a tight WP, leaves out b jets but has a low mistag rate instead, so a high purity and a low efficiency. This WP properties can be used to perform the c -tagging (see Ch. 5.1).

4.2. Event Reconstruction with KLFilter

As already mentioned, the energy and transverse momentum of the final particles are measured but they still must be assigned to the correct particles. This can be achieved by using the Kinematic Likelihood Fitter [32] for the reconstruction. KLFilter is based

on maximising the likelihood function \mathcal{L} , which consists of different functions giving the likelihood of measured parameters like the mass matching with the real parameters of the particles. One component of the likelihood function are the Breit-Wigner functions B that have their maximum for the particle's expected mass and falls off according to the mass distribution. The other component, the transfer functions W , work similarly by modelling the relation of the energy or momentum of the assumed particle to the energies and momenta measured in the detector. As a result, the likelihood can be written as

$$\begin{aligned}
 \mathcal{L} = & B\{m(q_1 q_2) | m_W, \Gamma_W\} \cdot B\{m(l\nu) | m_W, \Gamma_W\} \cdot \\
 & B\{m(q_1 q_2 b_{\text{had}}) | m_t, \Gamma_{\text{top}}\} \cdot B\{m(l\nu b_{\text{lep}}) | m_t, \Gamma_{\text{top}}\} \cdot \\
 & W(\tilde{E}_{\text{jet}_1} | E_{b_{\text{had}}}) \cdot W(\tilde{E}_{\text{jet}_2} | E_{b_{\text{lep}}}) \cdot W(\tilde{E}_{\text{jet}_3} | E_{q_1}) \cdot W(\tilde{E}_{\text{jet}_4} | E_{q_2}) \cdot \\
 & W(\tilde{E}_x^{\text{miss}} | p_{x,\nu}) \cdot W(\tilde{E}_y^{\text{miss}} | p_{y,\nu}) \cdot \begin{cases} W(\tilde{E}_l | E_l), & e + \text{jets channel}, \\ W(\tilde{p}_{T,l} | p_{T,l}), & \mu + \text{jets channel}. \end{cases}
 \end{aligned} \tag{4.1}$$

Therefore, the likelihood \mathcal{L} is maximised by permuting the assignment of measurement outcomes and particles. It is also possible to add additional terms to the likelihood representing information like the b -tagging.

4.3. Profile Likelihood Unfolding with TRExFitter

The measured distributions of observables are often distorted because of limited acceptance and resolution in the detectors. That is why the true distribution of a measured observable cannot be accessed directly but via an inverse process called unfolding. To do so, one can simulate the true distribution based on a model assumption and construct the simulated measured distribution. From this distribution, the unfolding is performed to cancel distortions out and the same unfolding process can then be applied to real measured distributions. The relation between the measured and true distribution with the unfolding process is presented in Fig. 4.2.

The unfolding performed in this thesis is a profile likelihood unfolding (PLU) based on a profile likelihood fit with TRExFitter. For the PLU, the response matrix consisting of the selection efficiency, migration matrix and acceptance as well as the truth distribution is necessary (see Ch. 5.2.2). In the following, the truth distribution means the parton level distribution. The idea is then to fold each truth bin with the response matrix to obtain one reconstructed distribution for each truth bin and assign one normalisation factor to each folded truth bin. The N_{bins} reconstructed distributions are then fitted to the data

4. Experimental Techniques

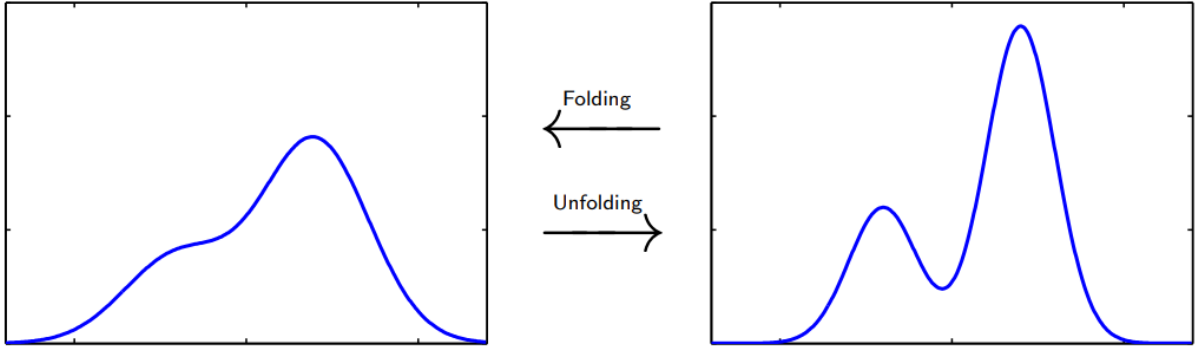


Figure 4.2.: Visualisation of unfolding and folding. On the left side the measured distribution is shown and on the right side the true one. The measured distribution is smeared compared to the true distribution due to resolution effects.

with the binned profile likelihood fit. As a result, the normalisation factors are obtained. These normalisation factors are applied to the truth distribution to receive the unfolded distribution.

The binned profile likelihood that is maximised in the fitting process by TRExFitter is defined as

$$\mathcal{L}(n|\theta, k) = \prod_i P(n_i | S_i(\theta, k) + B_i(\theta, k)) \cdot \prod_j G(\theta_j), \quad (4.2)$$

where n_i represents the data in the i -th bin, θ_i the constrained parameters, so the nuisance parameters associated to systematic uncertainties and k_i the unconstrained parameters, so parameters of interest and unconstrained nuisance parameters. $P(n_i | S_i(\theta, k) + B_i(\theta, k))$ yields the likelihood of a Poisson distribution with an expectation value based on the signal and the background to take the value of the data n . $G(\theta_j)$ is the constraint term which represents constraints on the nuisance parameters based on knowledge already obtained (for example with Gauß or Breit-Wigner distributions). Like this, the unfolding problem is simplified to a regular profile likelihood fit. In this thesis, only Asimov fits are performed, i.e. there is no data used for the unfolding and it is replaced by the truth distribution.

5. Sensitivity Study for the Observation of Spin Correlations

To investigate spin correlations in $t\bar{t}$, first possible c -tagging criteria are analysed to identify the charm jet and the strange jet associated with the same W boson. Subsequently, the observables sensitive to spin correlations are studied with respect to the quality of the reconstruction and the spin sensitivity. Lastly, the relevant spin coefficients are extracted from the distribution via fitting or unfolding and the achieved sensitivity is analysed.

For the analysis, a $t\bar{t}$ signal sample generated with POWHEG [33]+PYTHIA [34, 35] as Monte Carlo generators based on Run 2 in 2018 is used.

5.1. Investigation of possible c -tagging WPs

For the analysis of spin correlations in the lepton+jets channel, the strange quark as a spin analyser needs to be identified. To achieve this, suitable signal regions are defined with the help of the b -tagger DL1r and the flavour reconstruction evaluated.

5.1.1. Preparation

To identify semi leptonic decays of $t\bar{t}$ with certainty, a preselection is applied. An electron+jets (muon+jets) event is selected if

- it passes the single lepton trigger,
- there is exactly one electron (muon) with $p_T > 28$ GeV,
- the selected electron/muon matches the trigger,
- it passes the loose jet cleaning,
- there are at least four jets with $p_T > 25$ GeV,

5. Sensitivity Study for the Observation of Spin Correlations

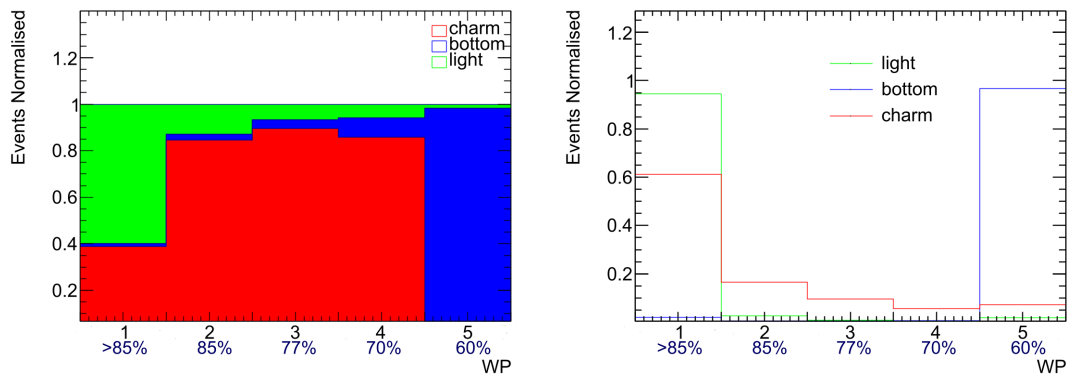


Figure 5.1.: Efficiency and purity of the DL1r WPs. On the left side the purity split into light, b and c jets is shown, on the right side the efficiency for the same jets. Based on these plots, the c -tag criteria are formulated.

- there are at least two jets at the 60% DL1r WP,
- and there is no bad muon.

The electron trigger is passed if the electron has a transverse energy $E_T > 26$ GeV, tight ID criterion without impact parameter and a loose isolation criterion, or $E_T > 60$ GeV and a medium ID criterion without impact parameter, or $E_T > 140$ GeV and a loose ID criterion without impact parameter. In contrast, the muon trigger is passed if the muon has either $E_T < 26$ GeV and a medium isolation criterion or $E_T > 50$ GeV.

The c -tagging WPs are based on the continuous b -tagging WPs of DL1r (shown in Tab. 4.1) where possible mistags in the looser WPs are used. To investigate the possible c -tagging WPs, the efficiency of the WP regarding each flavour, namely the fraction of jets classified in a certain WP, is of interest to estimate the remaining statistics. Another parameter of interest is the purity of the WP regarding the favoured flavour. In Fig. 5.1, it can be seen that the tightest WP has a high b purity as expected while hardly any b jets in the other WPs can be found. That is expected since the preselection for the $t\bar{t}$ process is at least two jets at the tightest WP, which should be the required truth b jets for a $t\bar{t}$ decay. The first WP has a high fraction of light jets (u, d, s or g), what is expected since they are the most different to b jets and therefore not that often mistagged. But the most interesting WPs for performing c -tagging are the WPs 2 – 4, which have a high fraction of c jets and can be used as a suitable c -tag criterion. Looking at Fig. 5.1, the majority of c jets will not be selected since they are sorted into the first WP but there are still a sufficient number of c jets in the relevant WP.

	c tag WP	s WP	jet multiplicity
SR 0	2	1	4
SR 1	2	1	5+
SR 2	3	1-2	4
SR 3	3	1-2	5+
SR 4	4	1-3	4
SR 5	4	1-3	5+

Table 5.1.: SR definition based on DL1r WPs and jet multiplicity.

5.1.2. Signal Regions

Based on the results from the WP analysis, three different c -tag criteria representing the three relevant DL1r WPs were designed. For orthogonal signal regions (SRs), the WP of the associated jet with the c -tagged jet is required to be looser than the c -tag WP. A more precise definition of the SRs can be achieved by differentiating between events with exactly 4 jets or more than 4 jets. The expectation based on the Feynman diagram is 4 jets but there can be more jets due to initial or final state radiation. It is reasonable to differentiate between those cases because the possibilities of KLFitter mismatching the jets increases with the jet multiplicity. A summary of the SRs is presented in Tab. 5.1.

The respective fiducial region on parton level is defined as the region with exactly one truth c jet and exactly one electron or muon. These particles are the products of the top quark decaying to a W boson, which then decays either leptonically or hadronically.

Having defined the SRs, the reconstruction efficiency is investigated by checking the truth flavour of the jets tagged as charm or assigned as strange. In Fig. 5.2, the truth `pdgId` of the c -tagged particles in the different SRs is shown. As expected, the majority of jets truly are c jets (`pdgId= 4`) but there is a non-negligible part of b jets (`pdgId= 5`) or gluons (`pdgId= 21`). Looking at the mistags, the case of c -tagging a b jet, the associated jet could still be an s or d jet carrying spin information whereas c -tagging a gluon means that the W boson was not reconstructed correctly because a W cannot decay into a gluon. Consequently, also the spin observables are negatively affected.

When a jet is c -tagged, the other jet that is assigned to the same W as the c -tagged jet according to KLFitter is assumed to be the s jet (`pdgId=3`). Looking at the true composition of the associated jets in Fig. 5.3, it can be seen that less than 50% are assigned correctly. If the assumed s jet truly is a d jet (`pdgId= 2`), the spin analysis is not affected because down quarks have the same spin analysing power as strange quarks, the W decay to c and s is simply more likely to occur than to c and d because of the CKM matrix elements. But the biggest contribution of falsely as strange reconstructed particles are

5. Sensitivity Study for the Observation of Spin Correlations

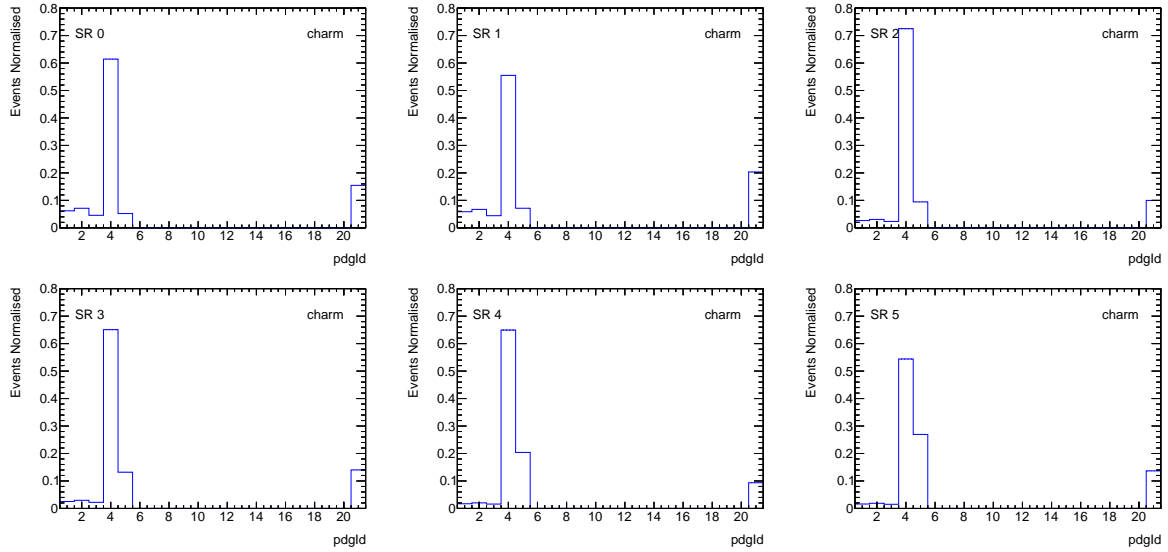


Figure 5.2.: Truth $pdgId$ of the c -tagged jets in the SRs. The truth c jets form the highest contribution which indicates a good reconstruction efficiency. But there are also events where a gluon was c -tagged and therefore, the W boson was not reconstructed correctly.

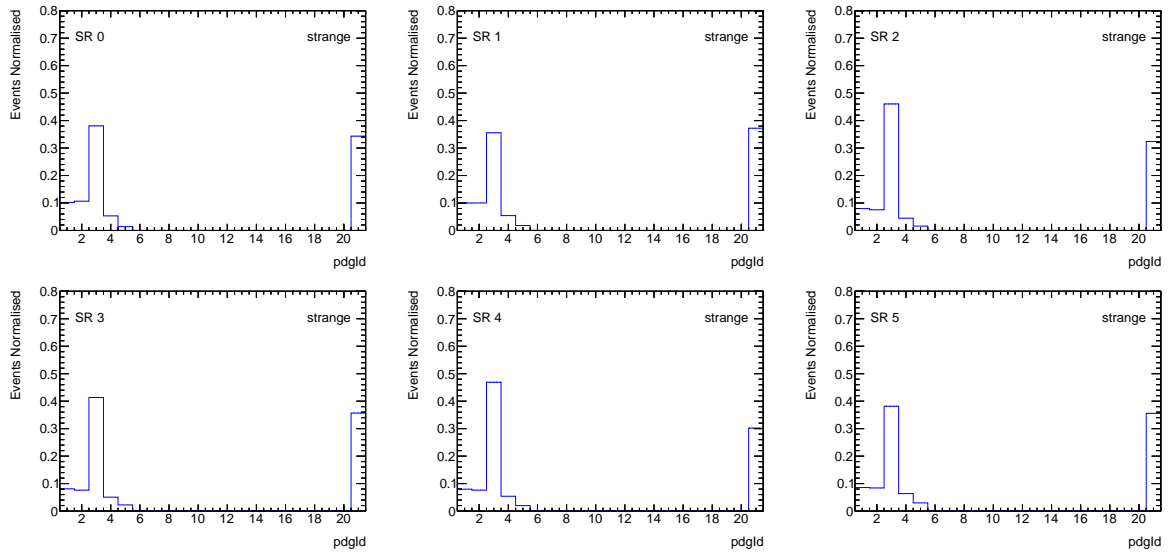


Figure 5.3.: Truth $pdgId$ of the associated jets in the SRs. The reconstruction efficiency for the s jet is not as good as for the c jets since there is a high contribution of gluons where the W boson was not reconstructed correctly.

the gluons, which do not carry the right spin information. Since the strange quark is one of the spin analysers next to the charged lepton, a false reconstruction affects the distribution of the observables directly. That is one of the reason why unfolding is performed later.

5.2. Investigation of Spin Observables

The observables introduced in Ch. 2.2.5 are analysed with respect to the truth/ reconstruction agreement and the spin sensitivity. As a result, the spin coefficients are extracted by fitting the distributions. Moreover, the background for the $t\bar{t}$ signal for the observables is analysed.

5.2.1. Construction of the Observables

The $\Delta\phi$ observable is easily constructed by taking the absolute value of the difference between ϕ_s and ϕ_l and normalising it with respect to π so that the result is between 0 and 1. For the observables in the helicity basis, the particles are first boosted to the $t\bar{t}$ rest frame and to their parent top's rest frame. Then, the unit vectors of the particles are determined to construct the right angles between the particles.

5.2.2. Reconstruction

To evaluate if the c -tagging approach is working for the reconstruction of the spin sensitive observables, the agreement between the distributions on truth and reconstruction level are compared and the migration matrix is analysed. The migration matrix is a $N_{\text{bins}} \times N_{\text{bins}}$ matrix with the truth observable on the vertical axis and the reconstructed observable on the horizontal axis and the number of entries on the z axis. Therefore, every entry in the matrix is an event that is in both the fiducial region and a signal region as defined in Ch. 5.1.2, which means that the reconstruction algorithm correctly identified the event. But it does not necessarily mean that the observable was reconstructed correctly. Since the rows of the matrix are normalised to 1, the fraction of truth events that are reconstructed in the corresponding bin is shown on the diagonal. But still, the number of bins is finite (and the width not infinitesimal) so the diagonal entries depend on the choice of bins which is used in the rebinning process later.

Other quantities to determine the quality of the reconstruction are the efficiency ϵ and the acceptance a . They are defined as

$$\epsilon = \frac{\text{\#events generated in fiducial region and reconstructed in SR}}{\text{\#events generated in fiducial region}}, \quad (5.1)$$

$$a = \frac{\text{\#events reconstructed in the SR and generated in fiducial region}}{\text{\#events reconstructed in SR}} \quad (5.2)$$

and are also important for the unfolding. The efficiency, migration matrix and acceptance can be combined to form the response matrix that is then used for the unfolding.

5. Sensitivity Study for the Observation of Spin Correlations

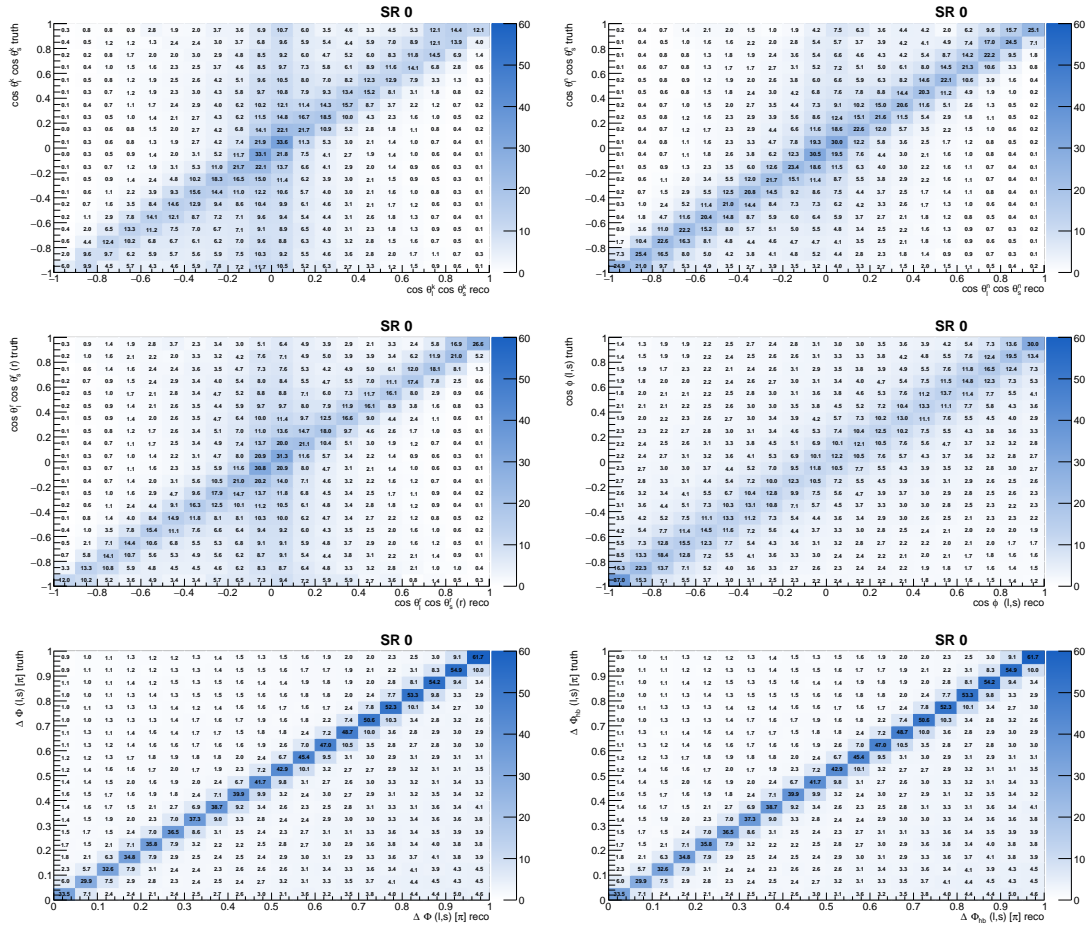


Figure 5.4.: Migration matrix for the different observables in SR 0. It can be seen that the migration is not very diagonal.

In Fig. 5.4, the migration matrices with 20 bins on each axis for the different observables for SR 0 are shown but it can be observed that the matrix is not as diagonal as desired. The $\Delta\phi$ observables show a migration to lower values for the reconstruction while the $\cos\theta_l \cos\theta_s$ observables have a migration of events to 0 and the migration for $\cos\varphi$ seems to be smeared. For the unfolding process later, a diagonal migration matrix is important to simplify the fit performed and to make sure that it converges. That is the reason why the histograms are rebinned so that bins where migration happens are merged. For the $\Delta\phi$ and $\cos\varphi$ observables, the bins are merged until the diagonal bin reaches a fraction of 50%, while for the $\cos\theta_l \cos\theta_s$ observables a different approach is chosen. Because the analytical formula Eq. (2.9) diverges at 0, it is set as a bin edge and the two halves are optimised separately with respect to the sum of the diagonal entries. The first rebinning approach resulted in three bins for the $\cos\theta_l \cos\theta_s$ observables, therefore the expectation

5.2. Investigation of Spin Observables

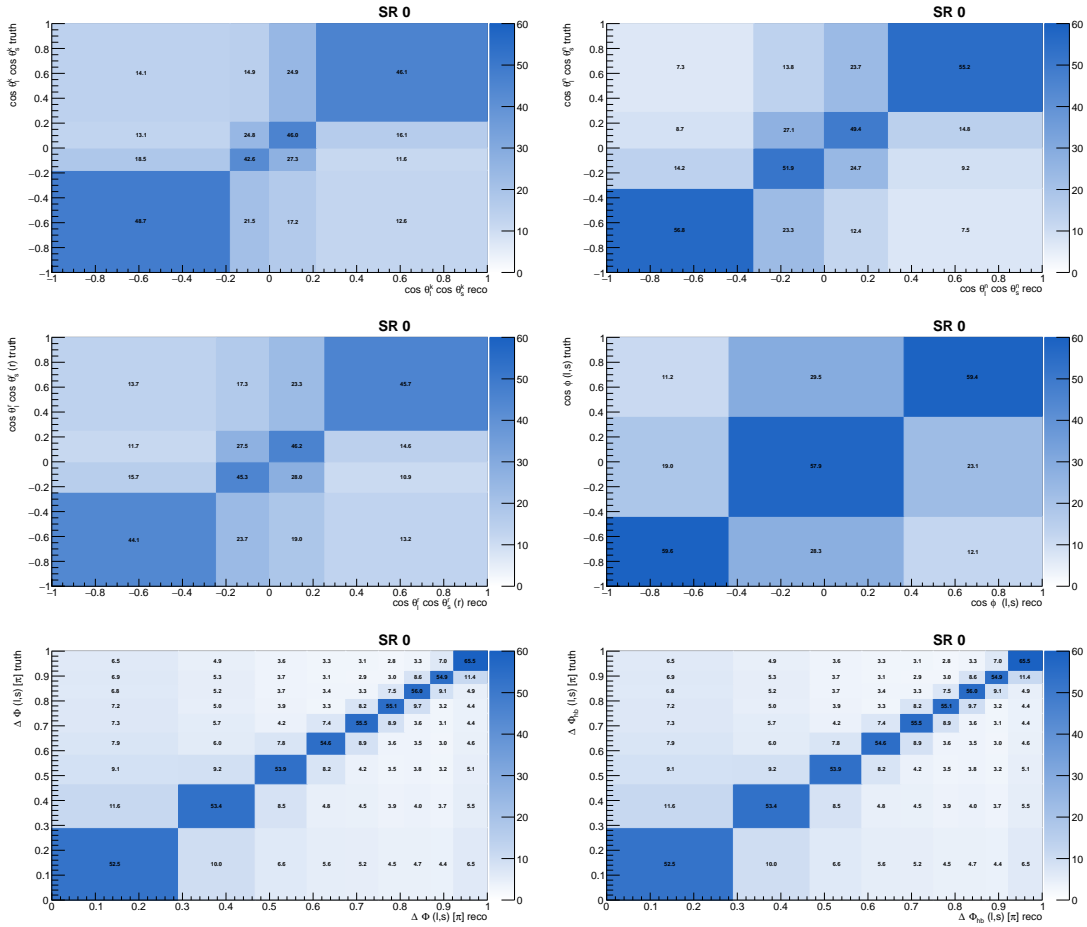


Figure 5.5.: Migration matrix for the observables in SR 0 rebinned. The other SRs are shown in App. A.1. The observation is that the rebinning clearly improved the diagonality.

was to aim for a total of four bins, two per half. For these processes, the SRs are considered simultaneously to gain a single suitable binning per observable. The results for the rebinning presented in Fig. 5.5 show a more diagonal matrix. In conclusion, the difficulties of the migration matrix illustrated in Fig. 5.4 were improved with the adjusted binning, which will be used for this analysis.

The efficiency and acceptance described in Eq. (5.1) and Eq. (5.2) are displayed in Fig. 5.6 and Fig. 5.7 for SR 0. In addition to the migration matrices, the comparison between the truth and reconstructed distribution is considered for the evaluation. In Fig. 5.8, the contrast already seen in the migration is shown.

The bad agreement between the truth and the reconstructed distribution can be a result of a misidentification in the c -tagging in the first place or a mismatch of KLfitter, like

5. Sensitivity Study for the Observation of Spin Correlations

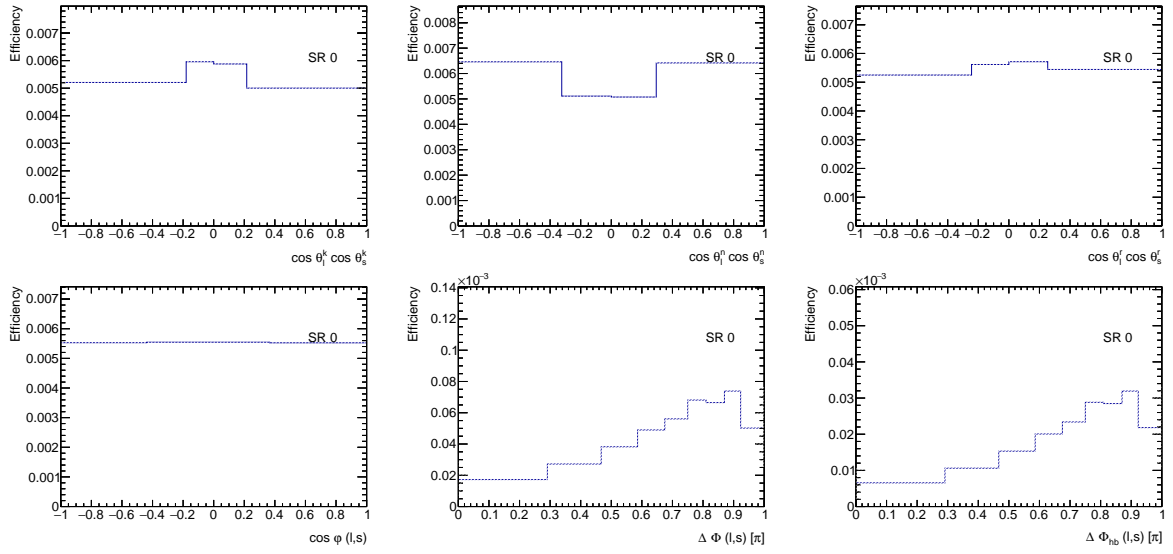


Figure 5.6.: Selection efficiencies for the observables in SR 0. The other SRs are shown in Ch. A.3.

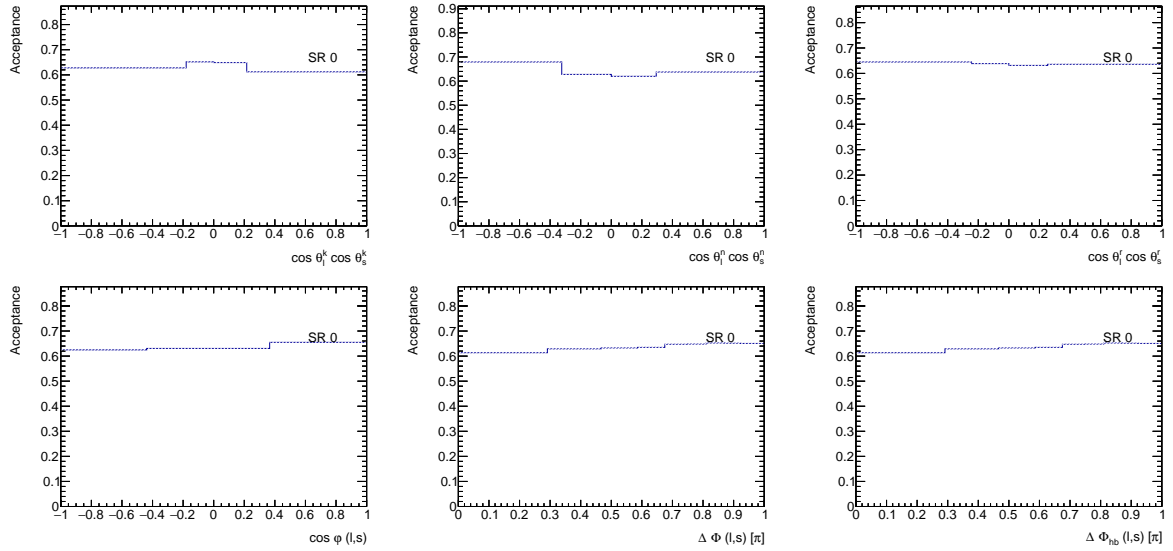


Figure 5.7.: Acceptance for the observables in SR 0. The other SRs are shown in App. A.4.

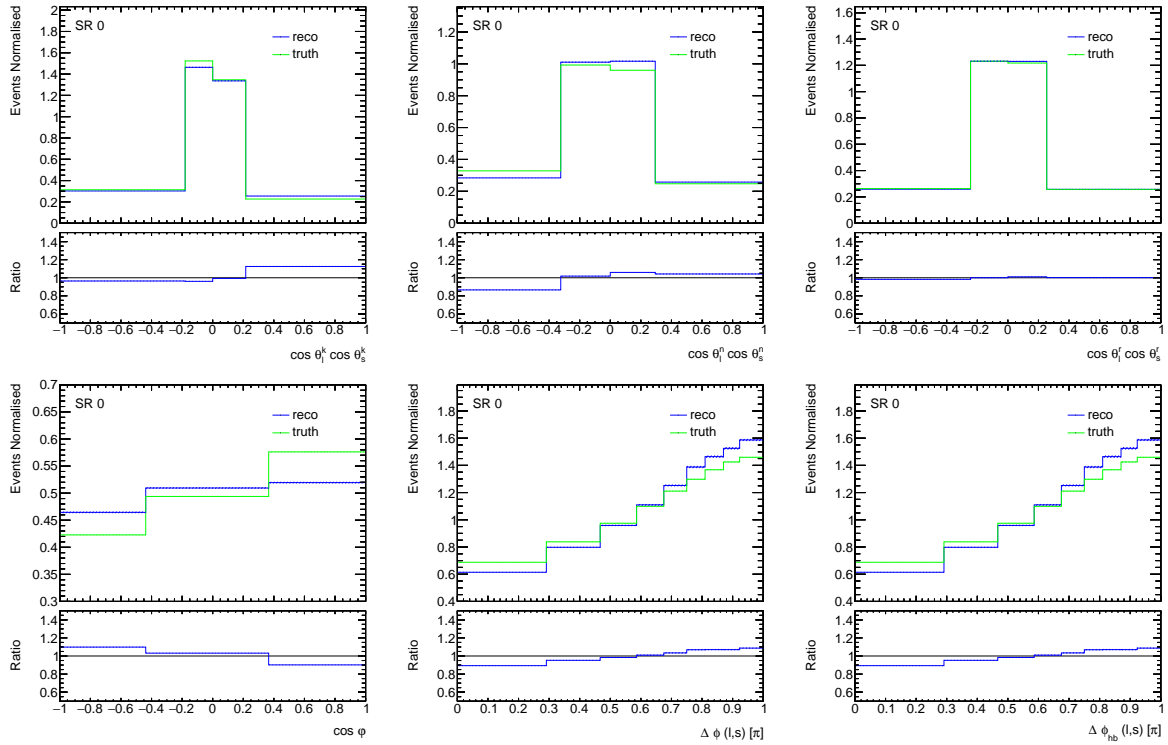


Figure 5.8.: Comparison between truth distribution and reconstructed distribution in SR 0. The other SRs are shown in App. A.2. It is shown that there is a discrepancy between the truth and reconstructed distribution which agrees with the migration effects observed.

already discussed in Ch. 5.1, or effects due to the detectors. But in the either case, the unfolding is performed since the analytical formula to fit the distribution is defined for the truth distribution and the bad agreement does not disrupt the analysis.

5.2.3. Spin Sensitivity

As described in Ch. 2.2.4, the charm quark has a low spin analysing power and is therefore not sensitive to spin correlations. Consequently, the distributions for the charm and strange quarks are expected to differ. The differences can be seen in Fig. 5.9 and the plots support the hypothesis that charm and strange quark behave differently when it comes to spin sensitive observables. For these plots, the bin width is considered when calculating the ratio histogram because the histograms for the charm and strange quark have different bin edges. That is because the observables have migration effects of different strength that create different results in the rebinning.

5. Sensitivity Study for the Observation of Spin Correlations

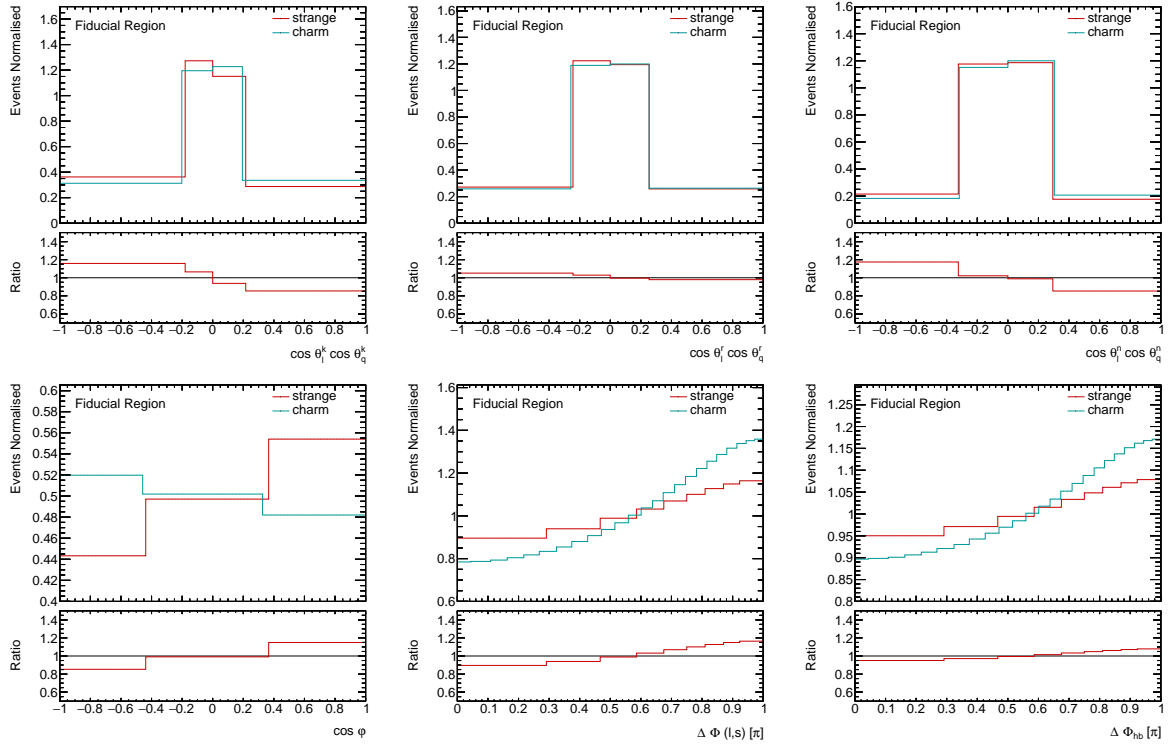


Figure 5.9.: Comparison of c and s distribution for the different observables. The distributions differ due to the different spin sensitivity.

In general, down type particles like the strange quark tend to have smaller transverse momentum than up type particles like the charm due to the parity violating W decay. The same applies to the up type ν and down type charged lepton in a leptonic W decay. Since there is a preselection cut on the p_T in the samples used for the reconstruction and cutting out more strange than charm jets could be the reason for the difference in the distributions, the truth momentum distribution and the observable distribution without this cut is analysed. In Fig. 5.10, the p_T of the strange and the charm in comparison and the neutrino and the charged lepton are shown since the neutrino is as well an up type particle and the charged lepton a down type one. It can be observed that the assumption stated in the beginning is plausible with these plots. In total, 90.33% of the charm jets have a $p_T > 25$ GeV whereas only 84.28% of the strange jets do.

The distributions of charm and strange on truth level (see Fig. 5.9) without any cuts still show differences which indicates that the differences originate from the different spin analysing powers.

For the $\Delta\phi$ observables, the spin sensitivity is expected to vanish with higher values

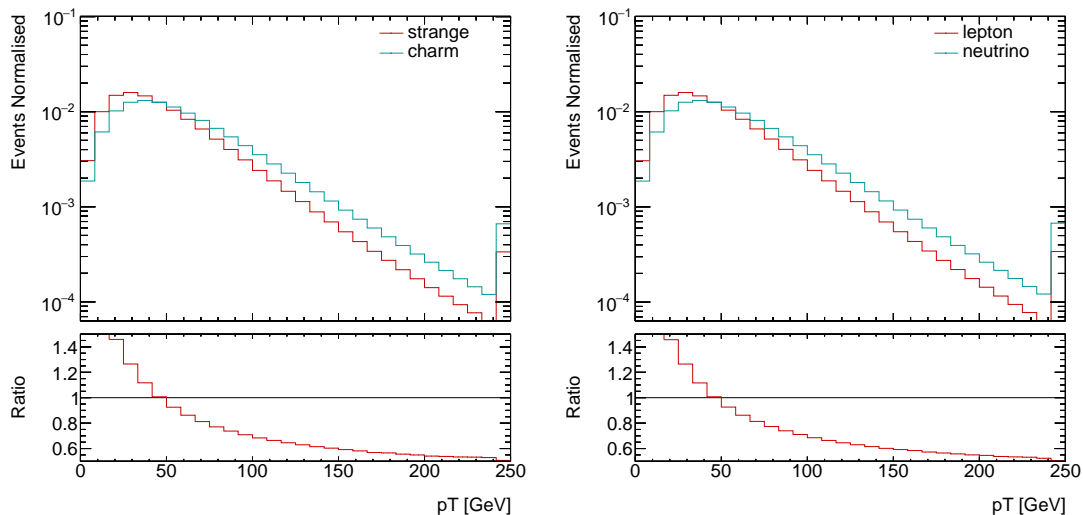


Figure 5.10.: Comparison of the p_T of down and up type particles. The last bin shows the overflow of particles with $p_T > 250$ GeV. The distributions differ because the down type particles tend to have a smaller p_T .

of $m_{t\bar{t}}$ and there is no analytical formula to fit and therefore, these observables will not be investigated further.

5.2.4. Fitting

As described in Ch. 2.2.5, the spin coefficients can be extracted from the distributions of the spin observables by fitting the analytical formula. With these coefficients and their uncertainty, information about the spin correlations is gathered. The analytical formula for the $\cos\varphi$ distribution described in Eq. (2.11) shows a linear relation, so this distribution can be fitted directly. In contrast, Eq. (2.9) points out a non-linear relation that complicates fitting because the middle of the bin is used for the fit, which does not represent the real bin centre based on the function to fit. That is the reason why a bin centre correction is applied before fitting the $\cos\theta_l \cos\theta_s$ distributions.

The fit performed for the histograms is a χ^2 fit where the χ^2 defined as

$$\chi^2 = \sum_{i=1}^{N_{\text{bins}}} \frac{(y_i - f(x_i))^2}{\sigma_i^2}$$

is minimised. N_{bins} represents the number of bins, y_i is the yield of the i -th bin, $f(x_i)$ the analytical function at the bin centre x_i and σ_i the uncertainty. To evaluate the quality of the fit, χ^2/ndf is calculated, where ndf means the number of degrees of freedom, which is equal to $N_{\text{bins}} - 1$ in this case.

5. Sensitivity Study for the Observation of Spin Correlations

The bin centre correction is based on a binary search algorithm to find the point between the bin edges where the integral of the function reaches 50% with respect to the total bin integral. But for a meaningful result a nominal value for the C parameter is required. To determine the expected parameter values precisely, the truth histogram to fit is produced with a fine binning. Then, the bin centre correction is obsolete because the bin width is small compared to the range of the function. In Tab. 5.2, the fit results, the means of the histograms (which are independent of the binning) and the reference literature values [24] can be found. Reading off the table, it is visible that the fit results agree well with the means as expected what can also be seen in the plots in Fig. 5.11. The fit results resemble the literature values but they do not need to match the literature values exactly since the spin correlation is only approximately implemented in the generator.

parameter	fit result	χ^2/ndf	$-9 \cdot \langle \cos \theta_l \cos \theta_s \rangle$	literature
$C(k, k)$	$0.3141 \pm 5 \cdot 10^{-4}$	1.56	$0.3140 \pm 5 \cdot 10^{-4}$	0.326
$C(r, r)$	$0.0478 \pm 5 \cdot 10^{-4}$	1.65	$0.0477 \pm 5 \cdot 10^{-4}$	0.071
$C(n, n)$	$0.3175 \pm 5 \cdot 10^{-4}$	1.62	$0.3175 \pm 5 \cdot 10^{-4}$	0.331
D	$-0.2264 \pm 3 \cdot 10^{-4}$	-	$-0.2264 \pm 3 \cdot 10^{-4}$	-0.228

Table 5.2.: Fit results for $\cos \theta_l \cos \theta_s$ with fine binning compared to the literature values [24] and means of the histograms.

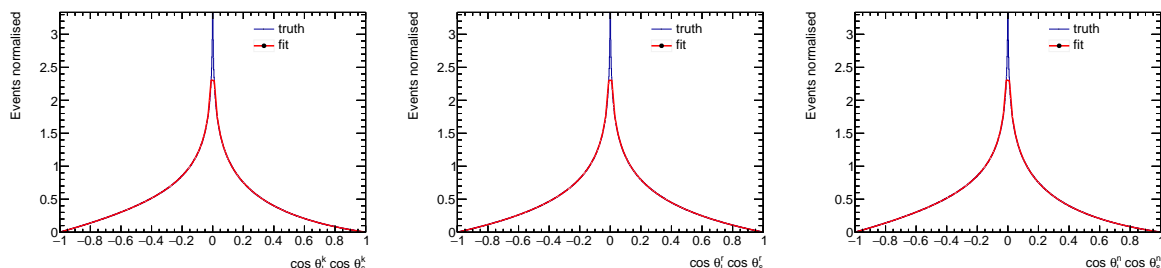


Figure 5.11.: The truth distribution plotted together with the fitted distribution for a fine binning. The two distributions agree well with each other.

In the next step, the bin centre correction based on the parameters obtained before was applied to the truth histograms with the regular binning. These histograms were then fitted and the results are displayed in Tab. 5.3. The fit parameters differ from the literature and the mean values due to the low number of bins. Moreover, it stands out that the χ^2/ndf is very high for the fit performed. To solve this, the mean is fitted with the unfolding instead, as described in Ch. 5.3.

Whereas the fitting of the $\cos \varphi$ observable is less complex since bin centre correction is

parameter	fit result	χ^2/ndf	literature
$C(k, k)$	$0.4005 \pm 4 \cdot 10^{-4}$	$2.67 \cdot 10^6$	0.326
$C(r, r)$	$0.0543 \pm 4 \cdot 10^{-4}$	$2.33 \cdot 10^6$	0.071
$C(n, n)$	$0.4283 \pm 4 \cdot 10^{-4}$	$1.67 \cdot 10^6$	0.331
D	$-0.2944 \pm 3 \cdot 10^{-4}$	-	-0.228

Table 5.3.: Fit results for $\cos \theta_l \cos \theta_s$ with regular binning compared to the literature values.

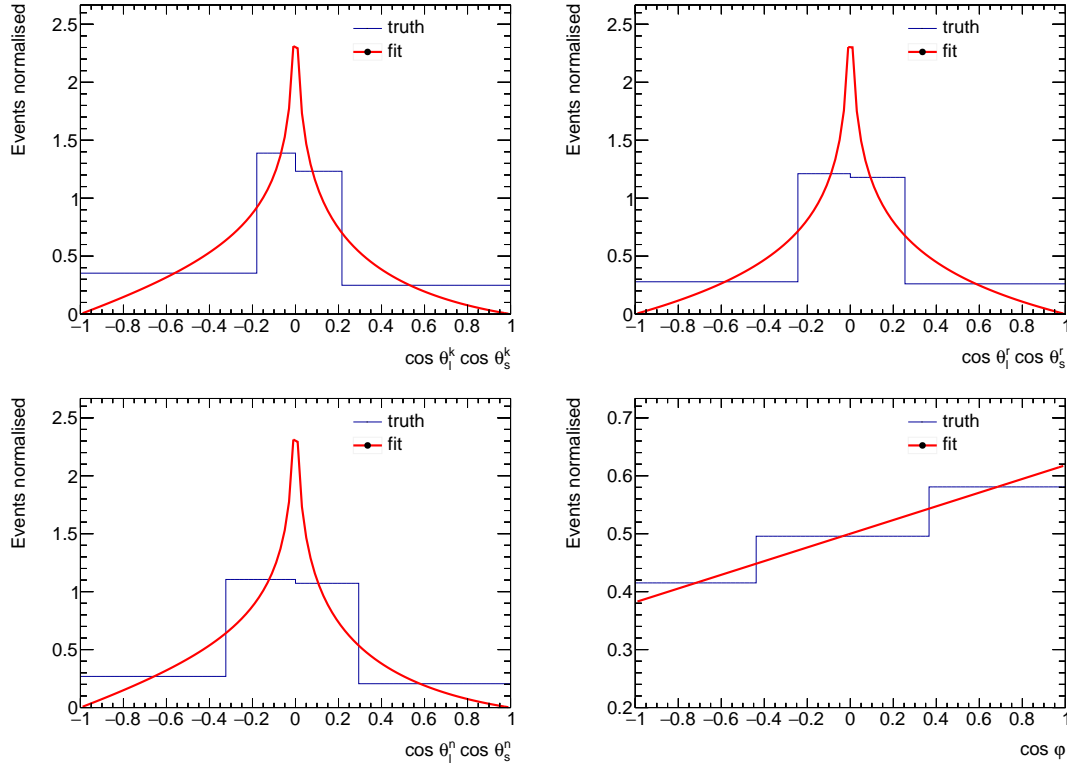


Figure 5.12.: The truth distribution plotted together with the fitted distribution for the regular binning. Due to the low number of bins, the distributions cannot be compared well.

not necessary and therefore the fit is performed directly. Tab. 5.4 shows that the fit result and mean of the histogram are in good agreement but the uncertainties are vanishingly small because no systematic uncertainties are included and the statistic ones are tiny for the truth distributions. In the unfolding described in Ch. 4.3, systematic uncertainties are considered and therefore more realistic uncertainties on the parameters are obtained.

5. Sensitivity Study for the Observation of Spin Correlations

parameter	fit result	χ^2/ndf	$-3 \cdot \langle \cos \varphi \rangle$	literature
D	$-0.2364 \pm 3 \cdot 10^{-4}$	0.60	$-0.2365 \pm 3 \cdot 10^{-4}$	-0.228

Table 5.4.: Results for the fitted parameter D from the $\cos \varphi$ truth distribution compared to the mean of the histogram.

5.2.5. Check with no Spin Correlations Sample

To assure that the spin correlation was extracted via the fit, the same process is repeated with a sample generated without spin correlations. The results displayed in Tab. 5.5 show a good agreement with the expectation of 0 as spin correlation coefficients. The fitted distributions are also displayed in Fig. 5.13.

parameter	fit result	χ^2/ndf	$\langle O \rangle$
$C(k, k)$	$0.0530 \pm 8 \cdot 10^{-4}$	$0.5 \cdot 10^6$	$(1 \pm 1) \cdot 10^{-3}$
$C(r, r)$	$(36 \pm 8) \cdot 10^{-4}$	$0.4 \cdot 10^6$	$(1 \pm 1) \cdot 10^{-3}$
$C(n, n)$	$0.08559 \pm 8 \cdot 10^{-4}$	$3 \cdot 10^5$	$(1 \pm 1) \cdot 10^{-3}$
D	$(7 \pm 6) \cdot 10^{-4}$	0.09	$(4 \pm 6) \cdot 10^{-4}$

Table 5.5.: Fit results for fitting the sample without spin correlations.

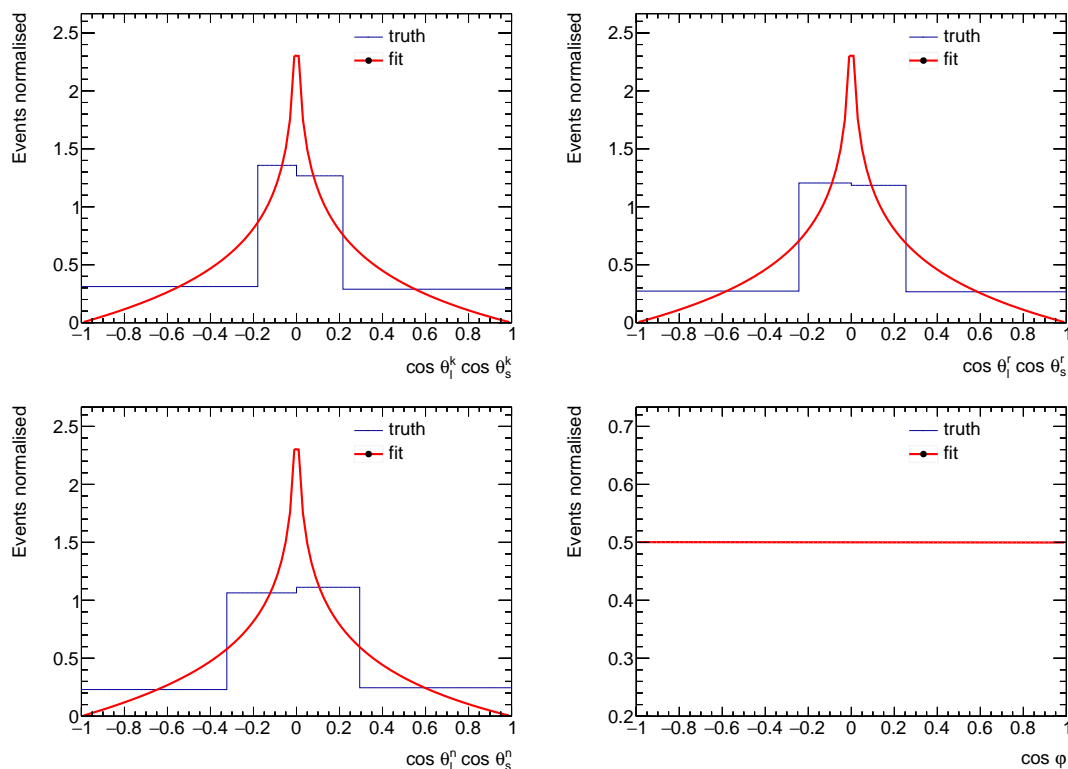


Figure 5.13.: The truth distribution plotted together with the fitted distribution for the sample without spin correlations. For the $\cos \varphi$ distribution, it is visible that the parameter is close to 0 as expected.

5.2.6. Background

In general, the background processes are characterised by having the same final states as the signal process what makes it impossible to distinguish between them on particle level but since the process is different, the results extracted from those distributions are incorrect. For the $t\bar{t}$ signal in the lepton+jets channel, the final states are two b jets, one charged lepton, one neutrino and at least two other jets. The relevant background processes are:

- **Diboson Production:** One of the bosons has to decay leptonically while the other one has to decay hadronically and there have to be two b jets in the final state to imitate the $t\bar{t}$ signal in the lepton+jets channel. The samples were produced with POWHEG +PYTHIA.
- **Single Top Production:** In the s and t production channel, the W from the top decay has to decay leptonically whereas in the tW channel, either the W from the top or the associated W has to decay leptonically and the other one hadronically.

5. Sensitivity Study for the Observation of Spin Correlations

In addition, there has to be a second b jet. Again, these samples were generated with POWHEG +PYTHIA.

- $t\bar{t} + H, t\bar{t} + W, t\bar{t} + Z$: For the $t\bar{t} + X$ processes, exactly one of the three bosons (two W from the $t\bar{t}$ decay and the additional H, W or Z) has to decay to leptons and the other two to hadrons. The $t\bar{t} + H$ was produced with POWHEG +PYTHIA, whereas the $t\bar{t} + W$ with SHERPA [36] and $t\bar{t} + Z$ with MADGRAPH5_AMC@NLO [37]+PYTHIA.
- **W +Jets and Z +Jets**: In this case, the boson has to decay to leptons and among the jets, there have to be two b jets. The SHERPA generator was used for these samples.

But still, events can be reconstructed incorrectly and the number of background events considered may vary.

The results are presented in Tab. 5.6 where the different background process contributions for the different observables can be seen. The distribution is similar for the different observables but the $t\bar{t}$ signal clearly forms the biggest contributions since the signal to background ratio has a value of about ~ 0.92 .

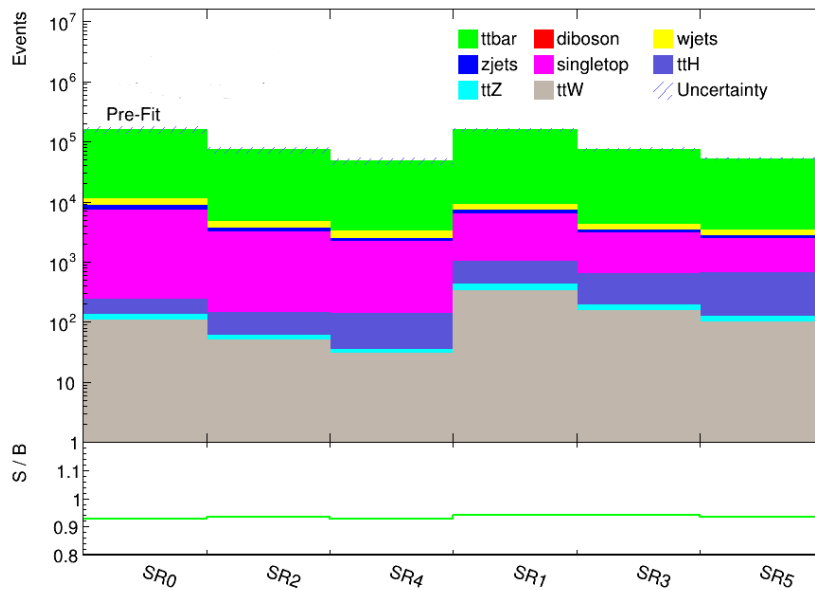


Figure 5.14.: Summary plots for the 6 SR of the signal and background yields.

	SR0	SR1	SR2
diboson	35.0 ± 3.1	19.1 ± 1.6	12.5 ± 0.9
W +jets	$2,710 \pm 220$	$2,020 \pm 170$	$1,110 \pm 90$
Z +jets	$1,440 \pm 140$	910 ± 80	457 ± 33
single top	$7,000 \pm 400$	$5,260 \pm 340$	$3,030 \pm 190$
$t\bar{t} + H$	108.0 ± 3.0	624 ± 22	83.5 ± 2.6
$t\bar{t} + Z$	23.0 ± 1.2	95 ± 6	10.1 ± 0.6
$t\bar{t} + W$	110 ± 6	335 ± 19	51.0 ± 2.9
$t\bar{t}$	$147,000 \pm 18,000$	$150,000 \pm 12,000$	$70,000 \pm 9,000$
Total	$159,000 \pm 19,000$	$159,000 \pm 12,000$	$74,000 \pm 10,000$
	SR3	SR4	SR5
diboson	7.2 ± 0.5	8.6 ± 0.5	5.47 ± 0.34
W +jets	860 ± 60	820 ± 60	700 ± 50
Z +jets	334 ± 24	333 ± 23	248 ± 15
single top	$2,420 \pm 140$	$2,040 \pm 130$	$1,800 \pm 110$
$t\bar{t} + H$	447 ± 15	106.9 ± 3.5	539 ± 19
$t\bar{t} + Z$	42.3 ± 2.5	5.7 ± 0.4	26.2 ± 1.6
$t\bar{t} + W$	156 ± 9	30.2 ± 1.9	101 ± 6
$t\bar{t}$	$72,000 \pm 5,000$	$45,000 \pm 6,000$	$49,700 \pm 3,100$
Total	$76,000 \pm 5,000$	$48,000 \pm 6,000$	$53,100 \pm 3,300$

Table 5.6.: Yields of the analysis for the different SRs. The yields are the same for every observable since the distribution is not considered.

5.3. Unfolding

As already described in Ch. 4.3, the reconstructed distributions are unfolded to match the truth distribution and to enable the extraction of meaningful coefficients. Thereby, the uncertainties are particularly important because they show the sensitivity achieved in the analysis. Therefore, different systematics are included.

5.3.1. Closure Test

To test if the unfolding is working reliably, a k-folding test is performed. For that, the same distributions are generated again, but split into histograms with even event numbers and odd event numbers. Thus, two statistically independent histograms were created. Then, the response matrix derived from events with an even event number are unfolded with the truth histogram containing the odd events and vice versa. The unfolded distributions are expected to match the truth distribution within the range of the statistical uncertainty. The results from Fig. 5.15 confirm this expectation.

5. Sensitivity Study for the Observation of Spin Correlations

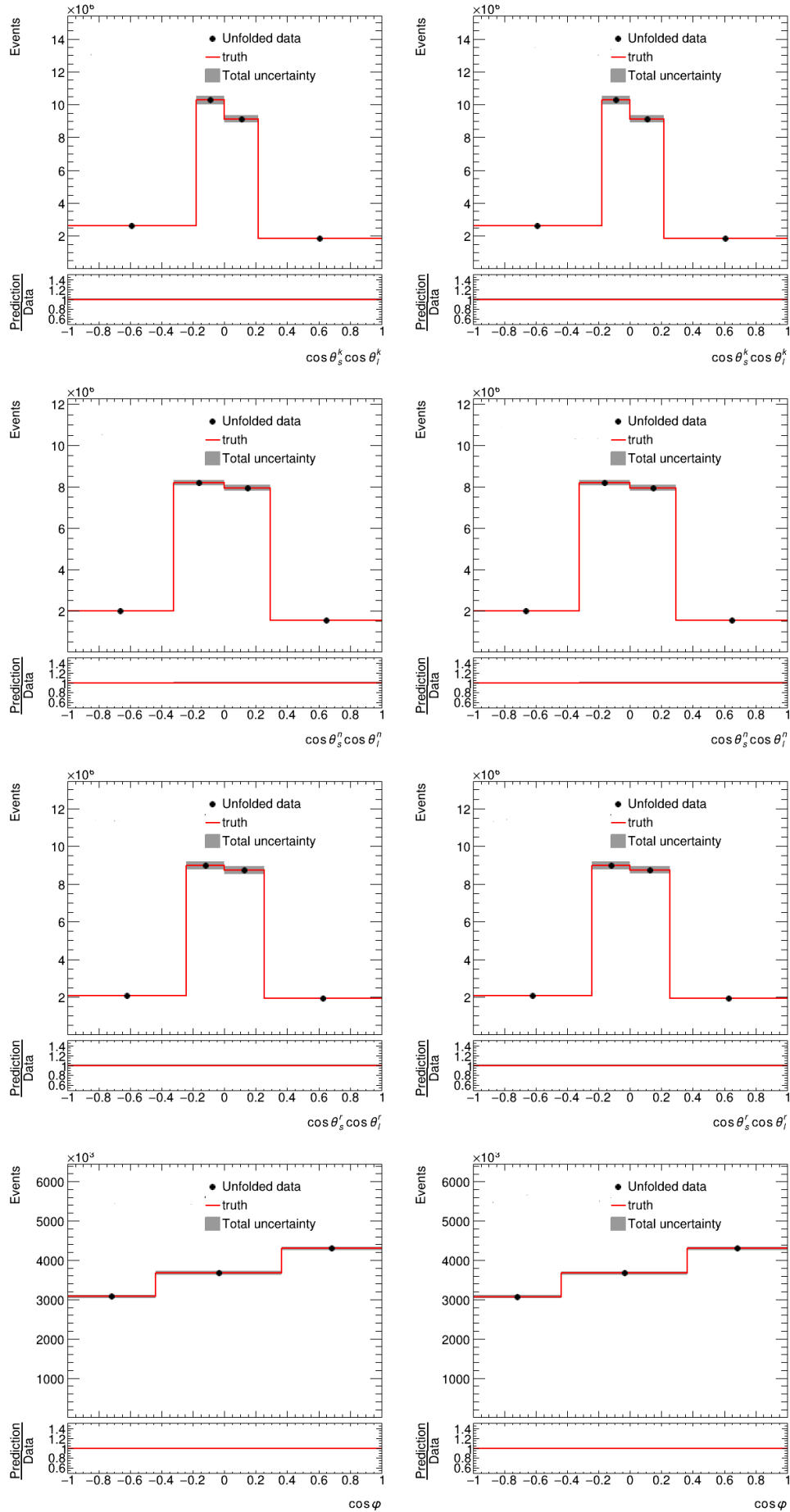


Figure 5.15.: Results from the k-folding test. On the right hand side the even response was used, on the left hand side the odd one. The results match well.

5.3.2. Results

The unfolded distributions with the corresponding uncertainties are shown in Fig. 5.17. Here, the six SRs are combined to one unfolded distribution. The truth distribution without spin correlations is also plotted to emphasise the difference to the distribution containing spin correlations.

In Fig. 5.16 and Tab. 5.7, the post-fit yields for the observables in the SRs are shown. As expected, only the uncertainties changed in comparison to Tab. 5.6, but they changed depending on the observable. A more detailed presentation of each SR and each observable can be found in App. A.5.

	SR0	SR1	SR2
diboson	35.0 ± 2.8	19.1 ± 1.5	12.5 ± 0.9
W +jets	$2,710 \pm 220$	$2,020 \pm 160$	$1,110 \pm 90$
Z +jets	$1,440 \pm 120$	910 ± 70	457 ± 34
single top	$7,000 \pm 400$	$5,260 \pm 330$	$3,030 \pm 190$
$t\bar{t} + H$	108.0 ± 3.2	624 ± 22	83.5 ± 2.8
$t\bar{t} + Z$	23.0 ± 1.2	95 ± 5	10.1 ± 0.6
$t\bar{t} + W$	110 ± 6	335 ± 19	51.0 ± 2.8
$t\bar{t}$	$147,000 \pm 5,000$	$150,000 \pm 5,000$	$69,700 \pm 2,400$
Total	$159,000 \pm 5,000$	$159,000 \pm 5,000$	$74,400 \pm 2,200$
	SR3	SR4	SR5
diboson	7.2 ± 0.5	8.6 ± 0.5	5.47 ± 0.35
W +jets	860 ± 60	820 ± 60	700 ± 50
Z +jets	334 ± 25	333 ± 23	248 ± 16
single top	$2,420 \pm 120$	$2,040 \pm 120$	$1,800 \pm 110$
$t\bar{t} + H$	447 ± 17	106.9 ± 3.2	539 ± 20
$t\bar{t} + Z$	42.3 ± 2.5	5.7 ± 3.2	26.2 ± 1.5
$t\bar{t} + W$	156 ± 9	30.2 ± 1.7	101 ± 6
$t\bar{t}$	$71,600 \pm 2,300$	$44,700 \pm 1,500$	$49,700 \pm 1,600$
Total	$75,800 \pm 2,200$	$48,100 \pm 1,400$	$53,100 \pm 1,500$

Table 5.7.: Yields of the analysis for the different SRs post-fit. As an example, only $\cos \varphi$ is shown since only the uncertainties change.

Since the spin coefficients are proportional to the means of the histograms (see Ch. 2.2.5), they can be extracted during the unfolding of the distributions. To achieve that, the

5. Sensitivity Study for the Observation of Spin Correlations

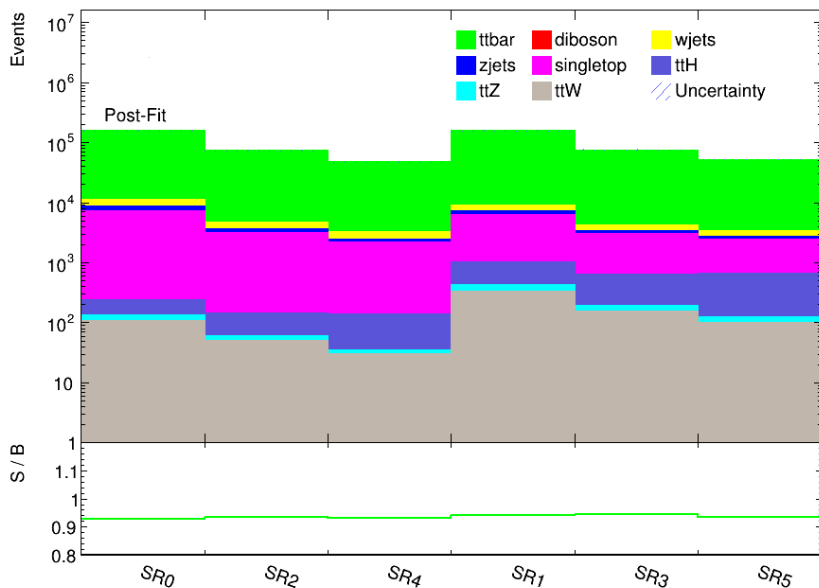


Figure 5.16.: Summary plots for the 6 SRs of the signal and background yields post-fit. As an example, only $\cos\varphi$ is shown since only the uncertainties change. A more detailed presentation of each SR and each observable can be found in App. A.5.

unfolding norm factor for the first bin μ_1 is redefined with respect to the mean $\langle O \rangle$ as

$$\langle O \rangle = \frac{\sum_{i=1}^{N_{\text{bins}}} x_i \cdot y_i \cdot \mu_i}{\sum_{i=1}^{N_{\text{bins}}} y_i \cdot \mu_i},$$

$$\Rightarrow \mu_1 = \frac{\sum_{i=2}^{N_{\text{bins}}} (x_i - \langle O \rangle) \cdot y_i \cdot \mu_i}{(\langle O \rangle - x_1) \cdot y_1}.$$

The x_i are the bin centres corrected according to the analytical function, as described in Ch. 5.2.4, the y_i are the bin yields of the truth distribution, N_{bins} is the number of bins and μ_i are the normalisation factors of the bin. Therefore, the mean and the corresponding uncertainties can be obtained directly from the fit. The results for the spin coefficients shown in Tab. 5.8 agree with the literature value within the range of uncertainty. The results are several σ intervals away from 0 meaning no spin correlations which indicates a good sensitivity. Here, the systematic uncertainties discussed in Ch. 5.3.3 are already included.

As described in Ch. 2.2.5, the D parameter from the $\cos\varphi$ distribution is sensitive to quantum entanglement for a $m_{t\bar{t}}$ window of < 390 GeV, hence the distribution is fitted

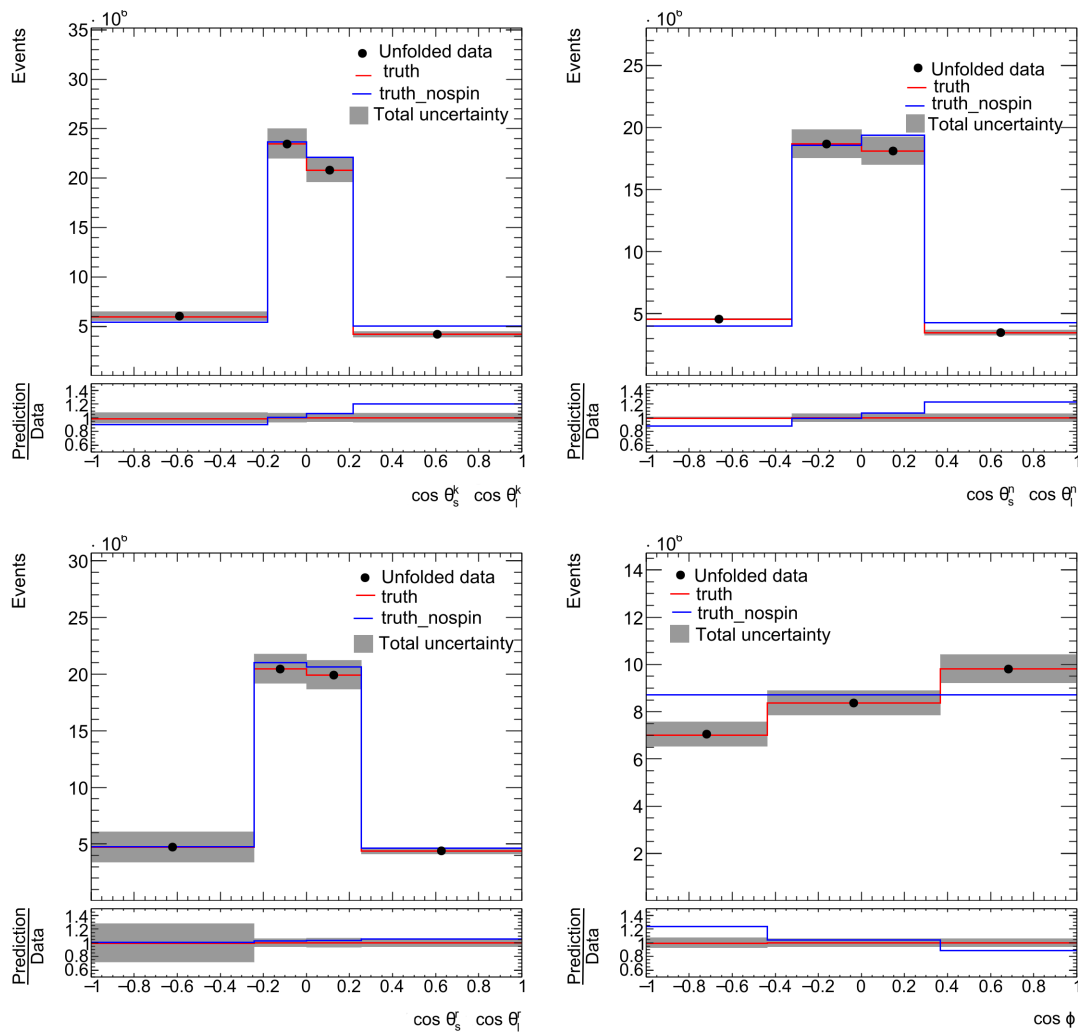


Figure 5.17.: Unfolding results with uncertainties for the different observables. The distribution without spin correlations is plotted for comparison.

with the right $m_{t\bar{t}}$ cut. The result of

$$D = -0.39 \pm 0.05 < -\frac{1}{3} \quad (5.3)$$

indicates entanglement with a significance of 1σ . The larger uncertainty could be due to the smaller number of events, which decreased to $\sim 17\%$ compared to the full $m_{t\bar{t}}$ range and consequently, the statistical uncertainty increased.

5. Sensitivity Study for the Observation of Spin Correlations

parameter	value	literature
$C(k, k)$	0.30 ± 0.02	0.326
$C(r, r)$	0.05 ± 0.02	0.071
$C(n, n)$	0.31 ± 0.01	0.331
D	-0.20 ± 0.01	-0.228

Table 5.8.: Results for the spin coefficients extracted with the unfolding norm factors. The results are several σ intervals away from 0 which equals a good sensitivity.

5.3.3. Systematic Uncertainties

When performing unfolding and extracting parameters, uncertainties are important to evaluate the significance of the results. The spin coefficients are affected by systematic uncertainties of which the most important are investigated in the following. A full investigation of every systematic cannot be provided in this thesis. Included in this analysis are:

- **Scale Systematics:** Theoretical scale variations based on models used for simulating this process, namely:
 - ISR and FSR - initial and final state radiation of gluons from the partons or the final state particles,
 - μ_R and μ_F - renormalisation and factorisation scale (for the running coupling α_S),
 - PDF - parton density function for the partons of the proton.

For these systematics, the same distributions were recreated with reweighted events. Precisely, for the ISR, FSR, μ_R and μ_F systematic for the up variation, the nominal value was doubled and divided in half for the down variation. For the PDF systematic, an alternative PDF variation was used [38].

- **b -Tagging Systematics:** Variations of the efficiency and calibration of the b -tagging algorithm. Like before, the distributions were generated again and scaled.
- **Generator Systematics:** Variations in the modelling process for different generators, namely:
 - $t\bar{t}$ parton shower,
 - $t\bar{t}$ matrix element.

For the generator uncertainties, the nominal sample generated with POWHEG +PYTHIA was compared to a POWHEG +HERWIG [39] sample for the parton shower systematic and to a MADGRAPH5_AMC@NLO +PYTHIA sample for the matrix element.

- **Background Cross Section Systematics:** Uncertainties on the cross section for the $t\bar{t} + W$, single top and $t\bar{t} + Z$ background processes.

The different systematics vary in their impact on the fit, which is displayed in Fig. 5.18. It stands out that especially the matrix element, parton shower and final state radiation systematic seem to have a big impact which was already expected. In Fig. 5.19, the overview of the pull distributions of the nuisance parameters is presented. The pull distribution is expected to be a Gaussian distribution with an expectation value of 0 and a standard deviation of 1. The nuisance parameter is constrained, meaning the pull distribution has a standard deviation smaller than 1, when the estimated uncertainty on the parameter does not match the uncertainty after the fit. This is the case for the parton shower, matrix element and FSR systematic. Since the systematic is based on variations of the nominal distribution, the difference can be measured and compared to the statistical uncertainty. If the shape difference is significantly outside the range of the statistical uncertainty, the uncertainty of the nuisance parameter can be constrained in the fit. Example plots showing the variations in comparison to the nominal distribution for the constrained matrix element systematic can be seen in Fig. 5.20, while the other SRs and constrained systematics can be found in App. B. Due to the high statistics for $t\bar{t}$, the statistical uncertainty is already small and constraints are likely.

In Fig. 5.21, the correlation matrices for the nuisance parameters with a correlation threshold of 0.2 are shown. The correlation describes the impact of one NP on another if varied. As expected, the NPs of the unfolding for the different bins are highly correlated and the selection of NPs above the threshold matches the selection in the ranking with the highest impact on the mean.

5. Sensitivity Study for the Observation of Spin Correlations

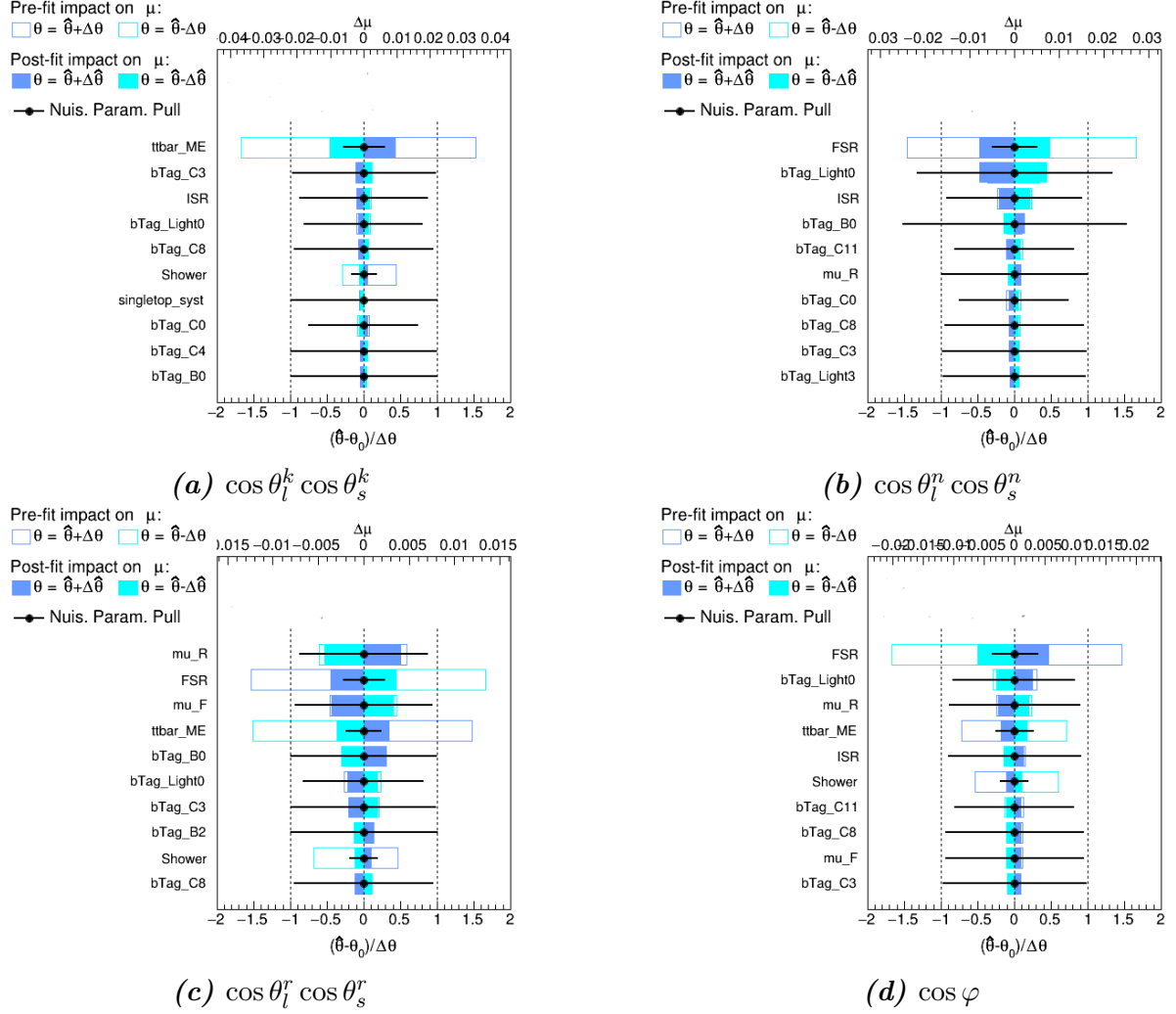


Figure 5.18.: Ranking for the systematics of the observables. The parton shower, matrix element and final state radiation systematic are among the systematics with the highest impact.

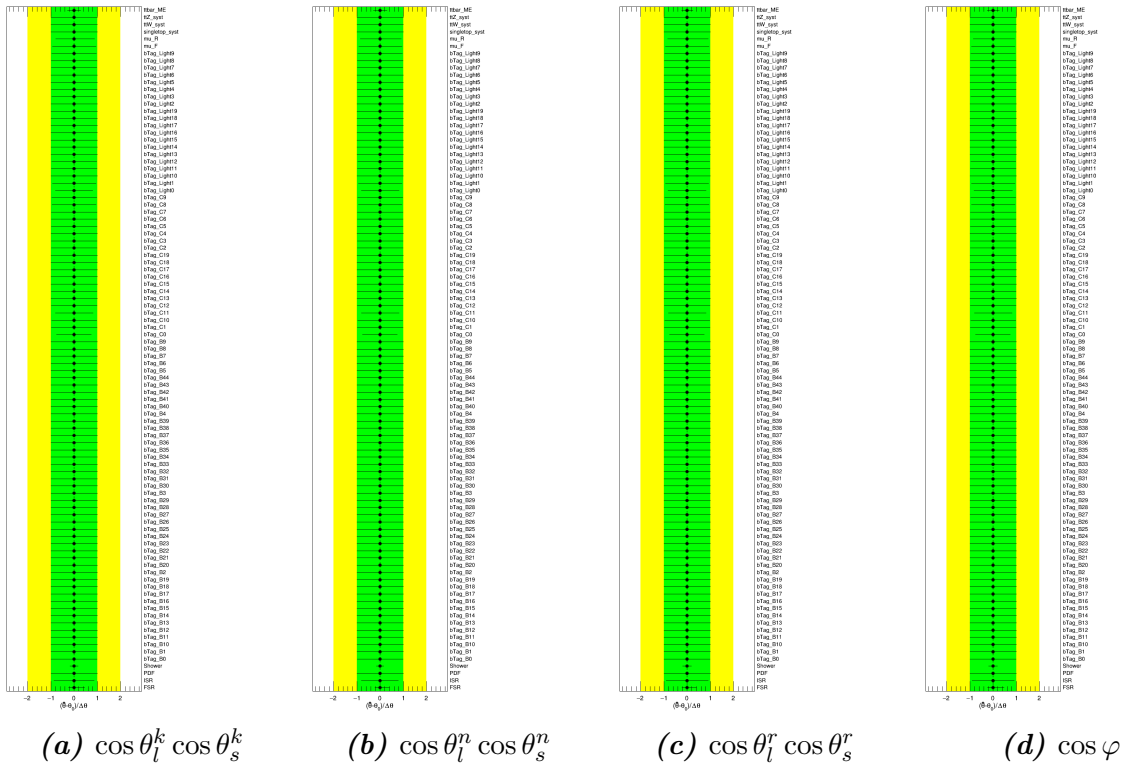


Figure 5.19.: Pull distribution for the systematics of the observables. The matrix element, parton shower and final state radiation systematics are shown to be constrained.

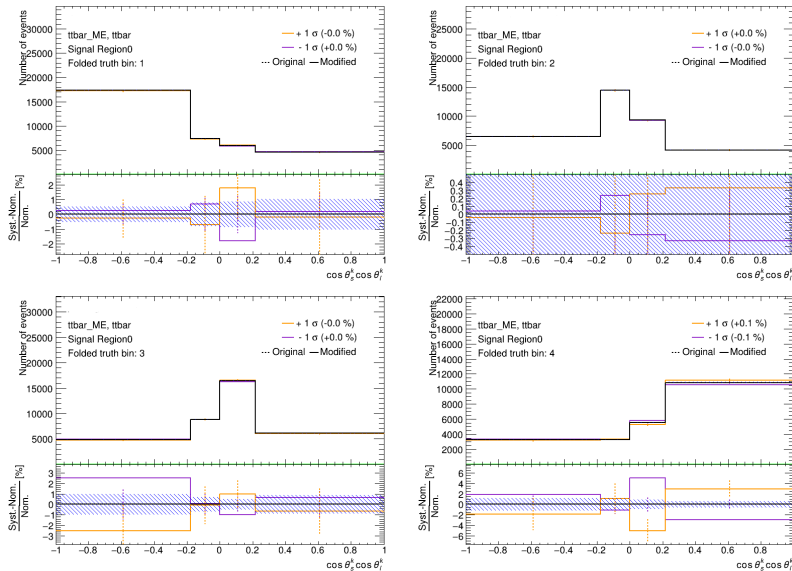


Figure 5.20.: Comparison between the nominal distribution and the variations for the matrix element systematic for SR 0 of $\cos \theta_l^k \cos \theta_s^k$. The other SRs and the other constrained systematics can be seen in App. B.

5. Sensitivity Study for the Observation of Spin Correlations

Unfolding Unfolded Truth Bin 2	100.0	78.7	88.9	-42.2	-30.3	26.2	40.2	24.4	59.7	-10.0	-10.0	50.9	-9.0	-2.3	2.2	1.4	-28.9	-13.1
Unfolding Unfolded Truth Bin 3	78.7	100.0	77.9	-21.8	-21.3	15.9	40.4	27.7	67.7	-4.9	-11.4	55.3	-5.9	-2.2	-2.2	-2.0	3.1	9.7
Unfolding Unfolded Truth Bin 4	88.9	77.9	100.0	-23.3	-8.0	20.3	40.8	24.6	61.9	-6.4	-9.9	58.2	-5.7	-2.2	11.2	11.8	-36.2	-31.8
FSR	42.2	-21.8	-23.3	100.0	25.3	-27.1	-11.8	9.3	-4.9	21.2	0.1	6.4	18.7	2.6	-5.8	-16.1	33.8	5.9
ISR	-30.3	-21.3	-8.0	25.3	100.0	43.4	5.0	2.5	-4.2	4.8	-0.3	-4.5	2.7	-3.3	-8.8	24.6	11.9	-10.3
Shower	26.2	15.9	20.3	-27.1	43.4	100.0	-18.0	-10.1	3.3	-3.4	12.2	24.2	-5.9	-5.1	21.9	37.4	-13.8	6.6
bTag_B0	40.2	40.4	40.8	-11.8	5.0	-18.0	100.0	1.5	-3.7	2.6	-4.6	-1.2	-3.5	-1.4	-2.7	-7.2	-7.7	-8.4
bTag_B1	24.4	27.7	24.6	-9.3	2.5	-10.1	1.5	100.0	2.9	-0.7	-3.9	-0.1	-2.4	0.2	-2.7	-4.7	-2.2	-0.5
bTag_C0	59.7	61.7	61.9	-4.9	-4.2	3.3	-2.7	2.9	100.0	-8.5	-33.4	36.8	14.0	8.9	3.5	1.6	-4.5	-3.0
bTag_C1	-10.0	-4.9	-6.4	21.2	4.8	-3.4	2.6	-0.7	-8.5	100.0	1.6	8.1	-14.9	12.7	-2.1	-4.7	9.7	0.3
bTag_C2	-10.0	-11.4	-9.9	0.1	-0.3	12.2	-4.8	3.9	-33.4	-1.8	100.0	11.0	7.8	3.4	-0.5	0.6	-1.7	-6.7
bTag_Light0	59.9	55.3	58.2	6.4	-4.5	24.2	-1.2	-1.1	-8.8	8.1	11.0	100.0	-27.3	-20.2	-1.8	0.7	-2.8	-11.5
bTag_Light1	-9.0	-5.9	-5.7	18.7	2.7	-5.9	-3.5	-2.4	14.0	-14.6	7.8	-27.3	100.0	2.6	-0.6	-0.2	5.0	4.1
bTag_Light2	-2.3	-2.2	-2.2	2.6	-0.3	-5.1	1.4	0.2	8.9	12.7	3.4	-20.2	-2.6	100.0	0.0	2.1	0.8	2.7
$\mu_{u,F}$	2.2	-2.2	11.2	-5.8	8.8	21.9	-2.7	-2.7	3.5	2.1	-0.5	-1.6	-0.6	0.0	100.0	17.6	-4.4	-4.2
$\mu_{u,R}$	1.4	-2.0	11.8	-16.1	24.6	37.4	7.2	4.7	0.6	0.7	-0.2	2.1	-17.8	100.0	-5.4	3.9	3.9	3.9
$\mu_{b,ME}$	-28.9	3.1	-36.2	33.8	11.9	-13.8	-7.7	-2.2	-4.5	9.7	-1.7	-2.8	5.0	0.8	-6.4	-5.4	100.0	53.8
mean	-13.1	9.7	-31.8	5.9	-10.3	6.6	-8.4	-0.5	3.0	0.3	-4.7	-11.5	4.1	2.7	4.2	3.9	53.8	100.0

(a) $\cos \theta_l^k \cos \theta_s^k$

Unfolding Unfolded Truth Bin 2	100.0	88.2	88.6	19.4	-30.6	20.2	64.7	68.1	20.9	80.0	-36.0	88.3	23.9	15.8	20.1	21.0	30.6	10.9	-28.7
Unfolding Unfolded Truth Bin 3	88.2	100.0	87.4	22.2	-32.0	23.6	65.8	67.6	20.5	80.8	-37.9	89.5	23.5	15.8	20.4	20.9	30.5	8.6	-32.9
Unfolding Unfolded Truth Bin 4	88.6	87.4	100.0	20.3	-31.8	19.9	65.5	65.7	19.6	88.9	-36.6	89.4	22.7	15.6	20.3	20.2	29.7	20.2	-35.6
FSR	19.4	22.2	20.3	100.0	20.3	2.3	-4.3	7.7	3.6	26.2	-15.6	33.4	24.9	6.8	13.5	5.4	-6.1	-6.2	60.3
ISR	-30.6	-32.0	-31.9	20.3	100.0	-3.7	34.4	-18.5	7.2	23.9	10.4	-21.5	-5.0	-4.1	-4.8	11.1	19.5	5.0	-12.0
Shower	20.2	20.6	19.9	2.3	-3.7	100.0	16.6	15.6	3.3	15.5	-7.3	16.6	4.3	3.8	4.2	2.2	3.2	2.4	-7.5
bTag_B0	64.7	65.8	65.5	-4.3	-54.4	16.6	100.0	32.3	10.1	52.8	-12.9	33.4	12.1	8.2	13.3	27.5	51.7	18.3	-14.6
bTag_B1	68.1	67.6	66.7	7.7	-18.5	18.6	32.3	100.0	9.7	44.9	-20.9	47.2	14.8	9.5	12.7	11.7	15.2	6.1	-8.7
bTag_B2	20.9	20.5	19.6	3.6	-7.2	3.3	10.1	9.7	100.0	14.7	-4.9	15.2	4.3	3.7	3.9	3.9	4.9	2.0	-0.0
bTag_C0	80.0	88.8	88.8	26.2	-23.9	15.5	52.8	44.9	14.7	100.0	-29.6	79.9	30.7	20.5	20.0	19.1	25.6	10.9	-31.8
bTag_C1	-36.0	-37.9	-36.6	15.6	10.4	-7.3	-19.9	-20.9	-4.9	-29.6	100.0	-28.8	-5.3	-7.8	-2.1	-4.3	-10.0	-1.8	2.3
bTag_Light0	88.3	88.5	88.4	33.4	-21.5	16.6	63.4	47.2	15.2	79.9	-20.8	100.0	9.9	5.1	16.4	17.5	26.3	10.1	-46.3
bTag_Light1	22.9	23.5	22.7	24.9	-5.0	-4.3	12.1	14.8	4.3	30.7	-5.3	9.8	100.0	1.3	-2.8	4.3	8.1	3.6	-14.2
bTag_Light2	15.8	15.8	15.6	6.8	-4.1	3.8	9.2	9.7	30.5	-7.8	5.1	1.3	100.0	5.9	3.5	7.9	3.2	-4.2	4.2
bTag_Light3	20.1	20.4	20.3	13.5	-4.8	4.2	13.3	12.7	3.9	20.0	-2.1	16.4	-2.2	5.9	800.0	4.3	5.4	2.5	-14.1
$\mu_{u,F}$	21.0	20.9	20.2	5.4	11.3	2.2	27.5	11.7	3.9	19.1	-8.5	17.5	4.3	3.5	4.3	100.0	-7.4	8.0	-13.1
$\mu_{u,R}$	30.6	30.5	29.7	-6.1	19.5	3.2	51.7	15.2	4.9	25.6	-12.0	28.3	8.1	7.9	5.4	-7.4	100.0	26.1	-2.4
$\mu_{b,ME}$	10.9	6.6	20.2	-6.2	5.0	2.4	18.3	6.1	2.0	10.9	-1.8	10.1	3.6	3.2	2.5	8.0	28.1	100.0	-4.6
mean	-28.7	-32.9	-33.5	60.3	-12.0	-7.5	-14.6	-8.7	-0.0	-31.8	2.3	-46.3	-14.2	-14.1	-13.1	2.4	-4.6	100.0	100.0

(b) $\cos \theta_l^n \cos \theta_s^n$

Unfolding Unfolded Truth Bin 2	100.0	78.5	89.3	-9.2	-7.5	14.6	33.9	54.9	38.1	-11.3	48.7	-9.8	9.6	10.2	-3.3	8.2			
Unfolding Unfolded Truth Bin 3	78.5	100.0	85.4	2.9	28.2	30.0	28.1	54.8	37.6	9.6	54.2	-7.0	6.2	5.3	-4.9	5.2			
Unfolding Unfolded Truth Bin 4	89.3	85.4	100.0	-6.9	25.2	15.4	34.6	55.9	38.5	-11.2	49.4	-8.6	7.4	-10.4	-9.5	-12.4			
FSR	-9.2	2.9	-6.9	100.0	9.3	-14.4	-6.6	6.2	-9.3	2.5	27.2	15.8	-12.1	-17.3	24.5	-18.5			
ISR	-7.5	-28.2	-25.2	9.3	100.0	-64.6	3.9	-5.2	5.3	0.8	-5.6	-1.2	8.6	22.5	4.0	-3.4			
Shower	14.6	30.0	15.4	-14.4	64.6	100.0	-19.5	-1.1	5.9	10.1	23.9	-6.4	23.5	39.5	-17.1	4.5			
bTag_B0	33.9	28.1	34.6	-6.6	3.9	-19.5	100.0	-14.5	-7.3	-2.9	-11.1	-2.4	-4.4	-9.9	-0.7	14.0			
bTag_B1	54.9	54.8	55.9	6.2	-5.2	-1.1	-14.5	100.0	-15.4	-25.4	28.2	13.4	2.9	-1.0	2.2	0.2			
bTag_C0	-38.1	-37.6	-38.5	-9.3	5.3	5.9	-7.3	-15.4	100.0	-0.5	-10.7	4.9	-1.1	-1.7	-1.1	-7.5			
bTag_C1	-11.3	-9.6	-11.2	2.5	0.8	10.1	-2.9	-32.4	-0.5	100.0	13.2	8.0	0.6	-1.8	-0.5	-5.3			
bTag_Light0	48.7	54.2	49.4	27.2	-5.6	23.9	-11.1	28.2	-10.7	13.2	100.0	-30.3	-0.4	-1.9	4.0	-11.8			
bTag_Light1	-9.8	-7.0	-8.6	15.8	-1.2	-4.4	-2.4	13.4	4.9	8.0	-30.3	100.0	-3.7	-3.1	-4.2	-0.4			
$\mu_{u,F}$	9.6	6.2	7.4	-12.1	8.6	23.5	-4.4	2.9	-1.1	0.6	-0.4	-3.7	100.0	-12.1	-16.1	-19.6			
$\mu_{u,R}$	10.2	5.3	-10.4	-17.3	22.5	39.5	-9.9	-1.0	-1.7	-1.8	-1.9	-3.1	-12.1	100.0	-14.0	23.8			
$\mu_{b,ME}$	-3.3	-4.9	-9.5	24.5	4.0	-17.1	-0.7	2.2	-1.1	-0.5	4.0	4.2	-16.1	-14.0	100.0	16.3			
mean	8.2	5.2	-12.4	-18.5	-3.4	4.5	14.0	0.2	-7.5	-5.3	-11.8	-0.4	-19.6	23.8	16.3	100.0			

(c) $\cos \theta_l^r \cos \theta_s^r$

Unfolding Unfolded Truth Bin 2	100.0	96.2	-3.1	-32.9	37.9	45.4	22.8	61.6	-29.0	-7.4	60.4	1.6	9.1	1.8	-9.6				
Unfolding Unfolded Truth Bin 3	96.2	100.0	-10.1	-30.1	34.9	46.9	23.2	62.5	-30.9	-9.1	55.8	1.0	10.5	-1.9	-22.1				
Unfolding Unfolded Truth Bin 4	-3.1	-10.1	100.0	12.2	-5.5	-3.2	-5.1	6.6	-7.4	4.0	25.1	25.0	-8.1	4.0	55.4				
FSR	-32.9	-30.1	12.2	100.0	-63.1	-6.3	1.1	-10.3	5.3	0.7	-9.3	-2.0	19.8	0.3	19.5				
ISR	37.9	34.9	-5.5	-63.1	100.0	-6.4	-5.9	10.1	4.5	10.6	34.1	1.2	44.2	-10.3	-15.3				
Shower	45.4	46.9	-3.2	-6.3	-6.4	100.0	-1.3	-3.1	-8.4	-1.7	3.5	1.6	-9.2	-2.2	-8.5				
bTag_B0	22.8	23.2	-5.1	1.1	-5.9	-1.3	100.0	2.4	3.1	-2.3	1.5	-0.3	-6.7	1.5	2.7				
bTag_B1	61.6	62.5	6.6	-10.3	10.1	-3.1	2.4	100.0	-11.8	-32.1	34.5	18.3	3.9	4.5	-5.1				
bTag_C0	-29.0	-30.9	-7.4	5.3	4.5	-8.4	3.1	-11.8	100.0	2.9	-7.5	4.2	-2.6	3.4	13.5				
bTag_C1	-7.4	-9.1	4.0	0.7	10.6	-1.7	-2.9	-32.1	-2.9	100.0	13.6	8.2	0.8	-3.7	11.3				
bTag_Light0	60.4	55.8	25.1	-9.3	34.1	3.5	1.5	34.5	-7.5	13.6	100.0	-19.4	8.0	-0.3	25.5				
bTag_Light1	1.6	1.0	25.0	-2.0	1.2	1.6	0.3	16.3	4.2	8.2	-19.4	100.0	0.9	1.2	7.0				
$\mu_{u,F}$	9.1	10.5	-8.1	19.8	44.2	-9.2	-6.7	3.9	-2.6	0.8	8.0	0.9	100.0	-7.9	24.0				
$\mu_{u,R}$	1.8	-1.9	4.0	0.3	-10.3	-2.2	1.5	4.5	3.4	-3.7	-0.3	1.2	-7.9	100.0	-21.3				
$\mu_{b,ME}$	-9.6	-22.1	55.4	19.5	-15.3	-8.5	2.7	-5.1	13.5	11.3	25.5	7.0	-24.0	21.3	100.0				
mean	9.6	5.2	-12.4	-18.5	-3.4	4.5	14.0	0.2	-7.5	-5.3	-11.8	-0.4	-19.6	23.8	16.3	100.0			

(d) $\cos \varphi$

Figure 5.21.: Correlation matrices for the normalisation factors of the observables. Only correlations above a threshold of 0.2 are shown.

6. Conclusion

In this thesis, the spin correlations of $t\bar{t}$ in the lepton+jets channel were investigated with focus on the sensitivity achieved.

Methodically, a c -tagging approach in combination with event reconstruction was used to determine the strange quark as a spin analyser. Based on that, spin sensitive observables were constructed and the reconstructed distributions for these observables unfolded to parton level. The unfolding was necessary because of difficulties in the reconstruction on the one hand and the analytical formulas being defined only on parton level on the other hand. In the unfolding process, the spin coefficients were extracted, and the uncertainties studied representing the result of this thesis.

The results for the c -tagging approach shown in Fig. 5.2 indicate that the c -tagging based on the b -tagging WPs was successful. In contrast, the identification of the strange quark necessary for the spin sensitivity was less successful, as displayed in Fig. 5.3, due to mismatches in the event reconstruction. Because of the performance of unfolding, this problem was hardly of consequence but it could be investigated further by removing badly reconstructed events.

The values for the spin coefficients extracted via unfolding and shown in Tab. 5.8 demonstrate the sensitivity achieved. As presented in Tab. 6.1, the results are several σ intervals away from 0 which would mean no spin correlations. For most of the coefficients, a very high sensitivity with $\geq 15\sigma$ intervals was achieved. The $C(r, r)$ coefficient is an exception because the effect is already small (literature value of 0.071, implemented value of 0.05) which can also be seen in Fig. 5.17.

The sensitivity was limited by the systematic uncertainties implemented and since only the most relevant systematics were included, the analysis could profit from an on-going investigation of the complete set of systematics. Moreover, the simulations of Run 2 in 2018 could be extended by considering simulations for the years 2015, 2016 and 2017.

6. Conclusion

parameter	σ intervals to 0
$C(k, k)$	15
$C(r, r)$	3
$C(n, n)$	31
D	20

Table 6.1.: Distance of the parameter values to 0, expressed in σ intervals.

The D spin coefficient is not only sensitive to spin correlations but also to quantum entanglement between the top quarks, which was also investigated. The result shown in Eq. 5.3 indicates quantum entanglement with a significance of 1σ . This quantum entanglement is a path to further investigation in $t\bar{t}$.

In conclusion, a high sensitivity to spin correlations in the $t\bar{t} \rightarrow \text{lepton} + \text{jets}$ channel based on c -tagging and unfolding was achieved in this thesis. As a long-term aim, the reconstruction and unfolding procedure can be applied to data to investigate the $t\bar{t}$ spin correlations with the sensitivity obtained.

A. Additional Plots for the Investigation of Spin Observables

A.1. Migration Matrix

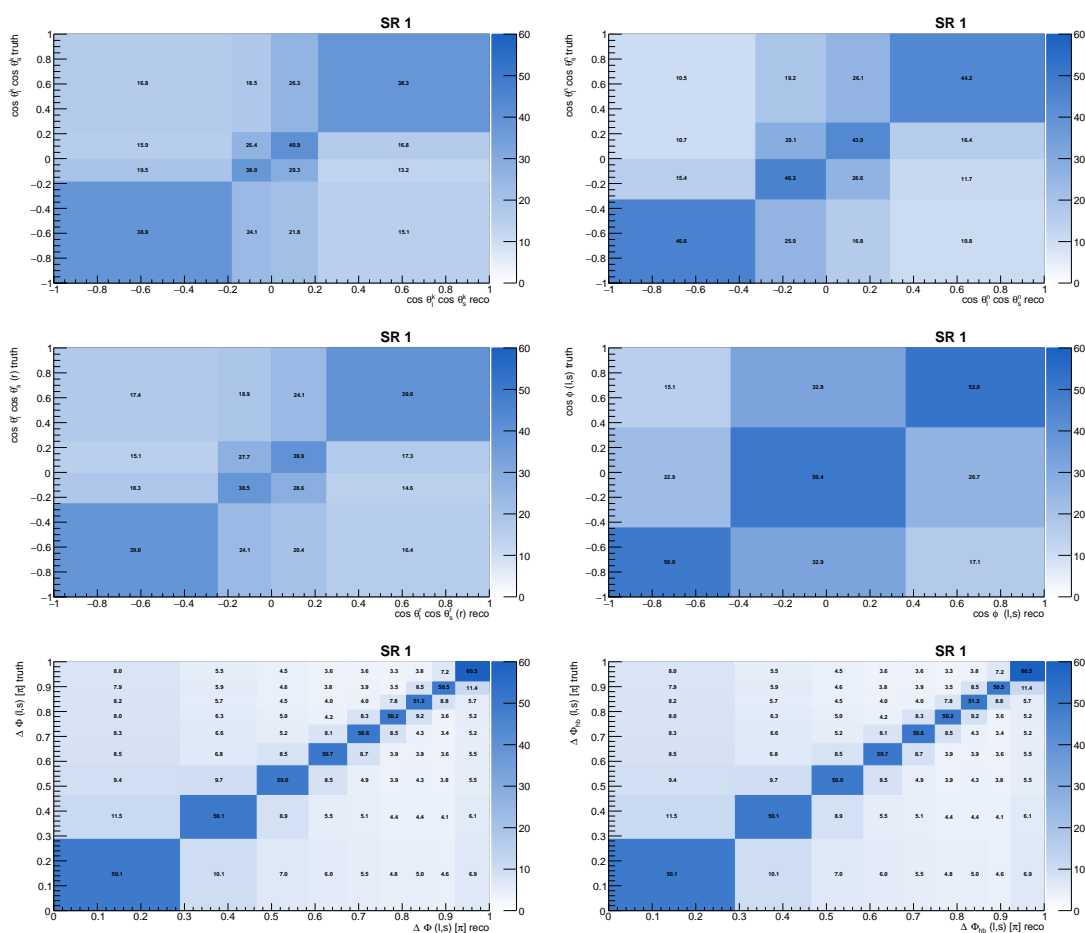


Figure A.1.: Migration matrix for the observables in SR 1.

A. Additional Plots for the Investigation of Spin Observables

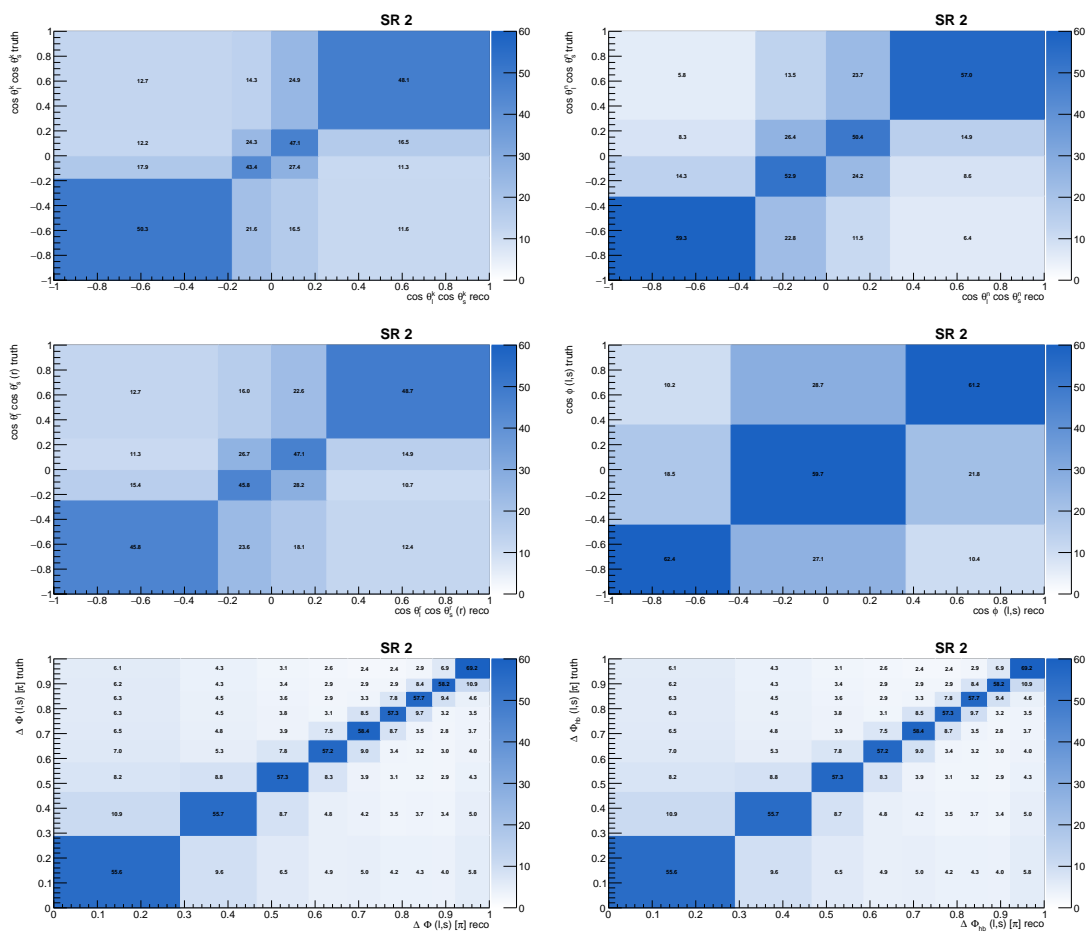


Figure A.2.: Migration matrix for the observables in SR 2.

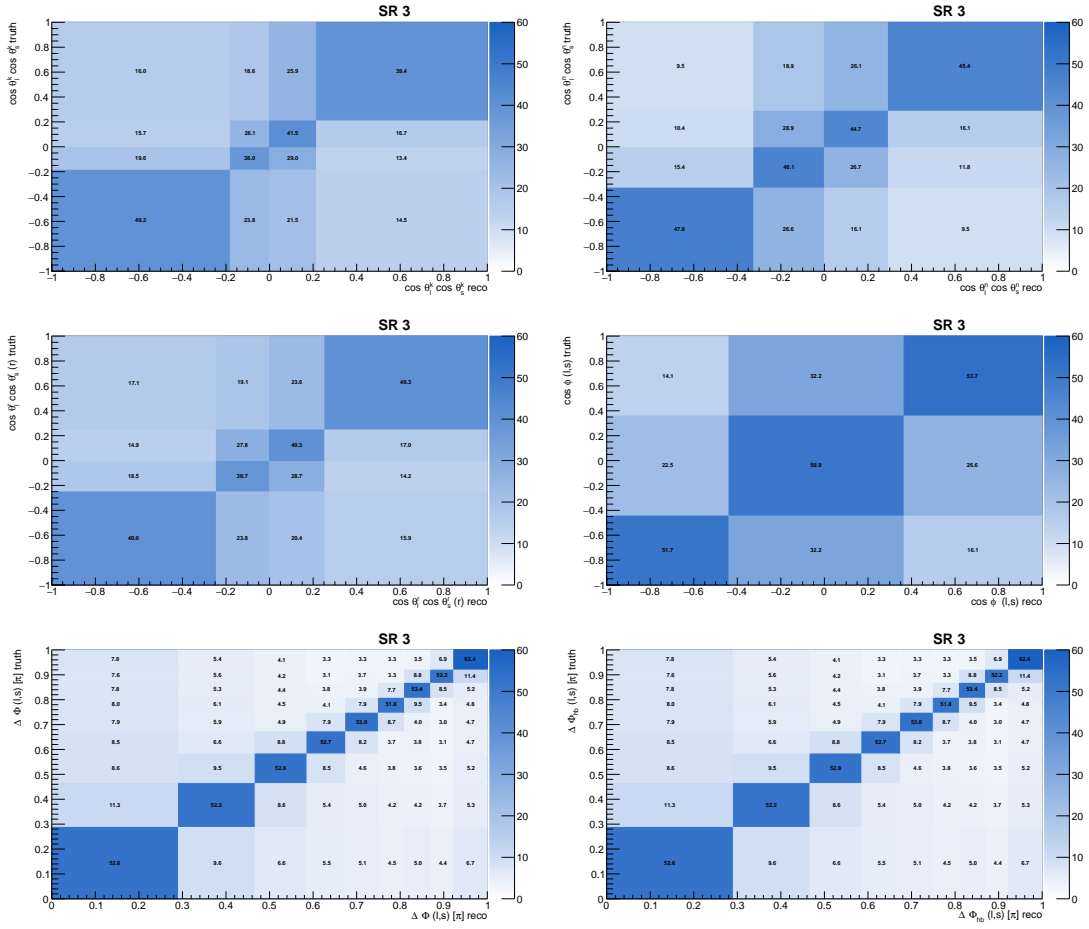


Figure A.3.: Migration matrix for the observables in SR 3.

A. Additional Plots for the Investigation of Spin Observables

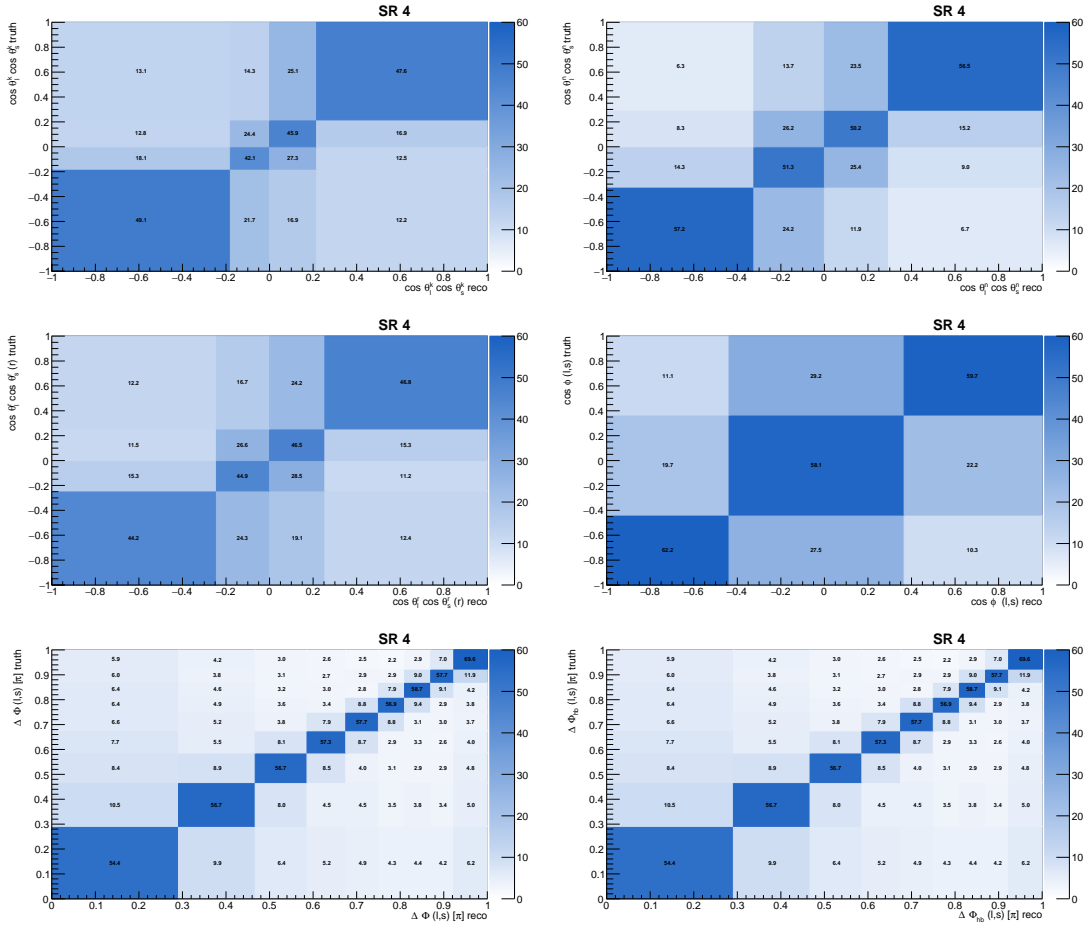


Figure A.4.: Migration matrix for the observables in SR 4.

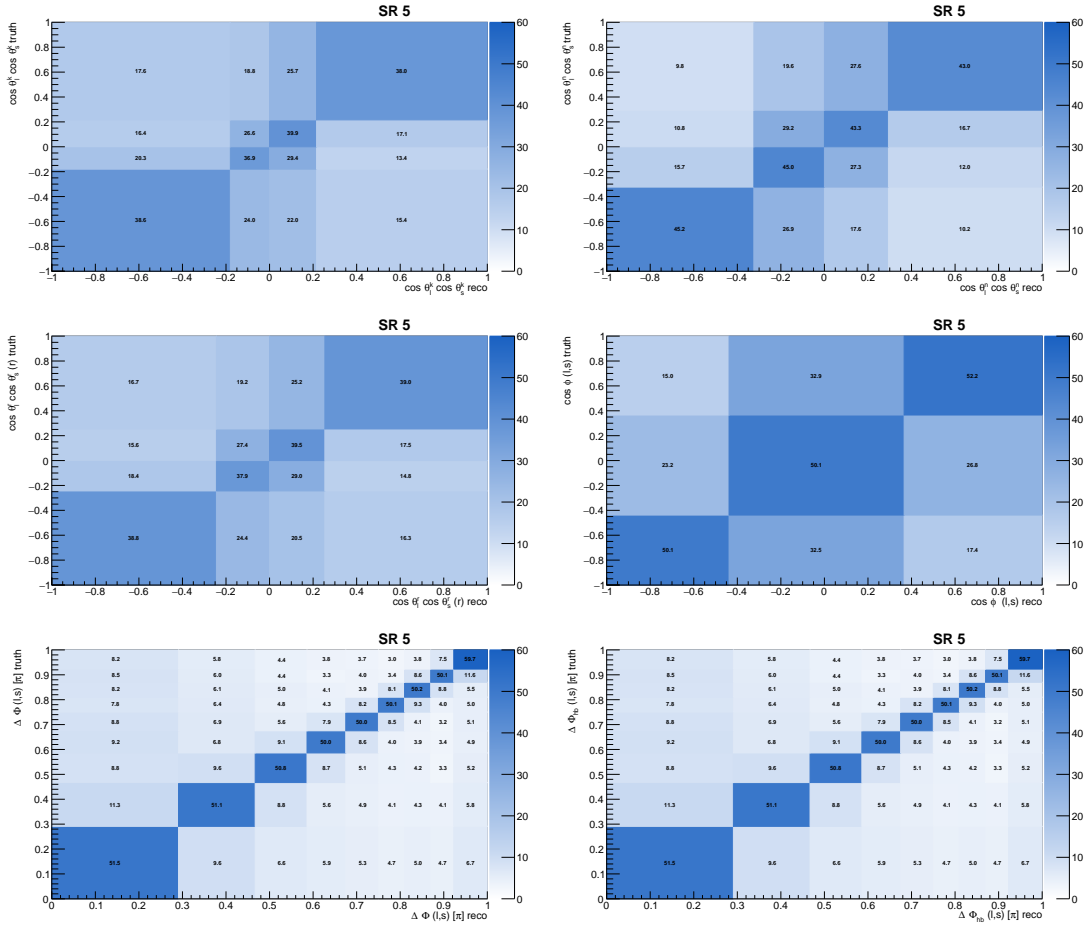


Figure A.5.: Migration matrix for the observables in SR 5.

A.2. Comparison Truth and Reconstructed Distribution

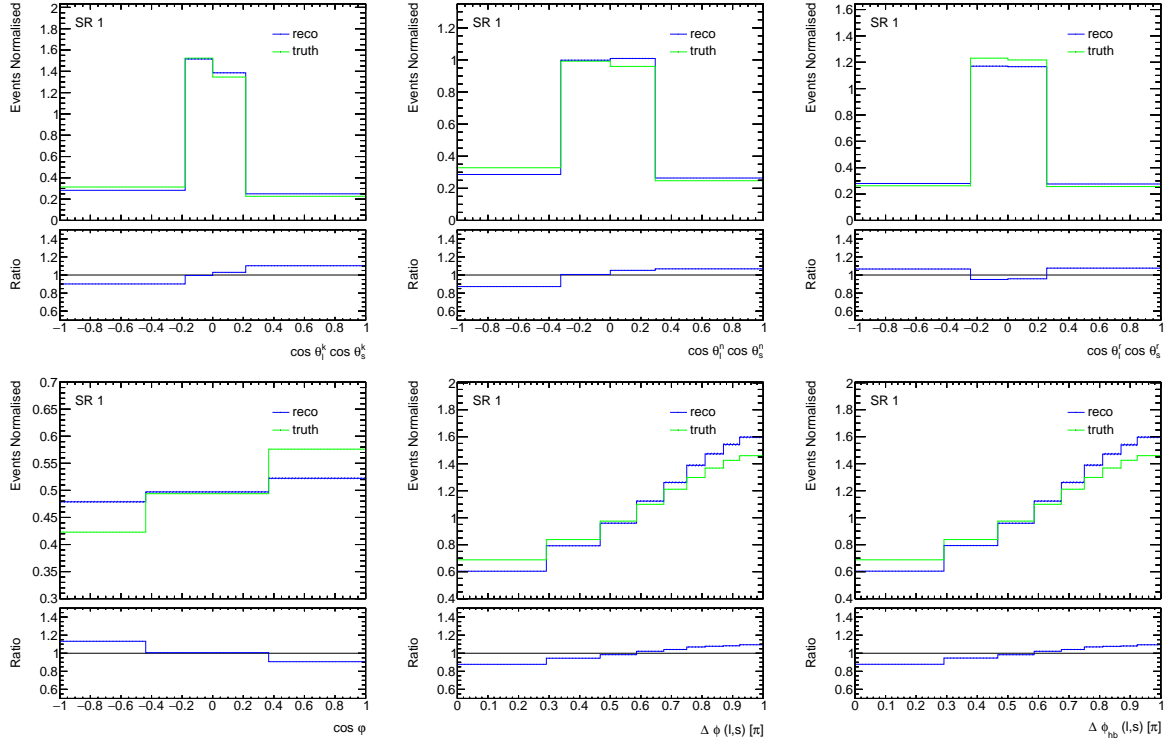


Figure A.6.: Comparison between truth distribution and reconstructed distribution in SR 1.

A.2. Comparison Truth and Reconstructed Distribution

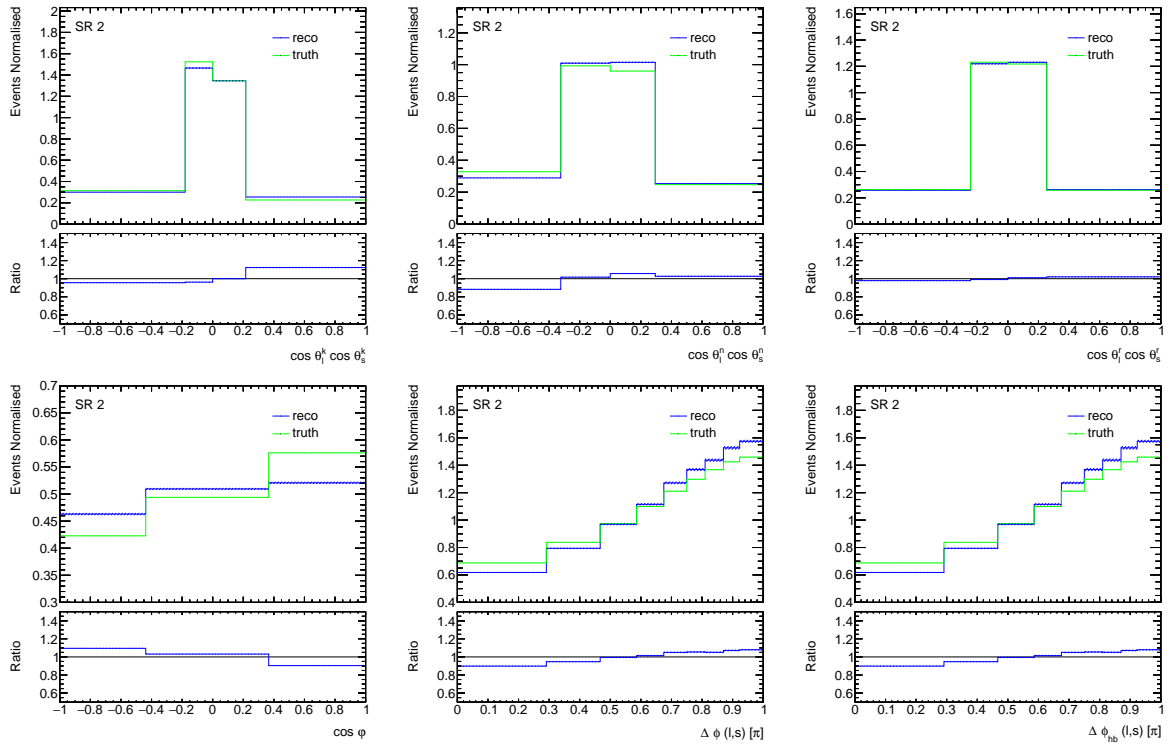


Figure A.7.: Comparison between truth distribution and reconstructed distribution in SR 2.

A. Additional Plots for the Investigation of Spin Observables

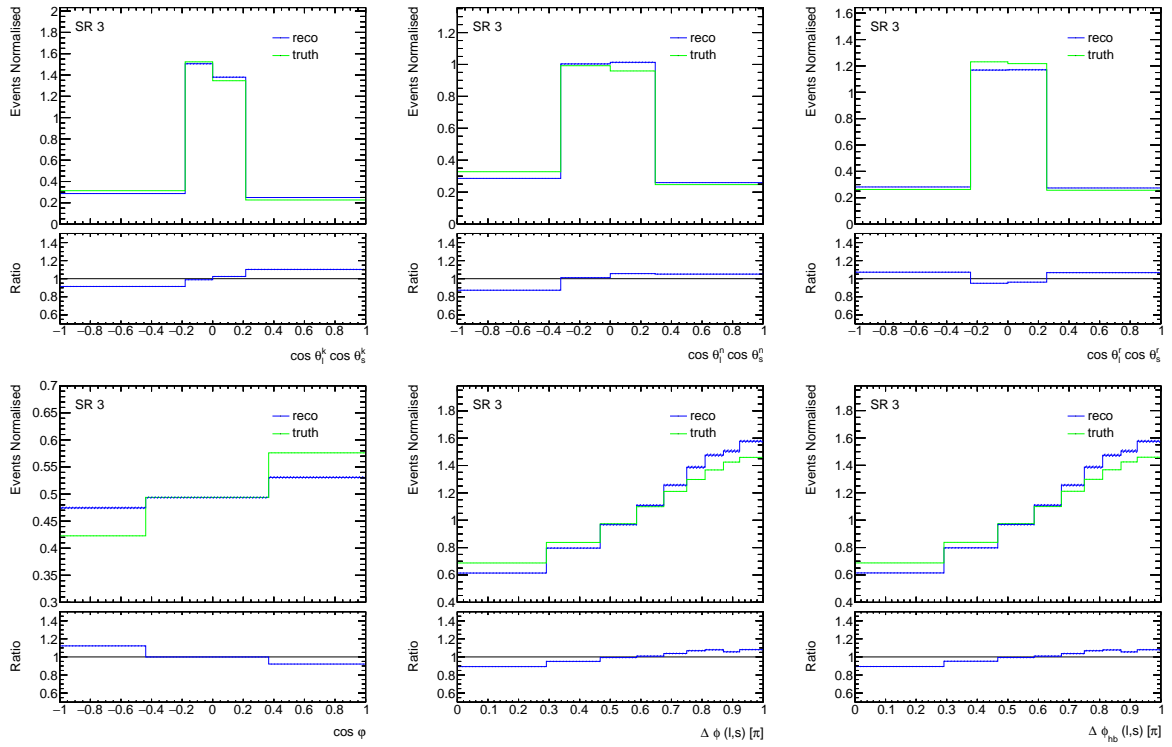


Figure A.8.: Comparison between truth distribution and reconstructed distribution in SR 3.

A.2. Comparison Truth and Reconstructed Distribution

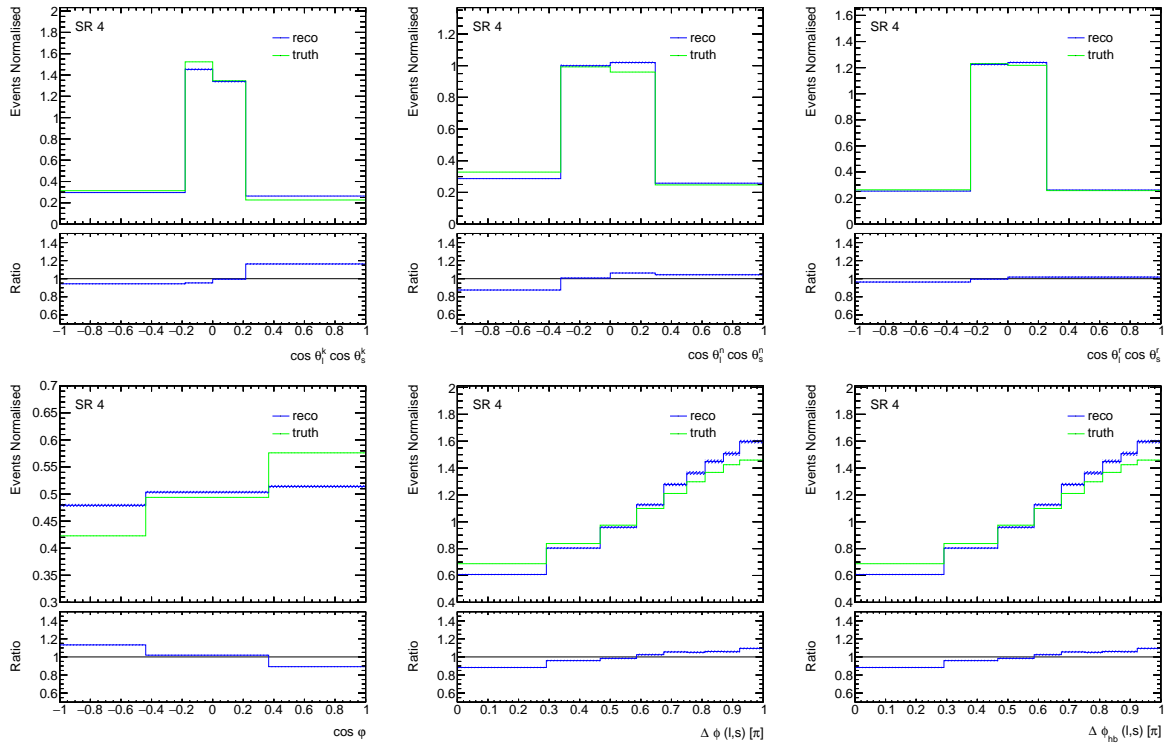


Figure A.9.: Comparison between truth distribution and reconstructed distribution in SR 4.

A. Additional Plots for the Investigation of Spin Observables

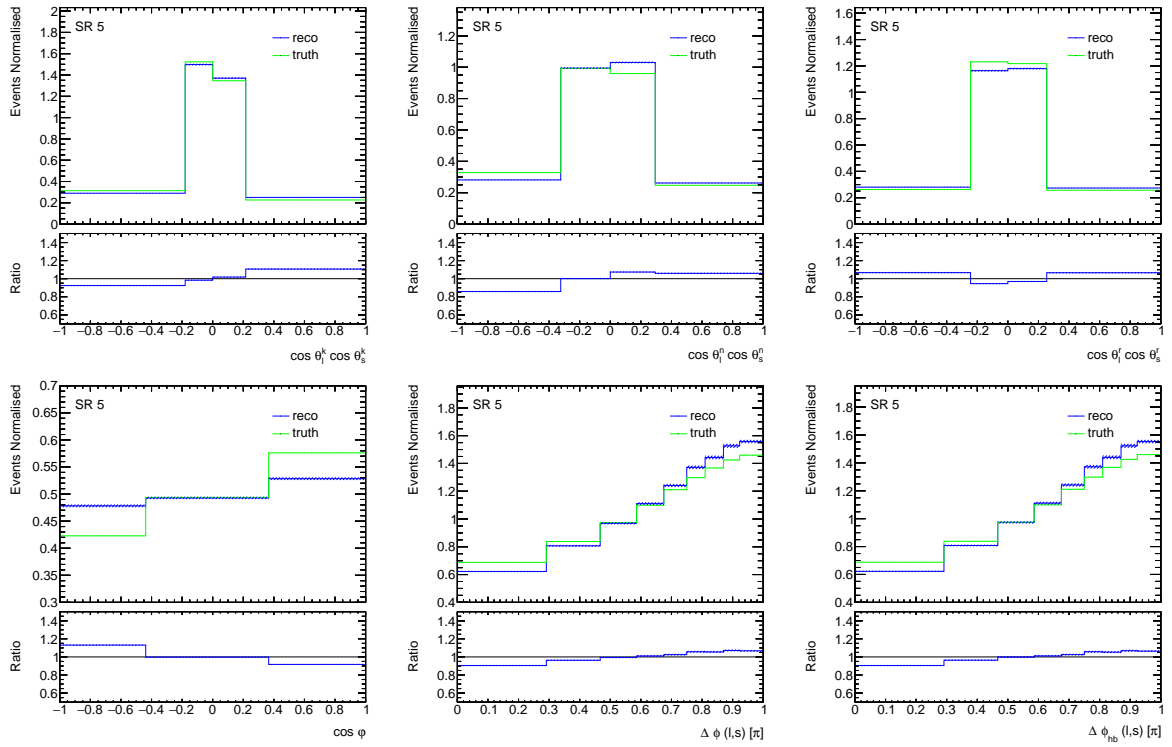


Figure A.10.: Comparison between truth distribution and reconstructed distribution in SR 5.

A.3. Selection Efficiencies

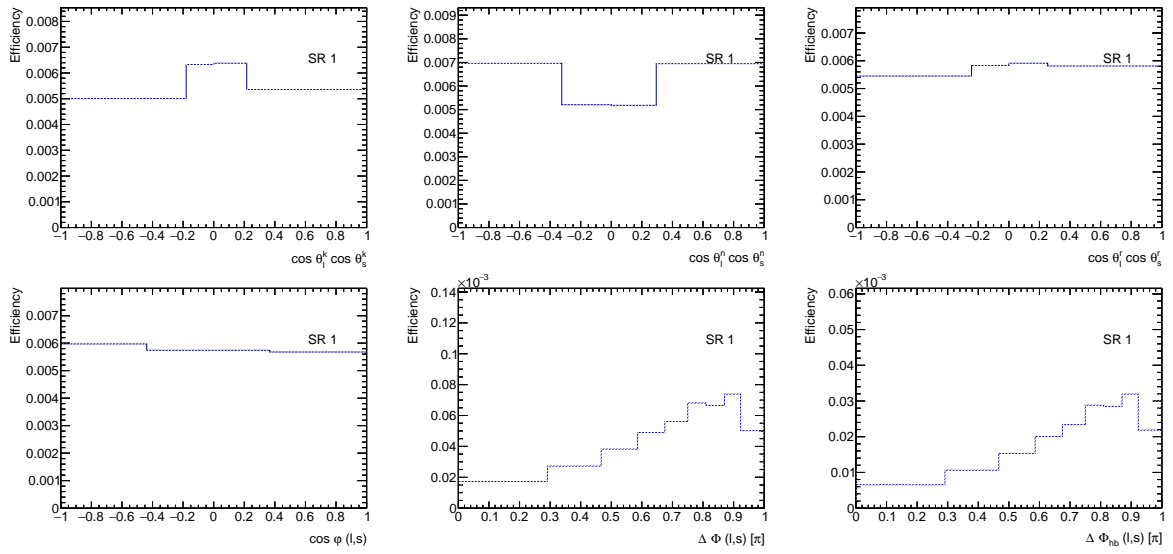


Figure A.11.: Selection efficiencies for the observables in SR 1.

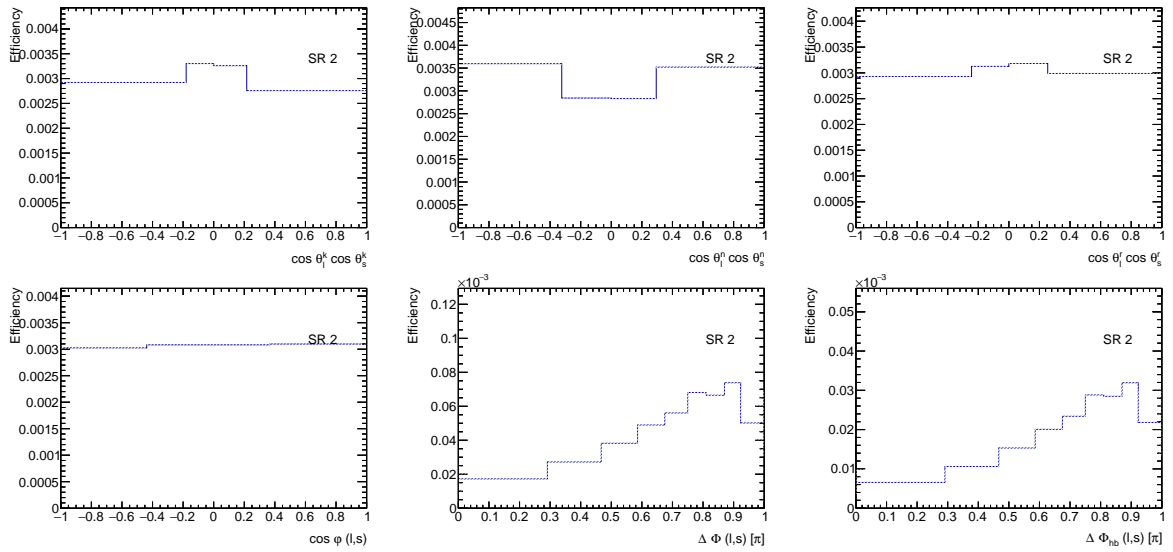


Figure A.12.: Selection efficiencies for the observables in SR 2.

A. Additional Plots for the Investigation of Spin Observables

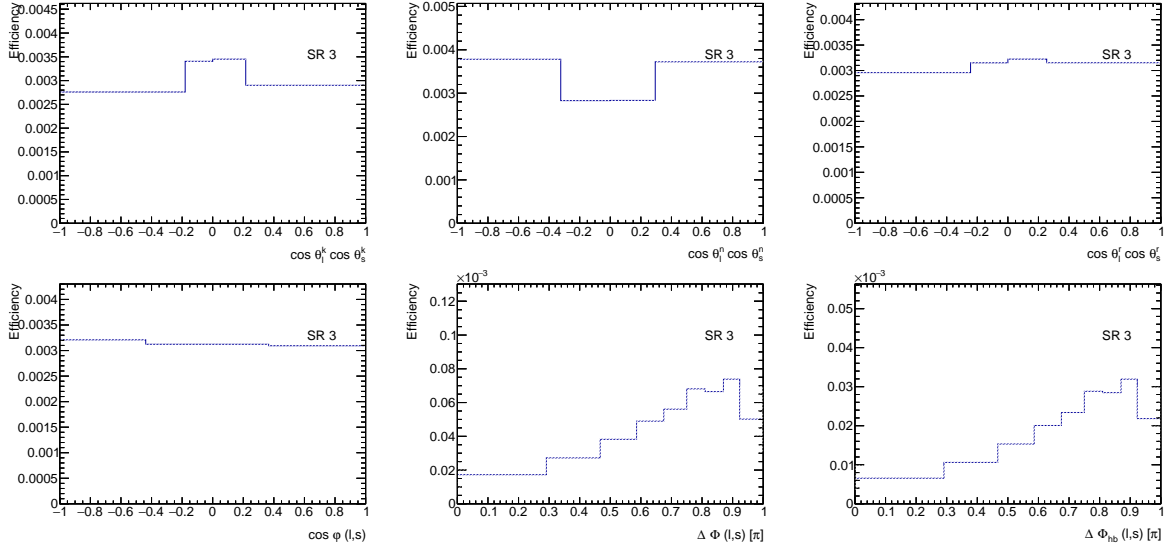


Figure A.13.: Selection efficiencies for the observables in SR 3.

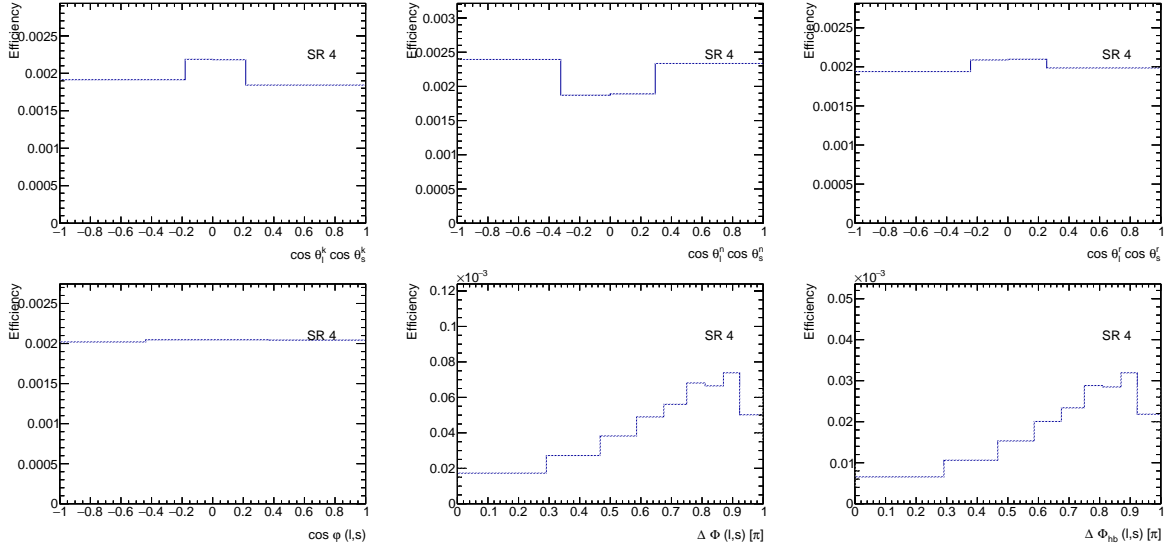


Figure A.14.: Selection efficiencies for the observables in SR 4.

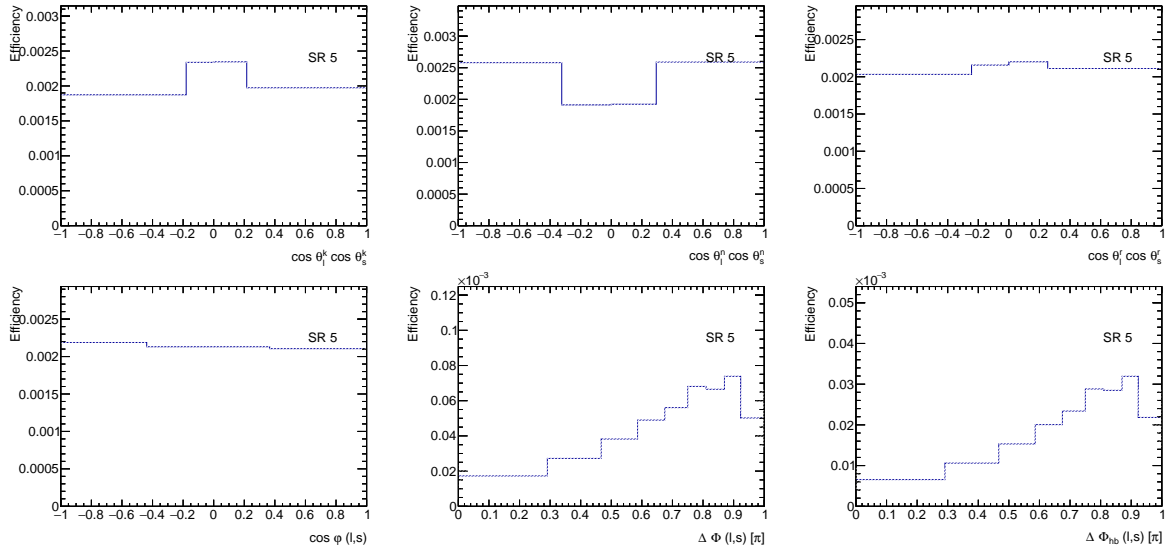


Figure A.15.: Selection efficiencies for the observables in SR 5.

A.4. Acceptance

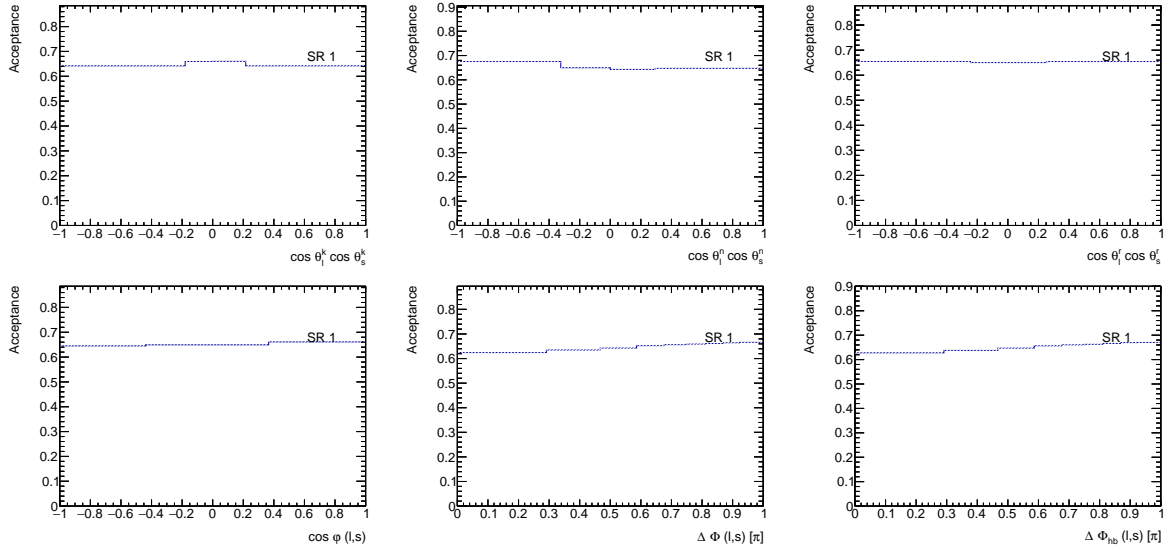


Figure A.16.: Acceptance for the observables in SR 1.

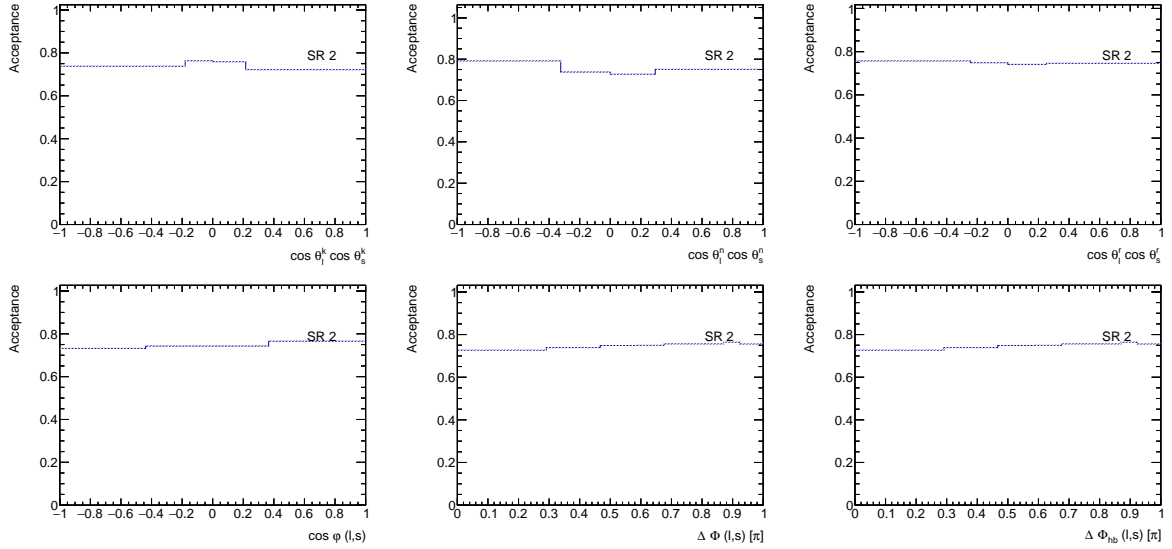


Figure A.17.: Acceptance for the observables in SR 2.

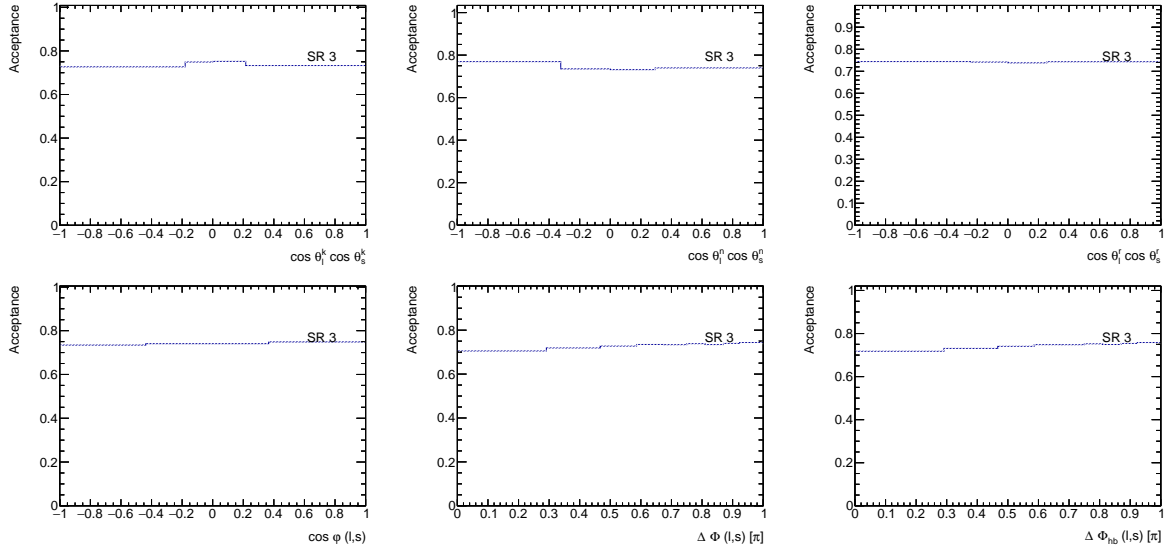


Figure A.18.: Acceptance for the observables in SR 3.

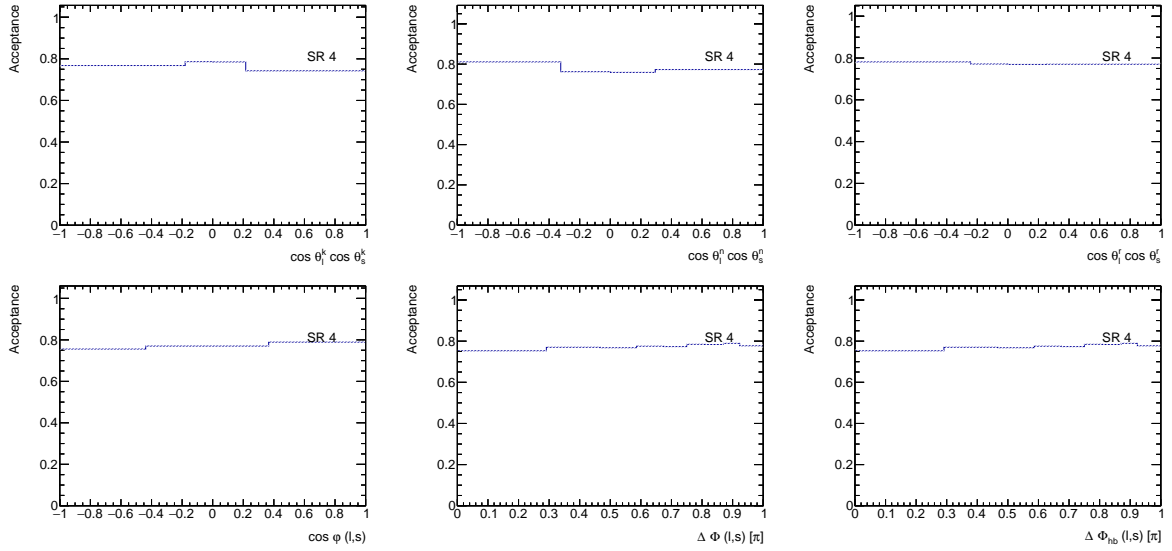


Figure A.19.: Acceptance for the observables in SR 4.

A. Additional Plots for the Investigation of Spin Observables

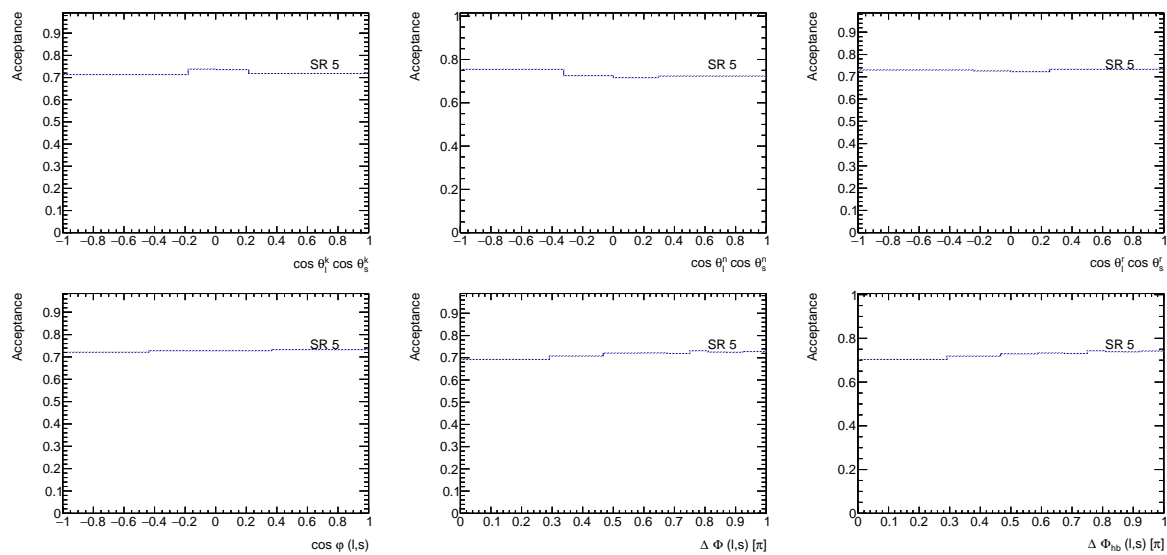


Figure A.20.: Acceptance for the observables in SR 5.

A.5. Comparison Pre- and Post-Fit Plots

A. Additional Plots for the Investigation of Spin Observables

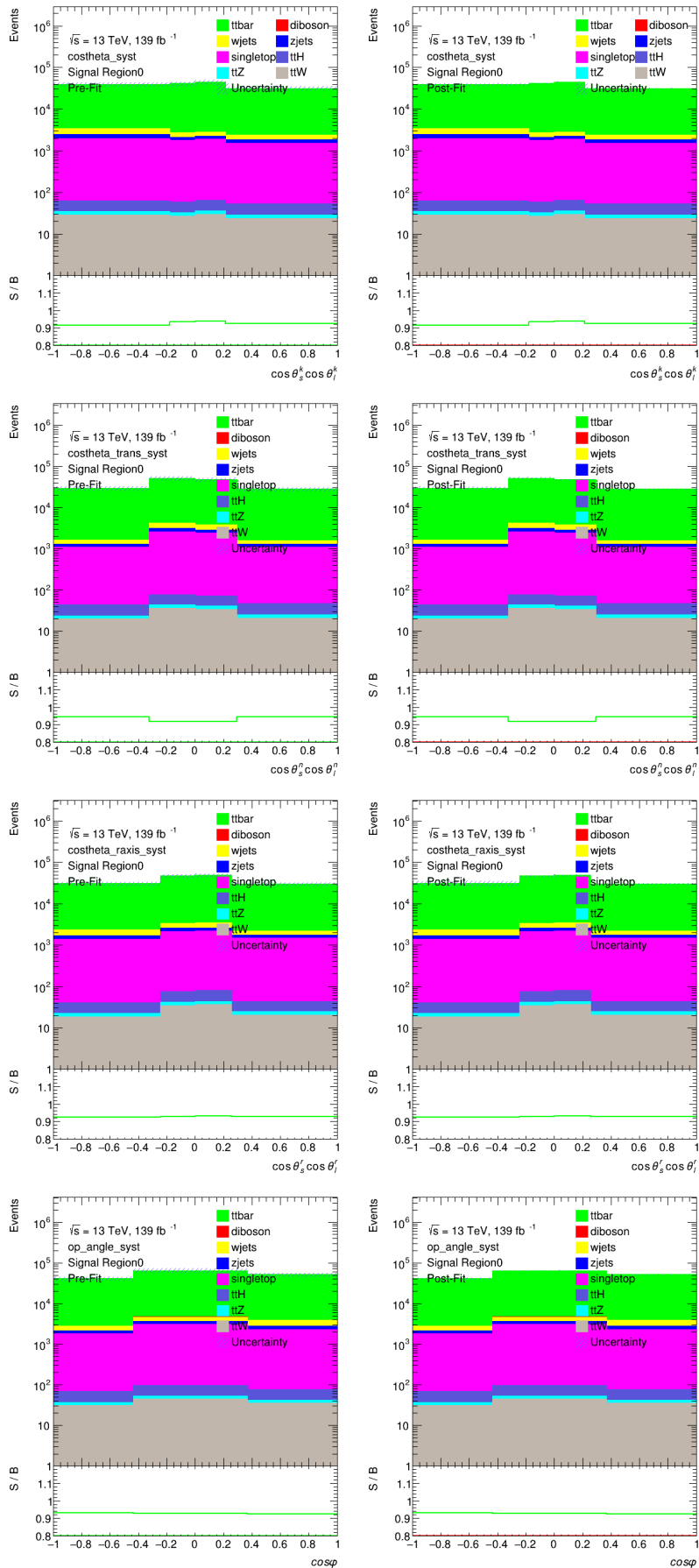


Figure A.21.: Comparison between the pre-fit and post-fit plots for the observables for SR 0.

A.5. Comparison Pre- and Post-Fit Plots

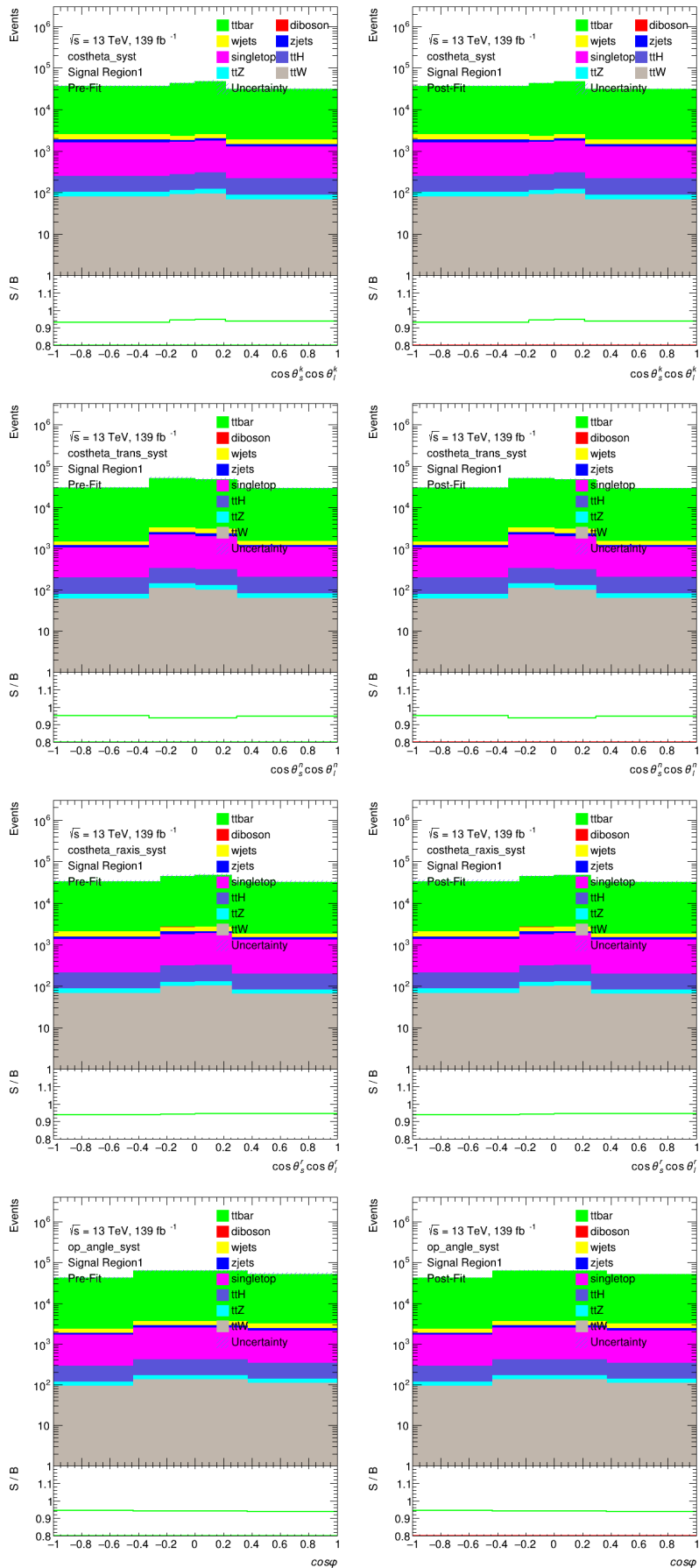


Figure A.22.: Comparison between the pre-fit and post-fit plots for the observables for SR 1.

A. Additional Plots for the Investigation of Spin Observables

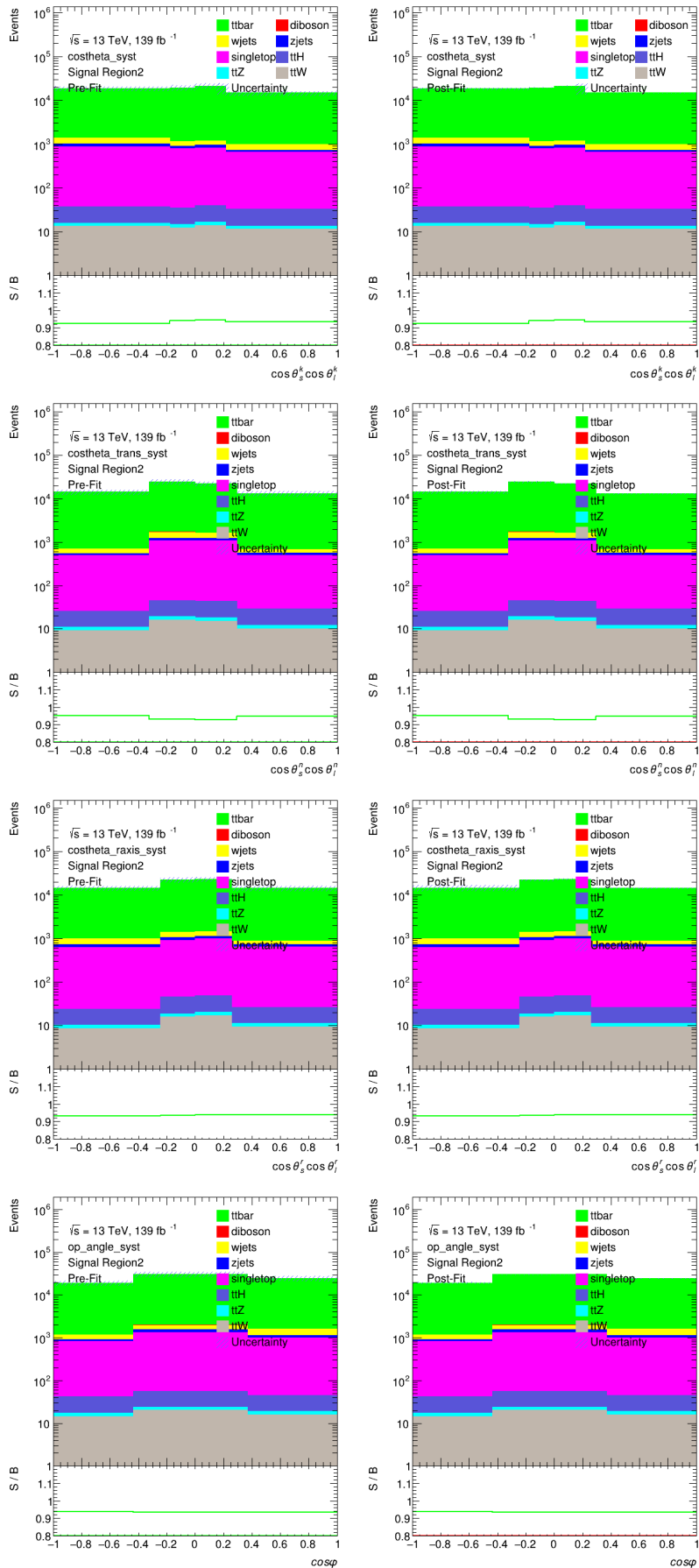


Figure A.23.: Comparison between the pre-fit and post-fit plots for the observables for SR 2.

A.5. Comparison Pre- and Post-Fit Plots

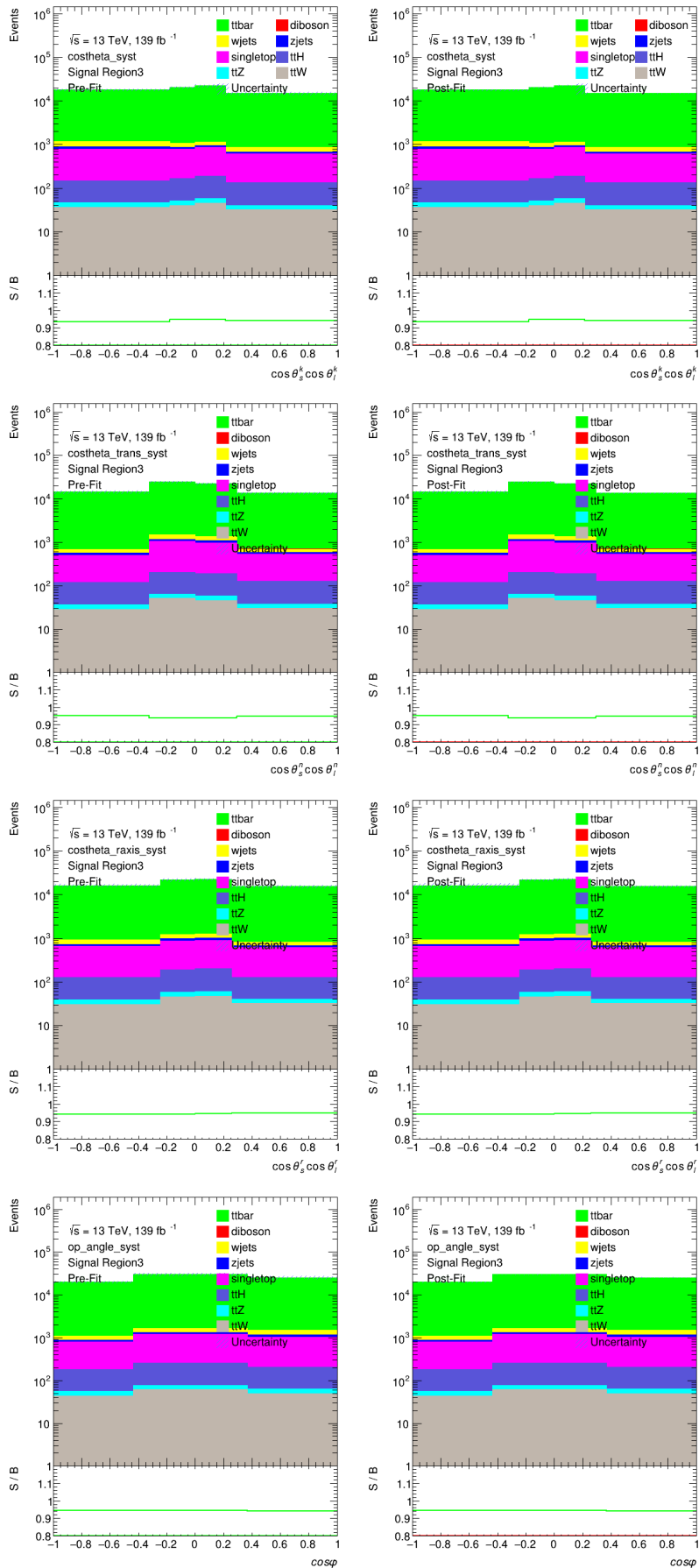


Figure A.24.: Comparison between the pre-fit and post-fit plots for the observables for SR 3. 69

A. Additional Plots for the Investigation of Spin Observables

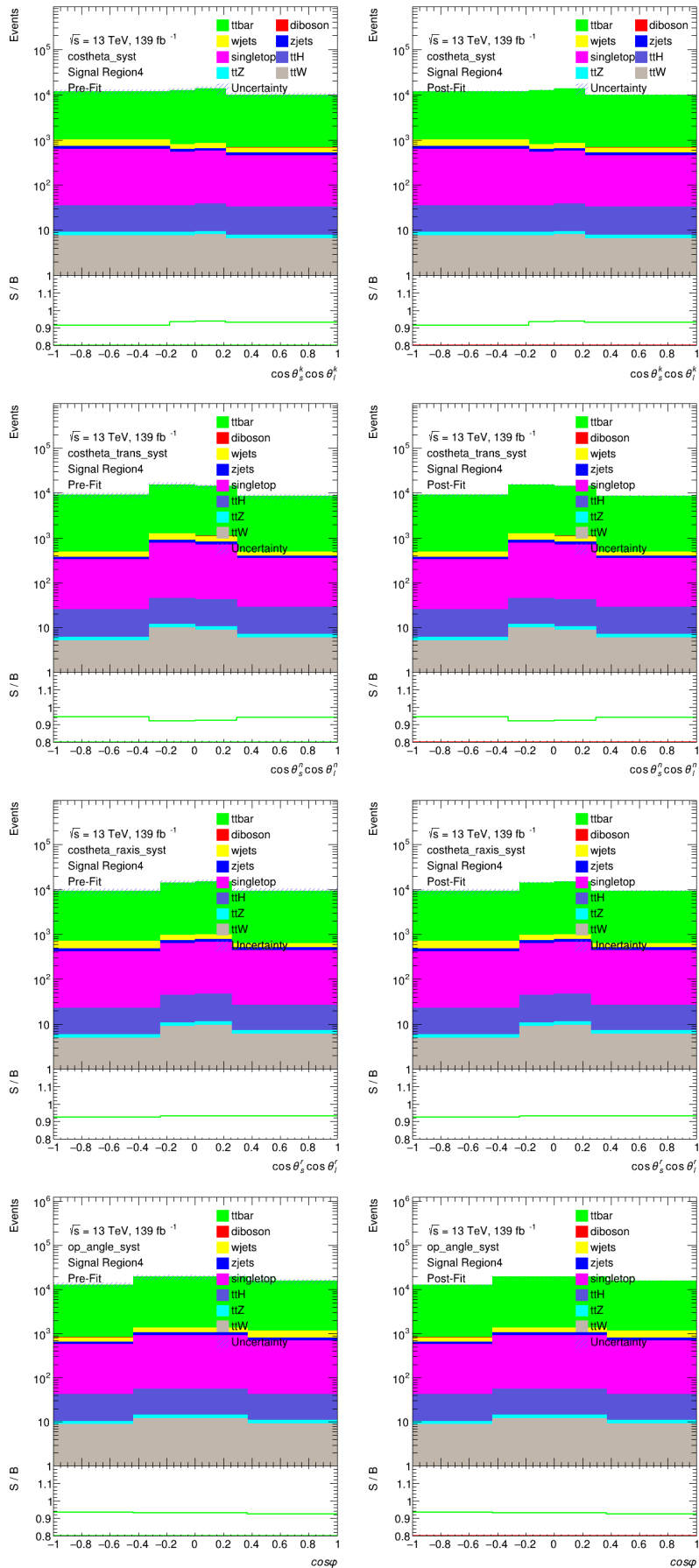


Figure A.25.: Comparison between the pre-fit and post-fit plots for the observables for SR 4.

A.5. Comparison Pre- and Post-Fit Plots

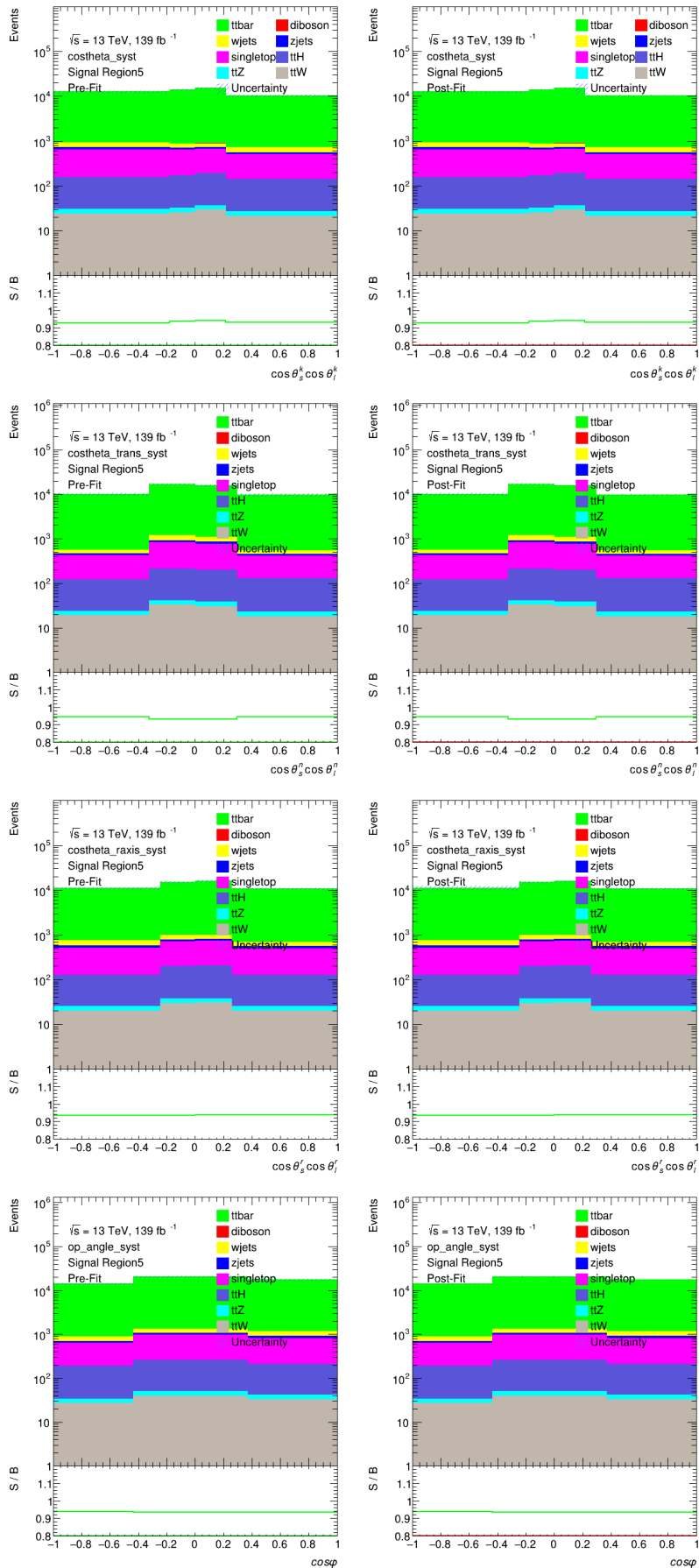


Figure A.26.: Comparison between the pre-fit and post-fit plots for the observables for SR 5.

B. Additional Plots for the Systematics

B. Additional Plots for the Systematics

B.1. $\cos \theta_l^k \cos \theta_s^k$

B.1.1. $t\bar{t}$ Matrix Element

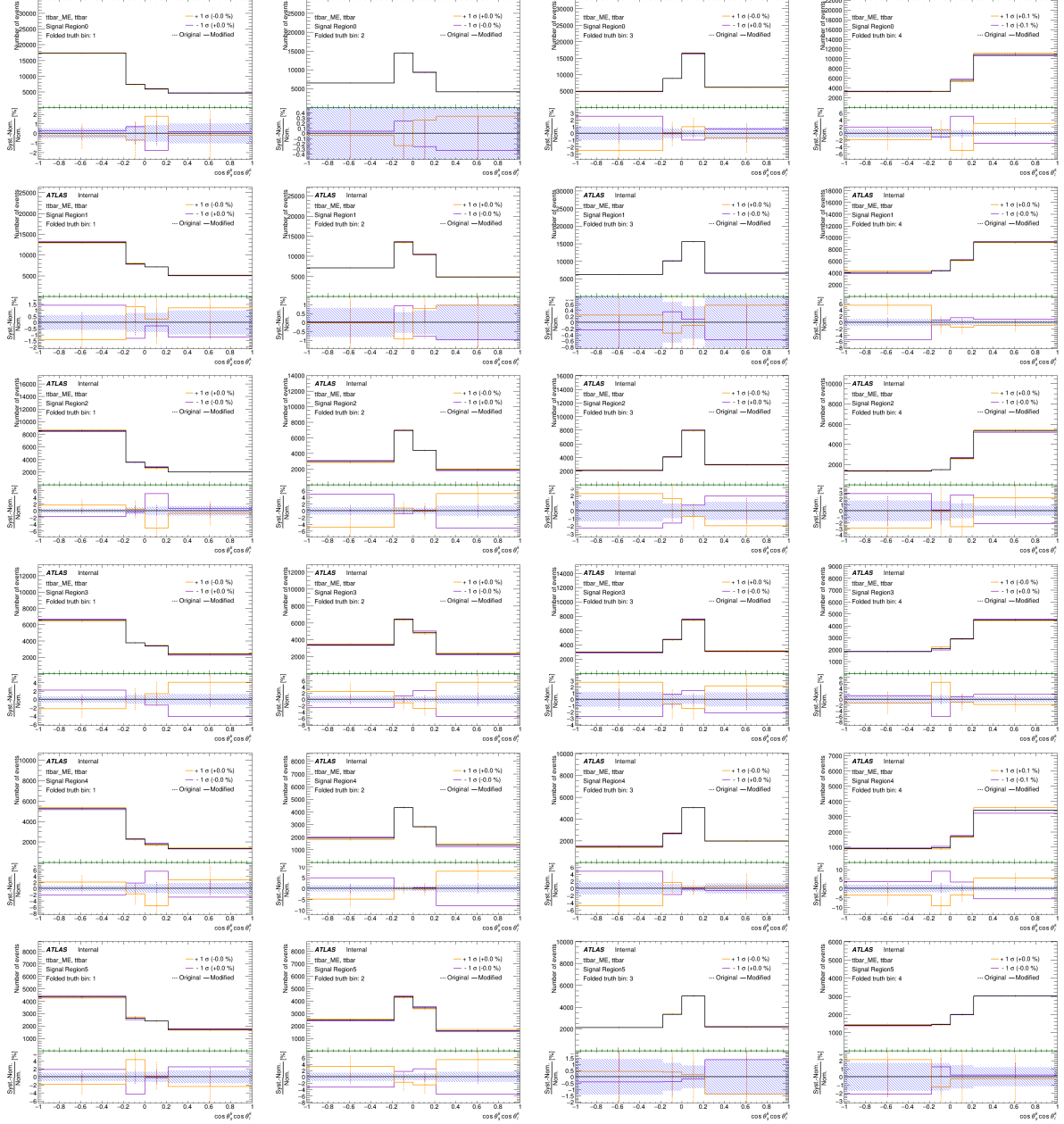


Figure B.1.: Comparison between the nominal distribution and the up/ down variations for the matrix element systematic.

B.1.2. $t\bar{t}$ Parton Shower

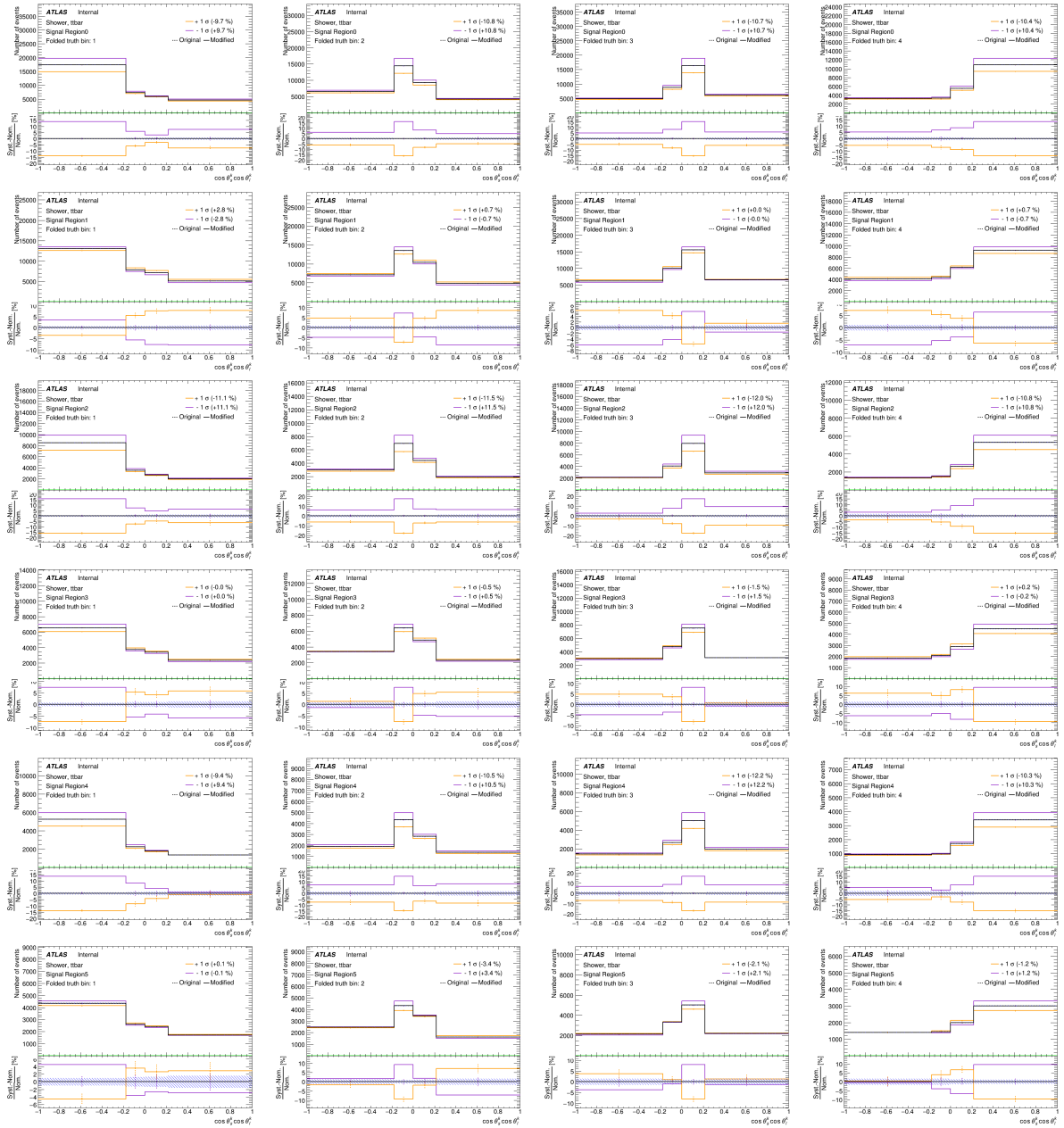


Figure B.2.: Comparison between the nominal distribution and the up/ down variations for the parton shower systematic.

B. Additional Plots for the Systematics

B.1.3. Final State Radiation

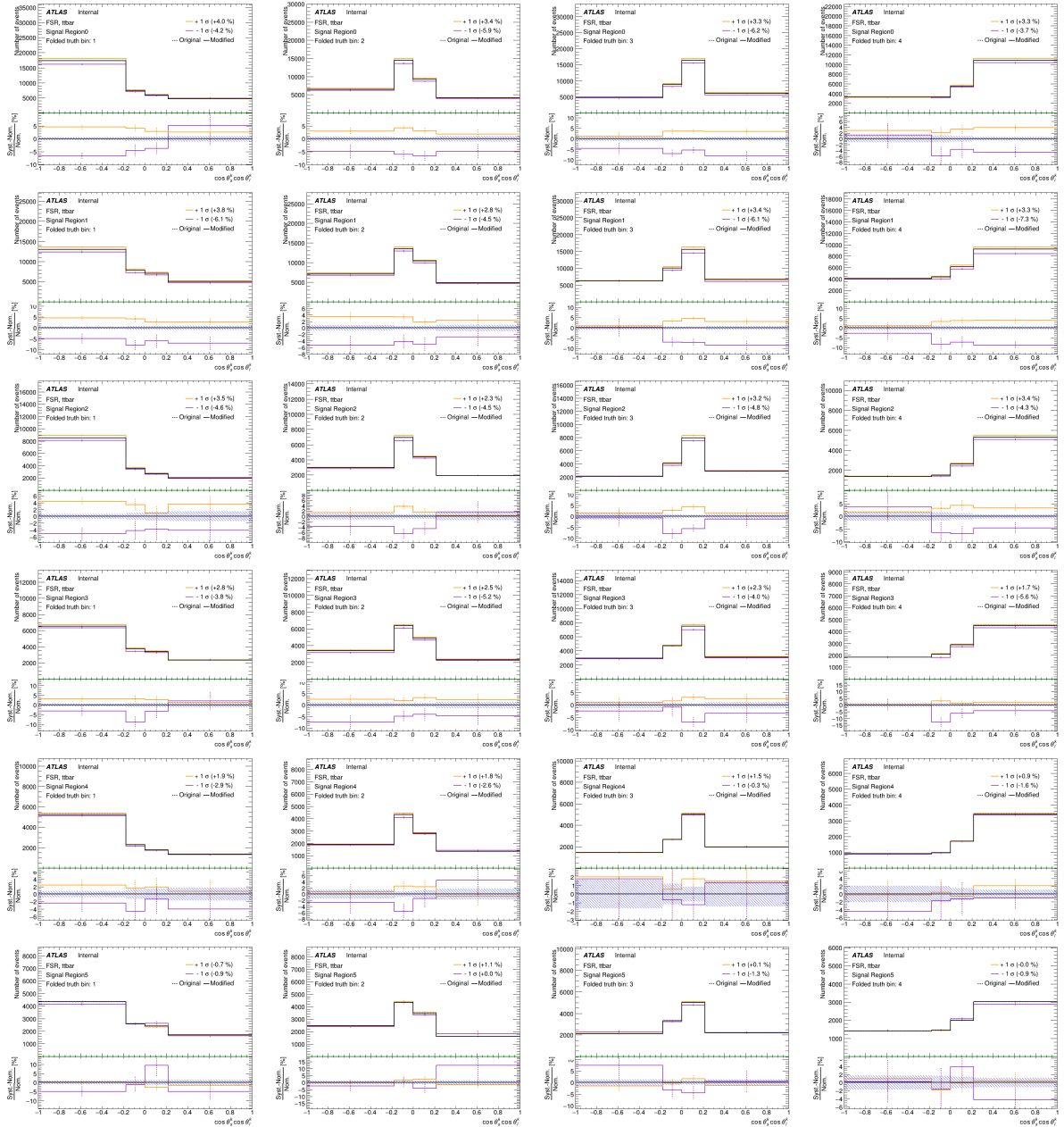


Figure B.3.: Comparison between the nominal distribution and the up/ down variations for the final state radiation systematic.

B.2. $\cos \theta_l^n \cos \theta_s^n$

B.2.1. $t\bar{t}$ Matrix Element

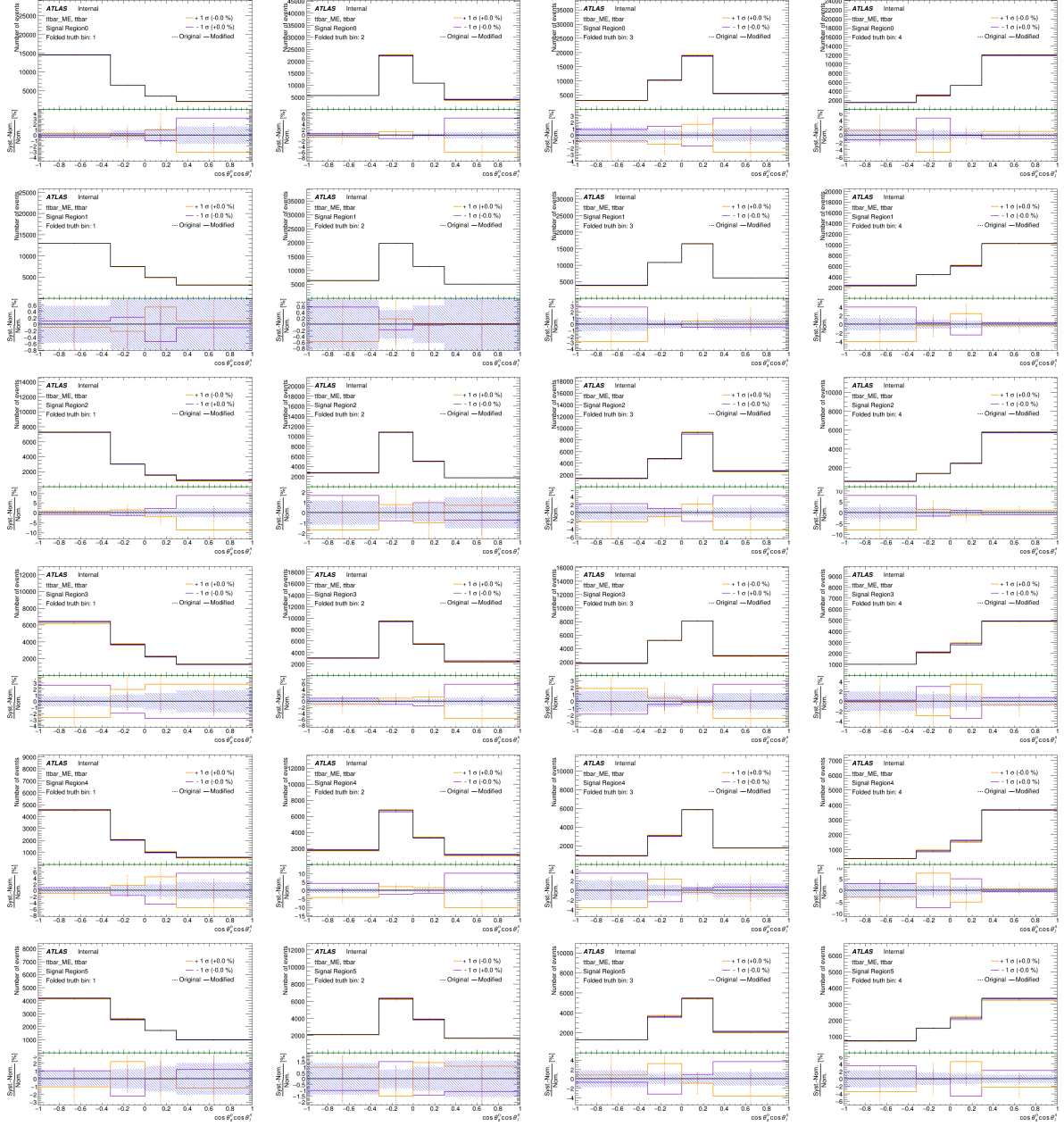


Figure B.4.: Comparison between the nominal distribution and the up/ down variations for the matrix element systematic.

B. Additional Plots for the Systematics

B.2.2. $t\bar{t}$ Parton Shower

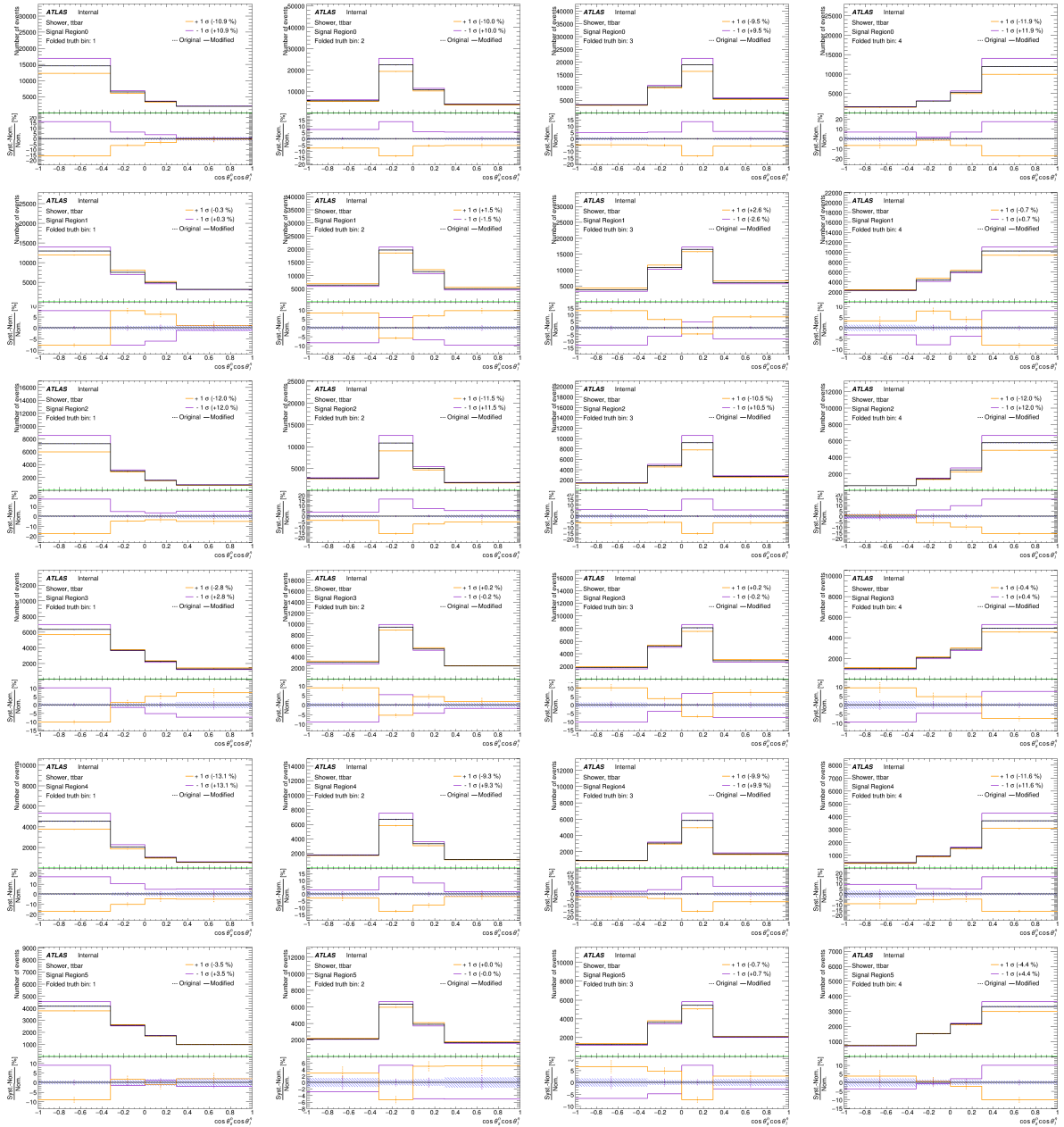


Figure B.5.: Comparison between the nominal distribution and the up/ down variations for the parton shower systematic.

B.2.3. Final State Radiation

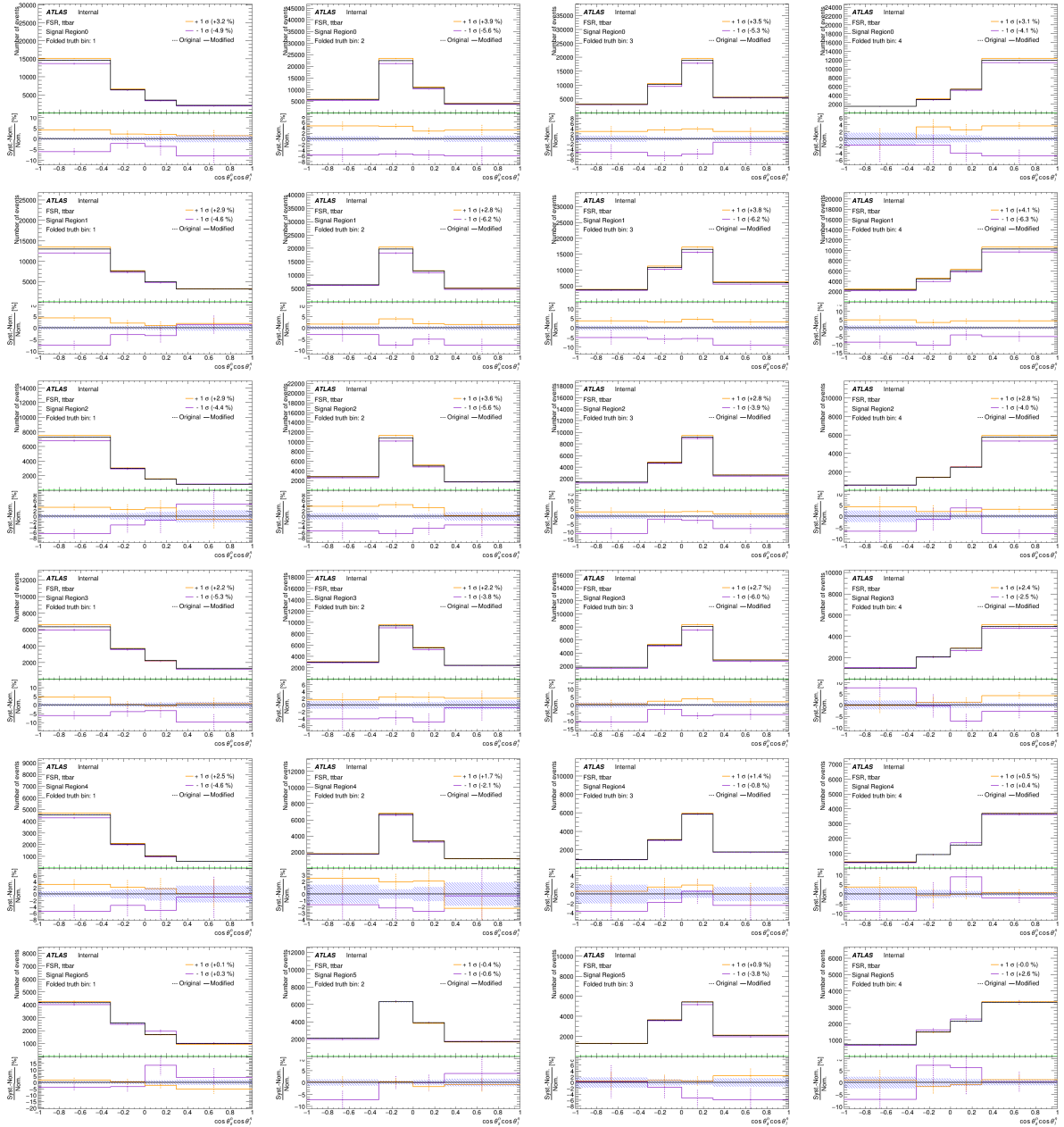


Figure B.6.: Comparison between the nominal distribution and the up/ down variations for final state radiation systematic.

B. Additional Plots for the Systematics

B.3. $\cos \theta_j^r \cos \theta_s^r$

B.3.1. $t\bar{t}$ Matrix Element

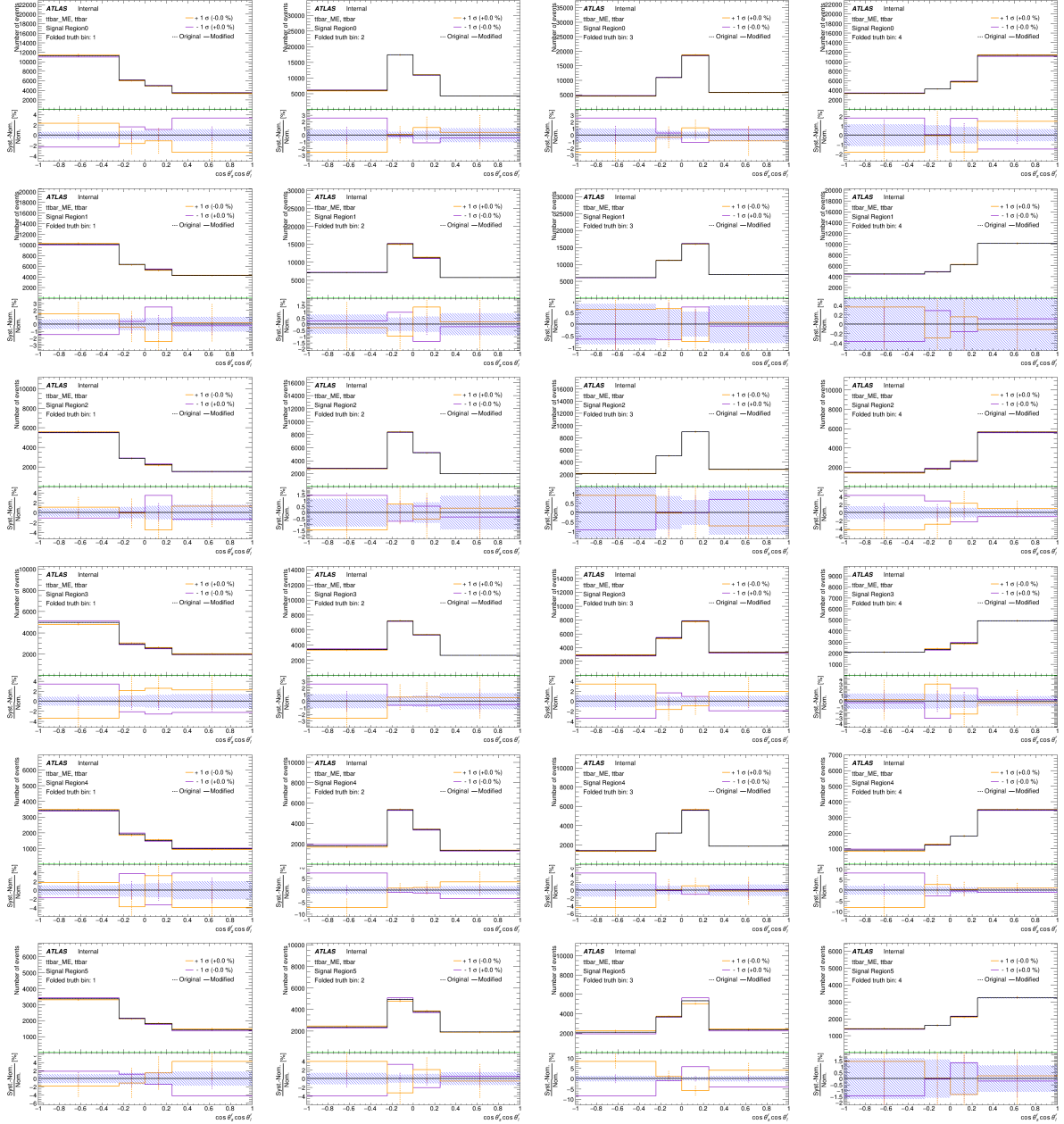


Figure B.7.: Comparison between the nominal distribution and the up/ down variations for the matrix element systematic.

B.3.2. $t\bar{t}$ Parton Shower

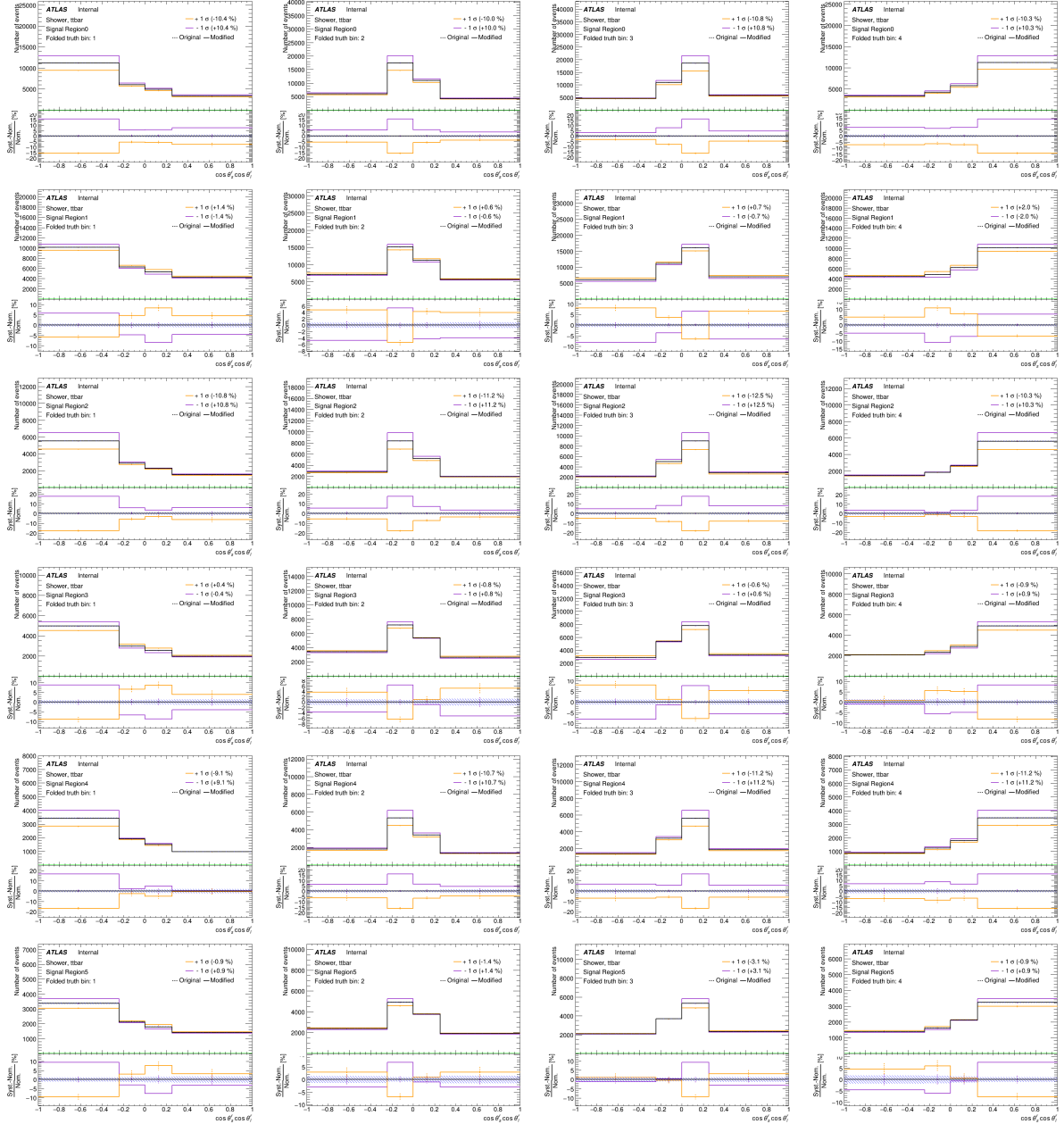


Figure B.8.: Comparison between the nominal distribution and the up/ down variations for the parton shower systematic.

B. Additional Plots for the Systematics

B.3.3. Final State Radiation

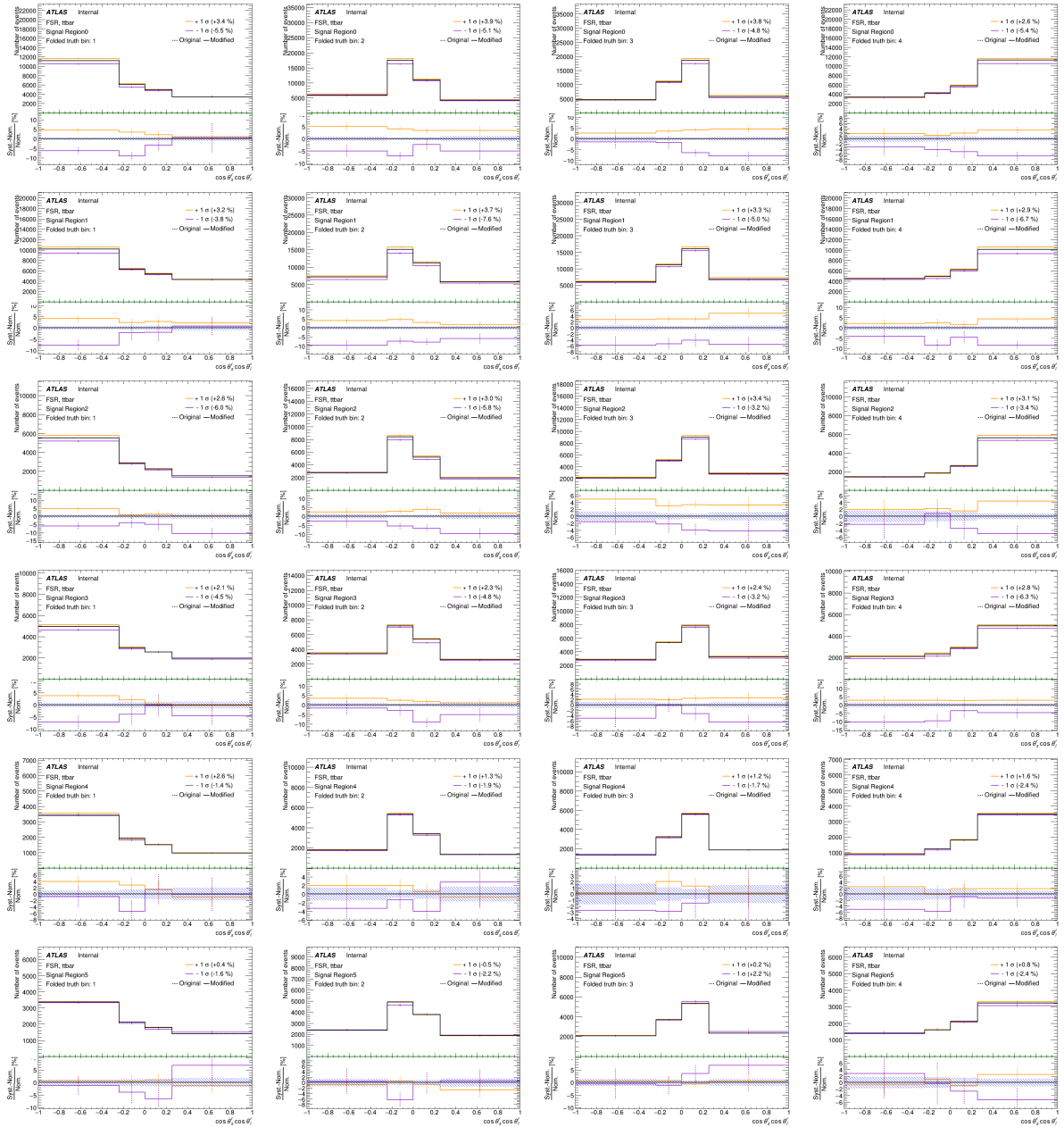


Figure B.9.: Comparison between the nominal distribution and the up/ down variations for the final state radiation systematic.

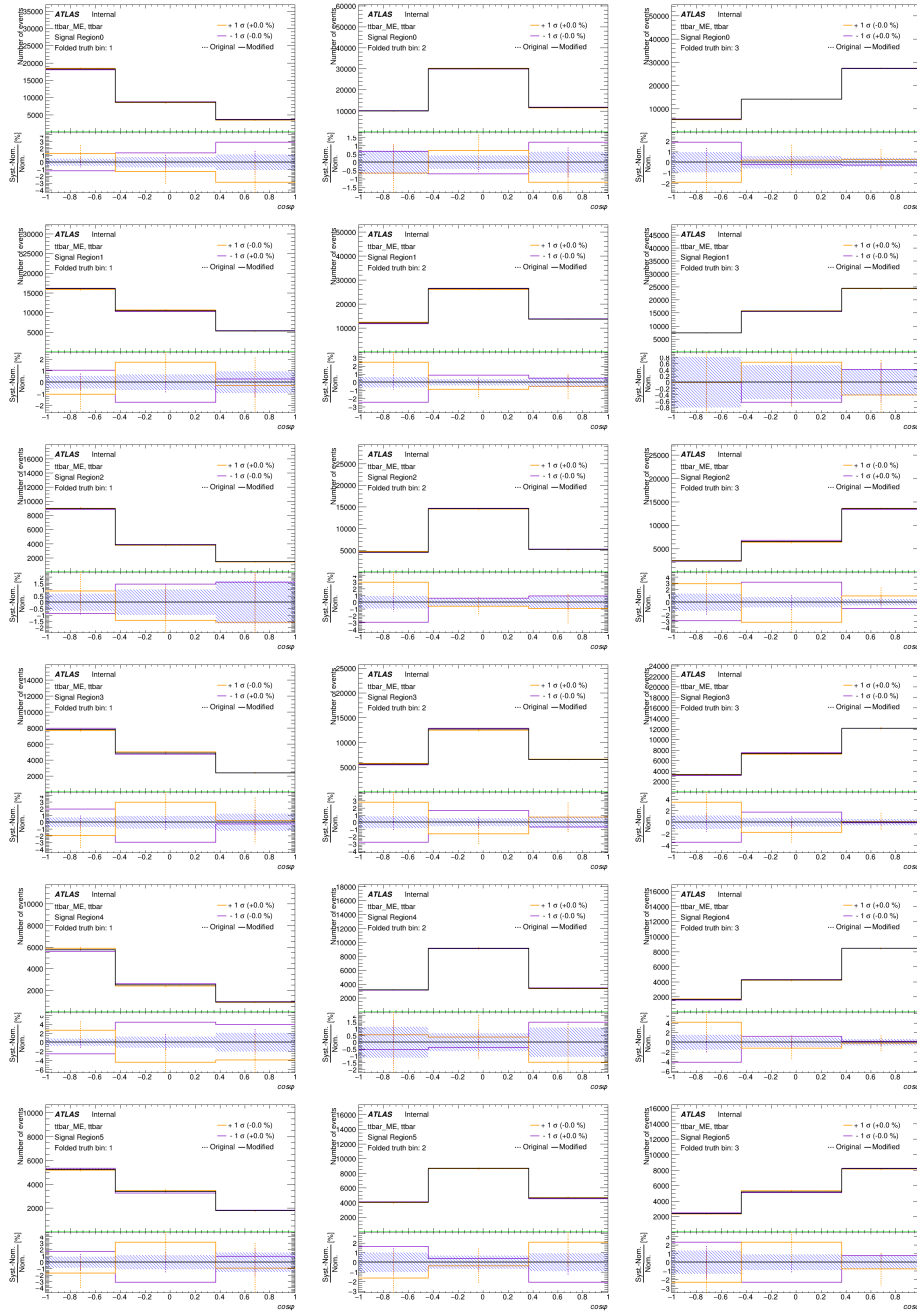
B.4. $\cos\varphi$ B.4.1. $t\bar{t}$ Matrix Element

Figure B.10.: Comparison between the nominal distribution and the up/ down variations for the matrix element systematic.

B. Additional Plots for the Systematics

B.4.2. $t\bar{t}$ Parton Shower

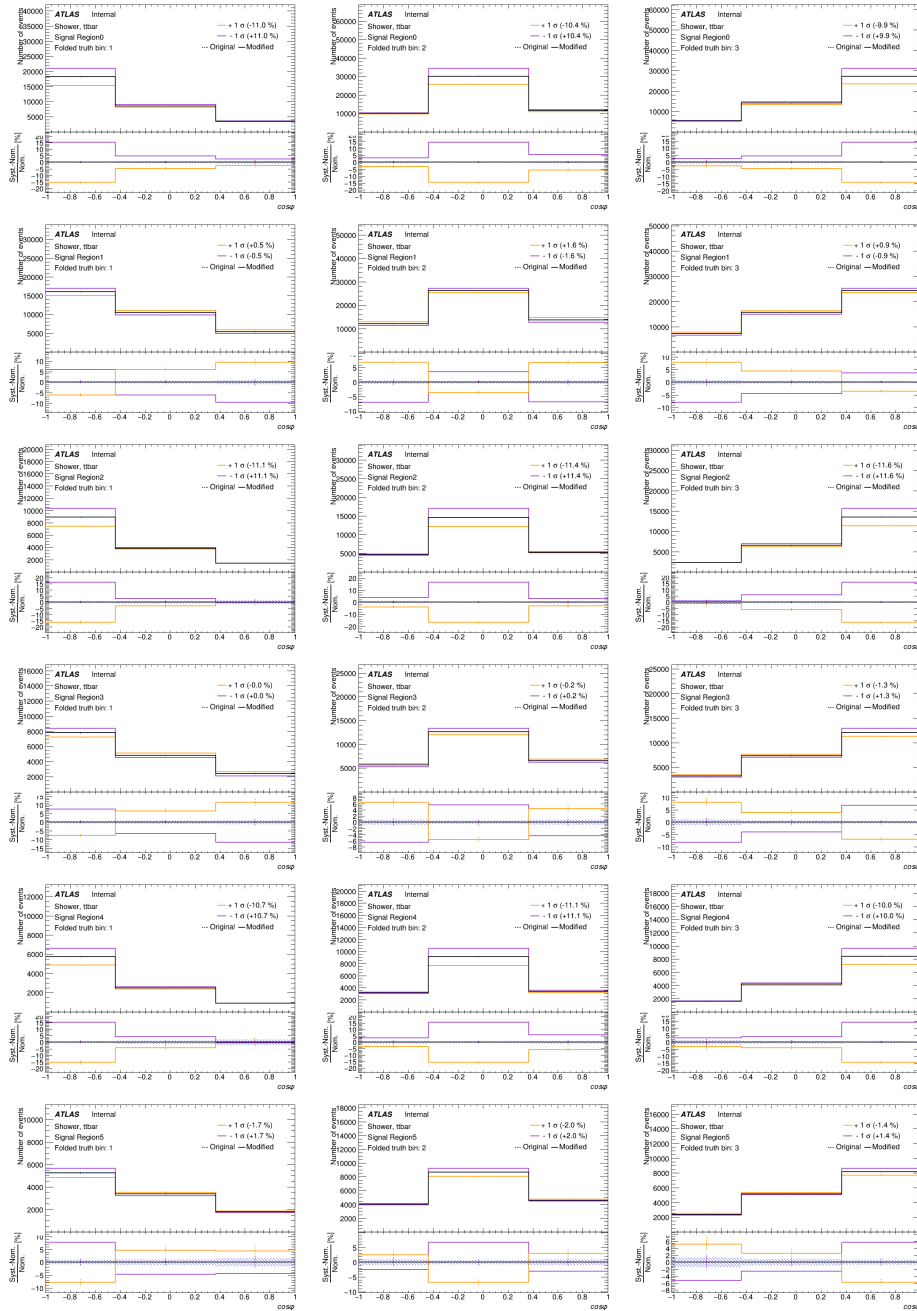


Figure B.11.: Comparison between the nominal distribution and the up/ down variations for the parton shower systematic.

B.4.3. Final State Radiation

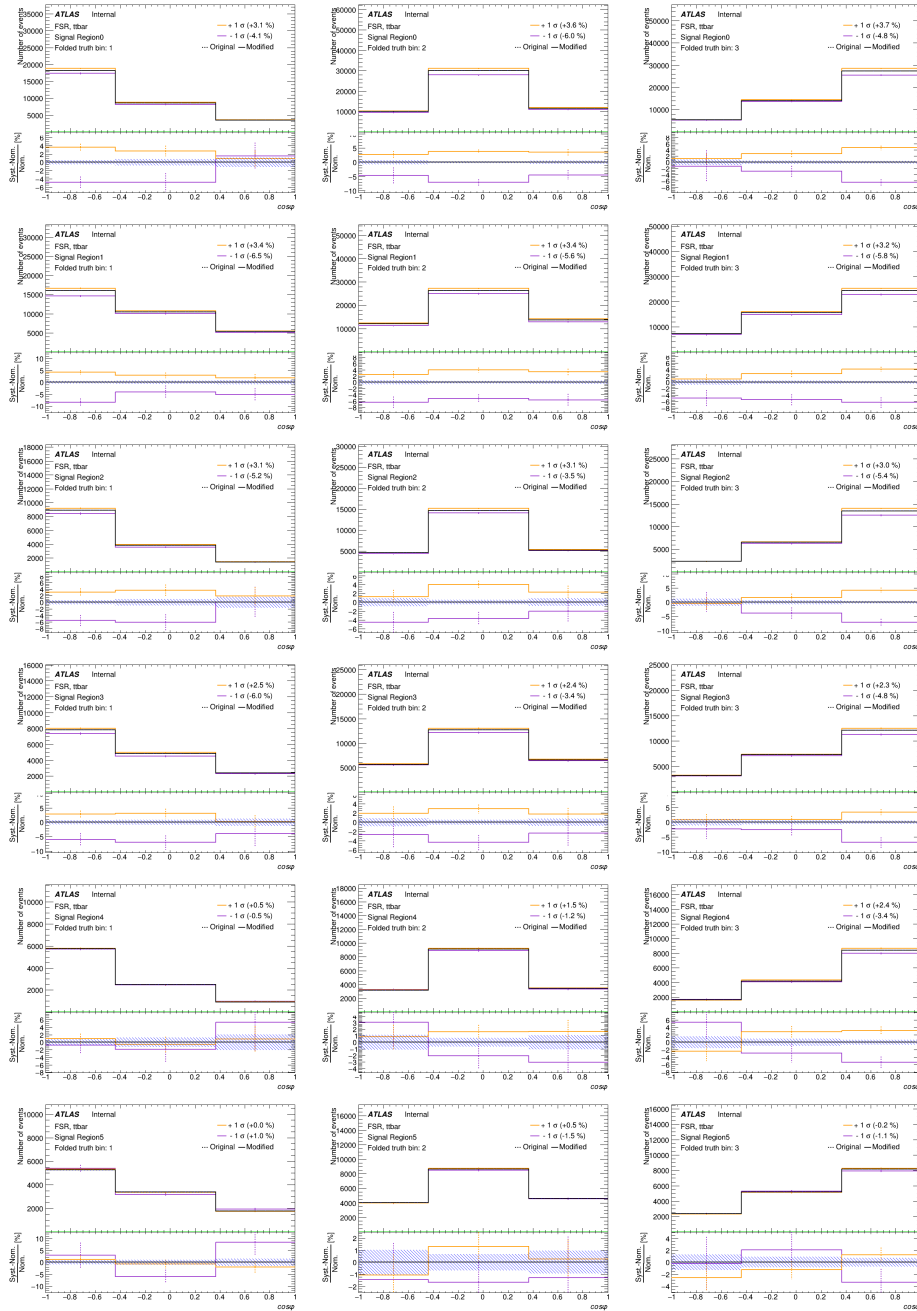


Figure B.12.: Comparison between the nominal distribution and the up/ down variations for the final state radiation systematic.

Bibliography

- [1] ATLAS Collaboration, *Observation of a new particle in the search for the Standard Model Higgs boson with the ATLAS detector at the LHC*, Phys. Lett. B **716(1)** (2012)
- [2] CMS Collaboration, *Observation of a new boson at a mass of 125 GeV with the CMS experiment at the LHC*, Phys. Lett. B **716(1)** (2012)
- [3] A. Aguilar, et al., *Evidence for Neutrino Oscillations from the Observation of Electron Anti-neutrinos in a Muon Anti-Neutrino Beam*, Phys. Rev. D **64(11)** (2001)
- [4] H. D. Politzer, *Reliable Perturbative Results for Strong Interactions?*, Phys. Rev. Lett. **30**, 1346 (1973)
- [5] D. J. Gross, F. Wilczek, *Asymptotically Free Gauge Theories. I*, Phys. Rev. D **8**, 3633 (1973)
- [6] H. D. Politzer, *Asymptotic freedom: An approach to strong interactions*, Physics Reports **14(4)**, 129 (1974)
- [7] E. Eichten, et al., *Charmonium: The model*, Phys. Rev. D **17**, 3090 (1978)
- [8] D. J. Gross, F. Wilczek, *Ultraviolet Behavior of Non-Abelian Gauge Theories*, Phys. Rev. Lett. **30**, 1343 (1973)
- [9] M. Kobayashi, T. Maskawa, *CP-Violation in the Renormalizable Theory of Weak Interaction*, Prog. Theor. Phys. **49**, 652 (1973)
- [10] P. W. Higgs, *Broken symmetries, massless particles and gauge fields*, Phys. Lett. **12**, 132 (1964)
- [11] F. Englert, R. Brout, *Broken Symmetry and the Mass of Gauge Vector Mesons*, Phys. Rev. Lett. **13**, 321 (1964)
- [12] S. Weinberg, *A Model of Leptons*, Phys. Rev. Lett. **19**, 1264 (1967)

Bibliography

- [13] S. L. Glashow, *Partial-symmetries of weak interactions*, Nucl. Phys. **22(4)**, 579 (1961)
- [14] A. Salam, *Weak and Electromagnetic Interactions*, ed. Nobel Symposium N0.8 (1968)
- [15] S. Abachi, et al. (DØ Collaboration), *Search for High Mass Top Quark Production in $p\bar{p}$ Collisions at $\sqrt{s} = 1.8$ TeV*, Phys. Rev. Lett. **74**, 2422 (1995)
- [16] F. Abe, et al. (CDF Collaboration), *Observation of Top Quark Production in $p\bar{p}$ Collisions with the Collider Detector at Fermilab*, Phys. Rev. Lett. **74**, 2626 (1995)
- [17] Particle Data Group, *Review of Particle Physics*, PTEP **2022**, 083C01 (2022)
- [18] I. I. Bigi, et al., *Production and Decay Properties of Ultra-Heavy Quarks*, PLB **181**, 157 (1986)
- [19] G. Mahlon, S. J. Parke, *Spin Correlation Effects in Top Quark Pair Production at the LHC*, Phys. Rev. D **81**, 074024 (2010)
- [20] M. Baumgart, B. Tweedie, *A new twist on top quark spin correlations*, JHEP **2013**, 44 (2013)
- [21] F. Hubaut, et al., *ATLAS sensitivity to top quark and W boson polarization in $t\bar{t}$ events*, Eur. Phys. J. C (**44**) (2005)
- [22] ATLAS Collaboration, *Optimisation and performance studies of the ATLAS b-tagging algorithms for the 2017-18 LHC run*, ATL-PHYS-PUB-2017-013 (2017)
- [23] ATLAS Collaboration, *Measurements of top-quark pair spin correlations in the $e\mu$ channel at $\sqrt{s} = 13$ TeV using pp collisions in the ATLAS detector*, Eur. Phys. J. C **80**, 754. 43 p (2019)
- [24] W. Bernreuther, D. Heisler, Z.-G. Si, *A set of top quark spin correlation and polarization observables for the LHC: Standard Model predictions and new physics contributions*, JHEP (**12**) (2015)
- [25] Y. Afik, J. R. M. de Nova, *Entanglement and quantum tomography with top quarks at the LHC*, Eur. Phys. J. Plus **136(9)** (2021)
- [26] L. Evans, P. Bryant, *LHC Machine*, JINST **3**, S08001 (2008)
- [27] O. Aberle, et al., *High-Luminosity Large Hadron Collider (HL-LHC): Technical design report*, CERN Yellow Reports: Monographs, CERN, Geneva (2020)

- [28] ATLAS Collaboration, *The ATLAS Experiment at the CERN Large Hadron Collider*, J. Instrum. **3(08)**, S08003 (2008)
- [29] ALICE Collaboration, *The ALICE Experiment at the CERN Large Hadron Collider*, J. Instrum. **3(08)**, S08002 (2008)
- [30] CMS Collaboration, *The CMS Experiment at the CERN Large Hadron Collider*, J. Instrum. **3(08)**, S08004 (2008)
- [31] LHCb Collaboration, *The LHCb Experiment at the CERN Large Hadron Collider*, J. Instrum. **3(08)**, S08005 (2008)
- [32] J. Erdmann, et al., *A likelihood-based reconstruction algorithm for top-quark pairs and the KLFitter framework*, Nucl. Instrum. Meth. **748**, 25 (2014)
- [33] S. Frixione, P. Nason, C. Oleari, *Matching NLO QCD computations with parton shower simulations: the POWHEG method*, JHEP **2007(11)**, 070 (2007)
- [34] T. Sjöstrand, S. Mrenna, P. Skands, *PYTHIA 6.4 physics and manual*, JHEP **2006(05)**, 026 (2006)
- [35] T. Sjöstrand, S. Mrenna, P. Skands, *A brief introduction to PYTHIA 8.1*, Comput. Phys. Commun. **178(11)**, 852 (2008)
- [36] E. Bothmann, et al. (Sherpa), *Event Generation with Sherpa 2.2*, SciPost Phys. **7(3)**, 034 (2019)
- [37] J. Alwall, et al., *The automated computation of tree-level and next-to-leading order differential cross sections, and their matching to parton shower simulations*, JHEP **2014(7)** (2014)
- [38] J. Butterworth, et al., *PDF4LHC recommendations for LHC Run II*, J. Phys. G **43** (2016)
- [39] G. Corcella, et al., *HERWIG 6: an event generator for hadron emission reactions with interfering gluons (including supersymmetric processes)*, JHEP **2001(01)**, 010 (2001)

Acknowledgement

First, I want to thank Prof. Arnulf Quadt for offering the place in his working group for my bachelor thesis, being first referee and creating my interest in particle physics in first place. I am also very grateful for his support in applying for the DESY summer school and for making my English language course possible, despite the overlap with the introduction. I am very glad about the possibilities of these unique experiences!

I also want to thank Prof. Ariane Frey for agreeing to be my second referee, supervising my seminar presentation (from quarantine to quarantine) and giving a very interesting particle physics lecture.

I am also very thankful for the help and advice of Dr. Baptiste Ravina who always took the time to look at my plots, give feedback and guide towards the next steps. I also want to thank the whole top quark analysis group for their advice in the Monday meetings.

But most importantly, I want to thank Marcel Niemeyer who was always there for me. Thank you for helping me with coding, bugs, presentations and just any kind of problems, guiding me through the thesis and proofreading it in the end. This thesis wouldn't be what it is without your extraordinary efforts. I have great respect for your expertise and I am very glad that I could profit from it!

I also want to appreciate the extraordinary support from my family and friends, especially when sickness and Covid tried to sabotage me. The last weeks were an exciting but also a challenging time, and I am proud of the work I was able to achieve.

Erklärung

nach §13(9) der Prüfungsordnung für den Bachelor-Studiengang Physik und den Master-Studiengang Physik an der Universität Göttingen: Hiermit erkläre ich, dass ich diese Abschlussarbeit selbständig verfasst habe, keine anderen als die angegebenen Quellen und Hilfsmittel benutzt habe und alle Stellen, die wörtlich oder sinngemäß aus veröffentlichten Schriften entnommen wurden, als solche kenntlich gemacht habe.

Darüberhinaus erkläre ich, dass diese Abschlussarbeit nicht, auch nicht auszugsweise, im Rahmen einer nichtbestanden Prüfung an dieser oder einer anderen Hochschule eingereicht wurde.

Göttingen, den 11. Dezember 2022

(Theresa Reisch)